5-20-2021

Systematic Investigation of Bulk and Surface Properties of Sr3(Ru1-xMnx)2O7

Yifan Yang
Louisiana State University and Agricultural and Mechanical College

SYSTEMATIC INVESTIGATION OF BULK AND SURFACE PROPERTIES OF $Sr_3(Ru_{1-x}Mn_x)_2O_7$

A Dissertation

Submitted to the Graduate Faculty of the
Louisiana State University and
Agricultural and Mechanical College
in partial fulfillment of the
requirement for the degree of
Doctor of Philosophy

in

The Department of Physics and Astronomy

by
Yifan Yang
B.S., Mississippi College, 2012
August 2021

Acknowledgments

I could never have imagined what life would be like as a physics graduate student eight years ago. After graduating with a B.S. in Engineering Physics, I was unsure of my fit in a doctoral program. Fortunately, I had a lot of support from my advisor and our group members, who kindly showed me the way. Without their help, I would never have been able to understand and begin my research on condensed matter physics, nor would I have overcome numerous obstacles to complete my research and finish writing these words.

First of all, I would like to express my special thanks to my late advisor Prof. Ward Plummer for his vision and rigorous approach to science. During times I felt overwhelmed, I have benefited from a quote of his: "Don't look at the trees not the forest." Although I am not a good student, he always had the patience to guide me in my research progression. These qualities have benefited me greatly and are among the most significant values I have gained; may he rest in peace and be long remembered. Secondly, I would like to thank Prof. Rongying Jin for providing me with the opportunity to enter the physics department. I am also very grateful to her and Prof. Jiandi Zhang for their guidance and support throughout my graduate studies and their encouragement in my academic and personal development over the years. I would also like to thank my committee members. Prof. Phillip Sprunger introduced me to the field of ultra-high vacuum experiments, and his rich experimental experience helped me overcome the challenges I encountered. I am also grateful to Prof. Juana Moreno and Prof. Patrick Gilmer serving on my committee and for their contribution and help with my project.

I would also like to give Dr. Von Braun Nascimento additional thanks for his meticulous help with LEED theoretical calculations, to Prof. Weiwei Xie for her help and enthusiastic support

with the X-ray diffraction experiments, and to Dr. Zheng Gai, who assisted with the STM experiments. I need to express my gratitude to all colleagues and friends who have been or are at LSU. Dr. Fangyang Liu, Dr. Hangwen Guo, Dr. Chen Chen, Dr. Zhenyu Diao, Dr. Mohammad Saghayezhian, Dr. Jisun Kim, Dr. Silu Huang, Dr. Jiayun Pan, Dr. Zhenyu Zhang, Dr. Joel Taylor, Dr. Ramakanta Chapai, Joanna Blawat, and Smita Speer. I would also like to thank the mechanical/electronic shop and the department's main office staff members for their help with my experiments.

Finally, I would like to thank my parents for their dedication and my wife, Fei Meng, for her support during my emotional and academic difficulties over the past few years. I would like to thank my newborn daughter, Chloe Yang, for giving me hope in life.

Table of Contents

Abstract

Transition metal oxides (TMOs) have attracted considerable interest due to the intriguing interactions between spin, charge, and lattice degrees of freedom. The delicate balance between these interactions can be altered by doping, symmetry breaking, and other external stimuli such as pressure, electric field, and magnetic field. The Ruddlesden-Popper (RP) family of ruthenates, $Sr_{n+1}Ru_nO_{3n+1}$, is a prototype of TMOs with stacking octahedra along the *c* axis, and the intra- and inter-octahedral structures are known to be crucial to both electronic and magnetic properties. In this dissertation, we focus on studying the effects of chemical doping and broken symmetry at the surface of bilayered $Sr_3(Ru_xMn_{1-x})_2O_7$ ($n = 2$), especially emphasizing the correlation of emergent surface electronic-magnetic properties with the lattice structure.

Bulk $Sr_3Ru_2O_7$ is paramagnetic and metallic with octahedra rotating around the *c*-axis. As Ru is partially replaced by Mn, $Sr_3(Ru_{1-x}Mn_x)_2O_7$ undergoes a metal-insulator transition (MIT) and an antiferromagnetic (AFM) phase transition coupled with *x*, leading to an AFM-insulating ground state. Creation of the surface breaks the bulk translational symmetry, leading to further perturbations of the system.

In this work, we complete the single-crystal X-ray diffraction study of $Sr_3(Ru_{1-x}Mn_x)_2O_7$ samples at low temperatures (28 K) and construct a surface phase diagram by using a combination of surface-sensitive characterization methods. Quantitative analysis of low-energy electron diffraction intensity versus voltage (LEED I-V) measurements are used to investigate the variation of the surface lattice. As *x* increases, the surface octahedral rotation angle decreases and is accompanied by a change in the bond lengths of surface octahedron. The temperature and magnetic field dependence of the scanning tunneling spectroscopy (STS) spectra of $Sr_3(Ru_{1-x}Mn_x)_2O_7$ (x = 0, 0.08, 0.16, and 0.23) indicate that the surface is metallic and nonmagnetic. We also use high-

resolution electron energy loss spectroscopy (HREELS) to indirectly verify the surface conductivity by the asymmetric Fano line shape of $A_{1g}(2)$ phonon mode.

Based on our detailed experimental investigations, we found that the surface of $Sr_3(Ru_{1-x}Mn_x)_2O_7$ has strikingly different properties from the bulk phase. This discovery allows us to gain insight into the relationship between surface structure and electronic/magnetic properties of $Sr_3(Ru_{1-x}Mn_x)_2O_7$ and provides an ideal platform for exploring the hidden bulk phases.

Chapter 1. Introduction

1.1 Correlated Electron Systems

In the last few decades, modern condensed matter physics has made great experimental efforts to explore the extraordinary physical properties of correlated electron systems and to explain the origin of their driving mechanisms theoretically. In these correlated electron systems (CEMs), electrons are no longer treated in dependently, but rather as a correlated behavior. The affected electronic interactions include Coulomb interactions and electron-phonon interactions that prevent electrons from jumping from one site to another [1,2]. Correlated materials exhibit complex and unique behaviors by tuning different parameters (e.g., composition, temperature, magnetic field, and pressure) [3-5]. As shown in Figure 1.1, there exists close coupling between the lattice, charges, orbitals, and spins in CEMs and external stimuli that disturb the balance of this coupling can induce novel physical properties.

The surface of correlated electronic materials is in many ways a new material, and the collective behavior observed in such materials arises from strong correlations between electrons. This phenomenon cannot be explained through classical treatment of the electronic properties, which cannot be explained by independent electronic properties, making it very difficult to develop any microscopic theory for these materials. Partially filled *d*-electron correlated transition metal oxides (TMOs) are a typical CEM system. TMOs contain many novel phenomena such as high temperature superconductivity, giant magnetoresistance, charge and spin density waves, quantum phase transitions, and different types of metal-insulator transitions, among others [6]. For example, in the case of chalcogenide transition metal oxides (chemical formula ABO_3), the A-site ions are rare earth or alkaline earth ions, and the B-site ions are transition metal elements [7]. Their rich physical properties are closely related to the lattice structure, A and B site elements. Therefore, it

is possible to introduce structural changes in the material by introducing chemical intercalation. An example is the doping with Ca on Ru sites of single layer Sr_2RuO_4, where the octahedral rotation dramatically affects the electronic band and orbital occupancy, and thus the physical properties [8].

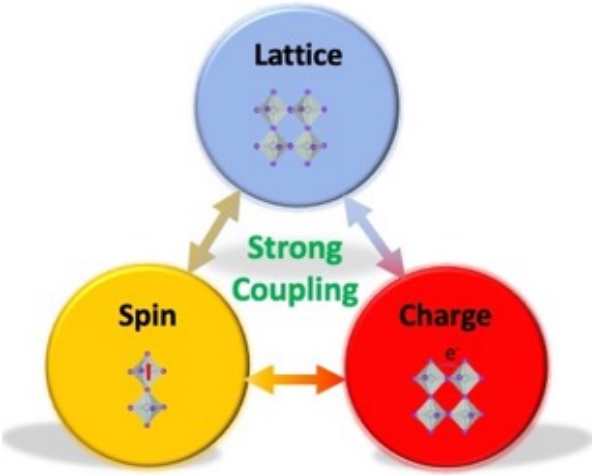

Figure 1.1.Strong nonlinear coupling between lattice, charge, and spin in CEMs.

From doping atomic sites containing elements with different valence states, such as Ca^{2+} doped into La^{3+} site of $La_{1-x}Ca_xMnO_3$, the additional holes change the bandwidth and band filling while maintaining the orthorhombic structure in the bulk of the crystal [9]. On these materials, one can perturb the system with an external source and measure the response of the system. The complex nature of the emergent phenomena allows one to control the structure of the material in distinct ways to tune a particular property of the material.

Creating a surface breaks the translational symmetry and thus induces a perturbation in the system [10]. Due to the nature of the CEMs, this perturbation can dramatically affect competing ground states and create new emergent phenomena. If a material has a layered structure, then we can create a surface by cleaving the sample and use it to explore the surface properties in the material [11-13].

1.2 Ruddlesden-Popper Ruthenates

The ruthenium oxides of the Ruddlesden-Popper (RP) series, $Sr_{n+1}Ru_nO_{3n+1}$ (n = 1, 2, 3, ...∞), are a very important class of compounds that are extremely sensitive to impurities due to the flexibility and reactivity of the delocalized Ru 4*d* orbital. Structurally, RP ruthenates form alternating layers of Sr-O and Ru-O planes, as shown in Figure 1.2. The crystal structure of layered RP ruthenates has n stacks of RuO_6 octahedra within the unit cell with shared oxygen along the *c*-direction [14]. Due to a relatively large separation between each Sr-O layer, they are weakly bound by van der Waals forces, and prone to cleave under external force. With the evolution of n, the octahedra in the *ab* plane have a half unit cell lateral shift. Like other CEMs, the phase diagrams of RP ruthenates are very complex and depend on n and octahedral distortions. The structural symmetry decreases as RuO_6 octahedra distort from a perfect cubic perovskite. The deviation from perfect cubic structure is assessed by a Goldschmidt tolerance factor t as a function of the A, B site ion radii r_A, and r_B [15]. For $SrRuO_3$ ($n = \infty$), $t = 1$ indicates an ideal cubic structure. while $t \neq 1$ indicates the octahedral distortion, such as in Figure 1.3, Sr_2RuO_4 ($n = 1$) is isostructural to the high-T_c compound $La_{2-x}Ba_xCuO_4$, having a layered perovskite structure with one RuO_2 plane per unit, and a *p*-wave superconductor with a spin-triplet [16]. On the other hand, $SrRuO_3$ ($n = \infty$) is an itinerant ferromagnet with three-dimensional behavior [17].

The magnetism in $Sr_{n+1}RunO_{3n+1}$ evolves with n and the bilayered $Sr_3Ru_2O_7$ (n = 2) intermediates between n = 1 and ∞, exhibiting a competition between ferromagnetic (FM) and antiferromagnetic (AFM) instabilities as well as quantum metamagnetic transitions [4,18,19]. The different compounds of RP ruthenates show distinct changes in physical properties and ground state behavior with n. Due to the difference in the Goldschmidt tolerance factor t of each TMOs, structural changes lead to distortions in the M-O-M bond angles and thus determine the conduction

band width W. As the system dimension decreases, especially in two-dimensional systems, the effect of structural distortions on W appears to be more drastic. A comparison between Sr and Ca compounds $(Sr, Ca)_{n+1}Ru_nO_{3n+1}$ (n = 1, 2) is shown in Figure 1.3. Both Ca_2RuO_4 and $Ca_3Ru_2O_7$ undergo metal-nonmetallic transitions with antiferromagnetic behavior, and the transition temperature decreases with n. While for Sr_2RuO_4 and $Sr_3Ru_2O_7$, both compounds remain metallic over the entire temperature range and display ferromagnetic behavior. Thus, structural changes triggered by the covalent doping of Ca^{2+} with Sr^{2+} at the A-site can produce a rich bulk phase diagram [19,20].

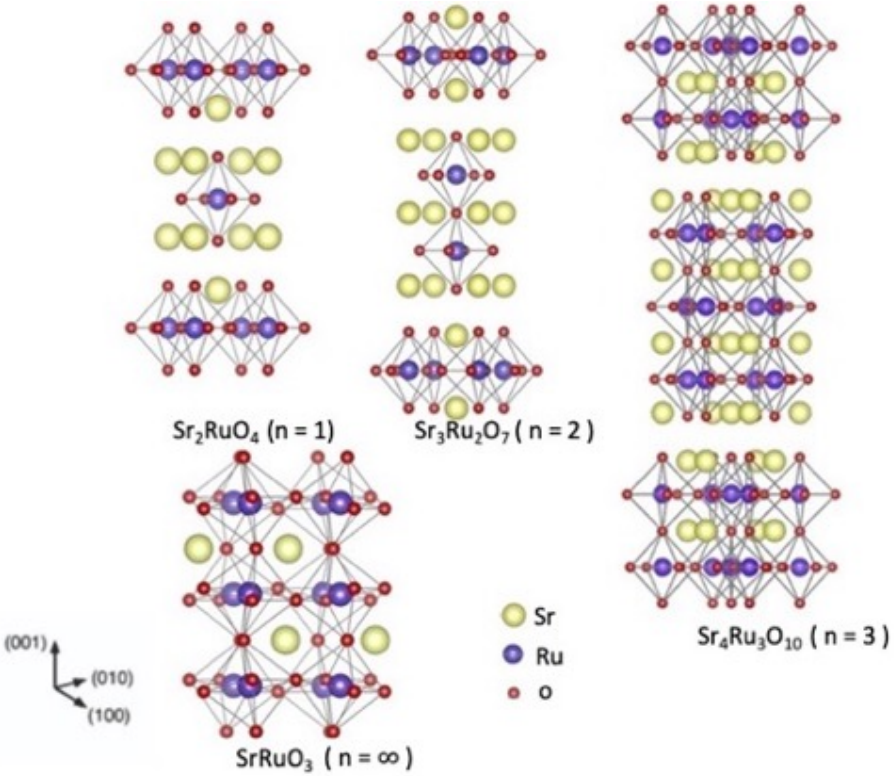

Figure 1.2. Crystal structures of the Ruddlesden-Popper ruthenates $Sr_{n+1}Ru_nO_{3n+1}$ (n = 1, 2, 3, ...∞) with RuO_6 octahedra stacking along the c direction.

The lattice dynamics of Sr_2RuO_4 (n = 1) have been investigated by inelastic neutron scattering, as shown in Figure 1.4. The Σ_3 and Σ_4 phonon modes are associated with the rotational mode of RuO_6 around an axis parallel to the c-axis and the tilting mode of the axis in the ab-plane,

respectively. Unlike the Σ_4 mode, which is flat throughout the Brillouin zone, the Σ_3 mode shows softening at the zone boundary along the blue line, where its phonon energy is significantly reduced in the second half of the Brillouin zone. Due to the interaction between the optical and acoustic phonon branches, along the blue line is the direction for the measured dispersion of the Σ_3 softened phonons. This softening behavior corresponds to a structural instability of the rotational distortion of the RuO_6 octahedron [21]. The partial replacement of Sr site in Sr_2RuO_4 (n = 1) with Ca results in the observation of structural changes and the appearance of the softened Σ_4 mode [22]. These structural transitions are closely coupled with magnetic and physical properties, as shown in the rich phase diagrams in Figure 1.5. The structure of $Ca_{2-x}Sr_xRuO_4$ in Figure 1.5a undergoes a first-order phase transition from the space group *I4/mmm* to *I4$_1$/acd* and *Pbca* to *S-Pbca* phase as the concentration of Sr changes. Figure 1.5b contains a x coupled AFM to paramagnetic transition and a MIT transition from the unconventional superconductivity. These changes in the physical properties are accompanied by an increase in the tilt angle and an increase

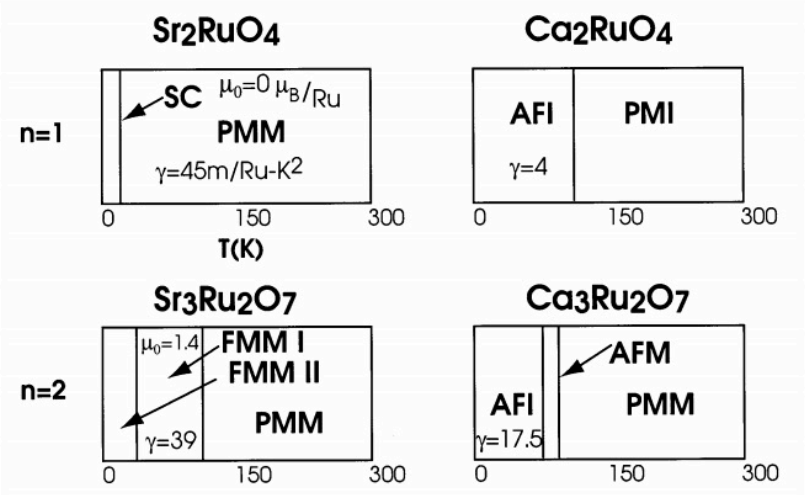

Figure 1.3. Summary of different phase diagrams for Sr- and Ca-based ruthenates (n =1, 2). The physical properties of both ruthenates show dimensionality dependence: Ca_2RuO_4 and $Ca_3Ru_2O_7$ undergo metal-nonmetallic transitions with antiferromagnetic behavior while Sr_2RuO_4 and $Sr_3Ru_2O_7$ compounds remain metallic and display ferromagnetic behavior. Transition temperatures vary with n. Figure adapted from Ref. [19].

in the length of the in-plane bonds, which strongly reduce the bandwidth and, in turn, explains the non-metallic behavior [23,24]. Moreover, the crystal field generated by the rotation of the RuO_6 octahedron lifts the band degeneracy changing the band structure with two electron-like pieces and one hole-like piece. The bulk band splitting is evidenced through high-resolution ARPES measurements [25,26]. Thus, it is determined that the structural changes in RuO_6 are closely related to the magnetic and electronic properties of the system, and minor chemical doping can dramatically alter the physical properties of RP ruthenates. In addition to the splitting of energy levels by the octahedral crystal field, the distortion of the octahedra (Jahn-Teller effect) further

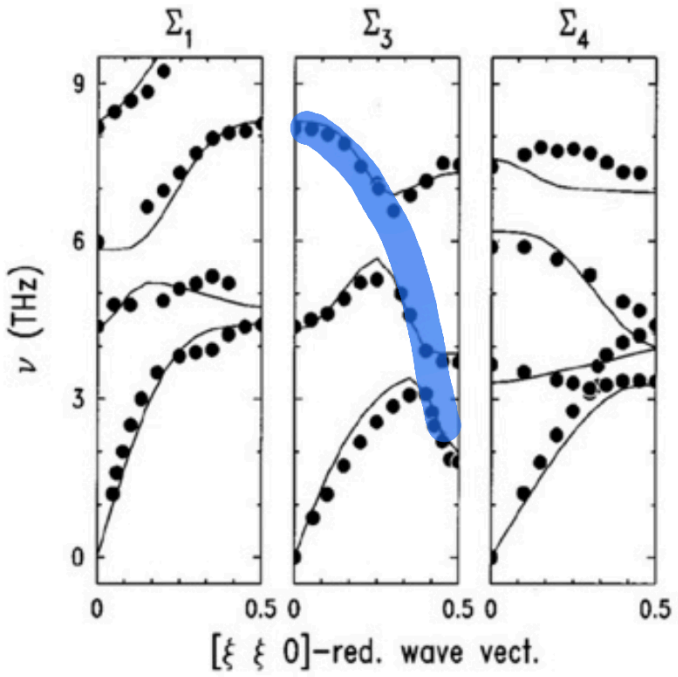

Figure 1.4. Measured Σ phonon dispersion along [110] for Sr_2RuO_4 with three different phonon modes Σ_1, Σ_3, and Σ_4. Unlike octahedral tilt associated with the Σ_4 mode in (0.5 0.5) what has only a slight drop or remains flat until the zone boundary. The RuO_6 octahedral rotational Σ_3 phonon mode has a steep dispersion along the direction of the blue line in the figure at the zone boundary. This represents a typical structural instability of perovskites [21].

degenerates the orbitals [27,28]. For example, the atomic orbitals associated with each energy level in the manganese oxide system shown in Figure 1.6. The crystal field splits the Mn *d* levels into a

higher two-fold e_g level and a lower three-fold t_{2g} level. When the octahedra elongate or compress along the z-axis, the distortion of an octahedron in the xy plane is much larger than the distortion in the z-axis direction. So, the e_g splits into $d_{x^2-y^2}$, $d_{3z^2-r^2}$, and t_{2g} splits into $d_{xy}, d_{zx},$ and d_{zy} which lifts the e_g degeneracy and reduces the overall system energy.

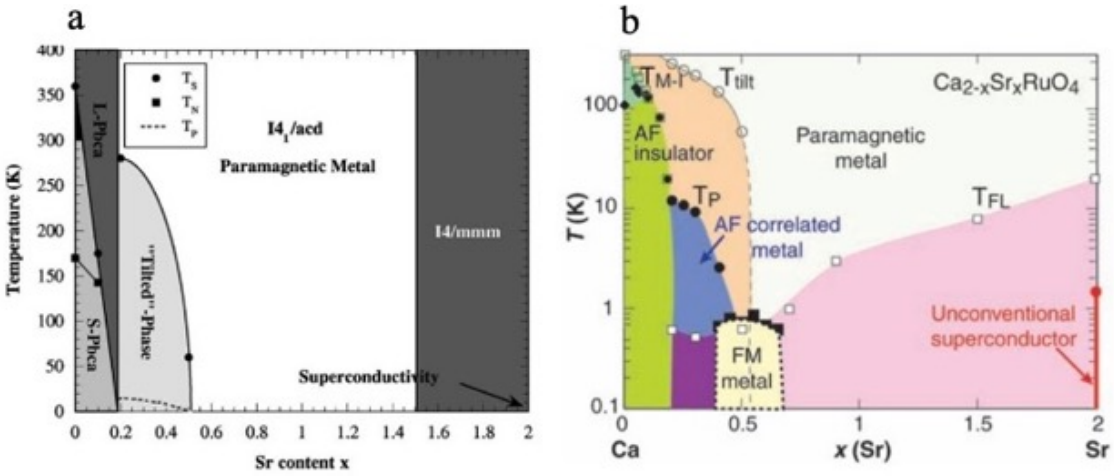

Figure 1.5. Structural and electronic/magnetic phase diagrams of $Ca_{2-x}Sr_xRuO_4$ resulting from partial replacement of Ca by Sr. (a) Structural phase diagram of $Ca_{2-x}Sr_xRuO_4$ shows the octahedral distortion of the Ru-O-Ru bond angle with x. The structure undergoes a transition from $I4/mmm$, $I4_1/acd$ to $Pbca$, accompanied by a superconducting state, and a metal-insulator transition and magnetic transition labeled by T_s and $T_{N,}$ respectively. (b) The $Ca_{2-x}Sr_xRuO_4$ electronic/magnetic phase diagram. There are several different regions of superconducting, antiferromagnetic metal/insulator regions and paramagnetic metal/insulator with x = 0.5 as a critical point. The structure and physical properties are coupled in $Ca_{2-x}Sr_xRuO_4$ [23,24,29].

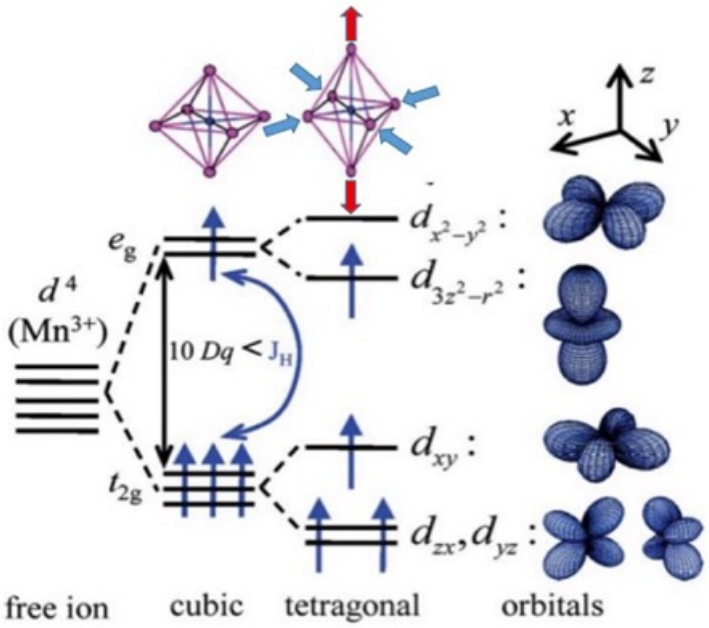

Figure 1.6. Schematic of the 3*d* levels of Mn split subsequently by the crystal field and Jahn-Teller distortion lift the five-fold band degeneracy. This figure is adapted from Ref. [30].

1.2.1 Structural and Physical Properties of Bulk $Sr_3Ru_2O_7$

More pertinent to my dissertation research is the double-layered $Sr_3Ru_2O_7$ (n = 2), where the additional RuO_6 layer leads to a rather different electronic and magnetic properties in Sr_2RuO_4. The classification of the bilayered $Sr_3Ru_2O_7$ structure has long been controversial. A tetragonal structure with space group *I*4/*mmm* was first proposed in 1990 [14]. Later, Shaked et al. reported an orthorhombic structure with space group *Bbcb* (#68) from neutron diffraction studies at room temperature, where the bulk's RuO_6 octahedron has an intrinsic ~ 6.8^o rotation around the *c*-axis [31] [32].The superlattice reflection (SLR) in Figure 1.7a shows that the *Bbcb* group has a larger superlattice, and the resulting unit lattice has parameters $a_{sup} = b_{sup} = a\sqrt{2}$ while $c_{sup} = c$. Then, Huang proposed that $Sr_3Ru_2O_7$ crystallizes in the *Pban* symmetry group with a half unit cell side shift between the two RuO_6 stacking sequences, as shown in Figure 1.7b [33].

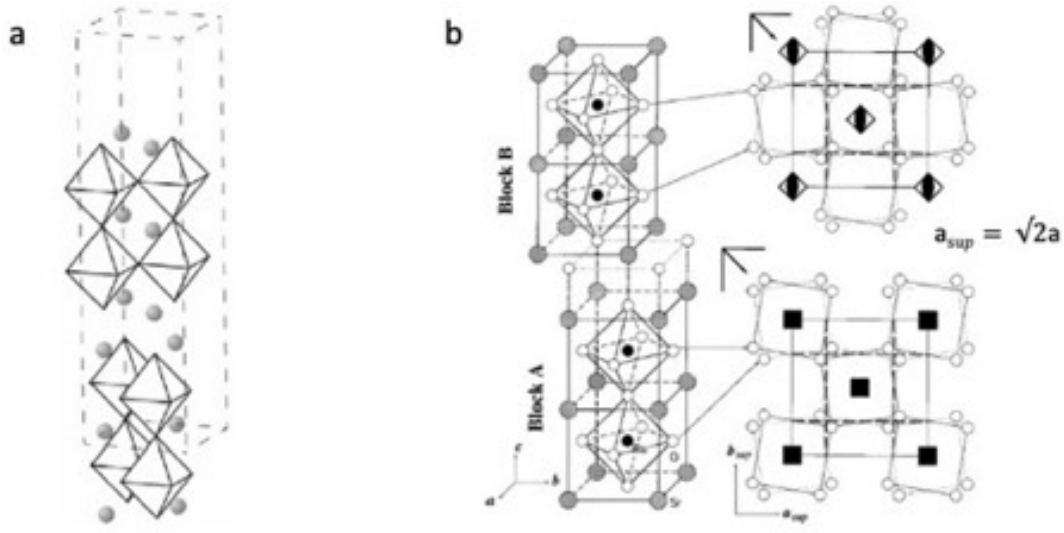

Figure 1.7. Bulk structural distortions in $Sr_3Ru_2O_7$ with different crystalized symmetries: (a) *Bbcb* symmetry group: Supercell with a lattice parameter $\boldsymbol{a_{sup} = \sqrt{2}a}$ [31]. (b) *Pban* symmetry group: two blocks of distorted double-layered RuO_6 stacking with two neighboring RuO_6 octahedra sharing an oxygen atom in between with two-fold vertical symmetry [33].

The electronic properties of $Sr_3Ru_2O_7$ in the microscopic view can be understood by considering the lifting of the band degeneracy by the rotation of the bilayered RuO_6 octahedra. The Fermi surface for $Sr_3Ru_2O_7$ is shown in Figure 1.8. The band has $\alpha_1, \alpha_2, \beta, \gamma_1, \gamma_2$ and δ sheets cross Fermi energy, where δ belongs to the usually unoccupied e_g orbitals. γ_1 and β are a mixture of $d_{xy,yz}$ and d_{xy} orbitals. From the band dispersion analysis, it is found that the γ_2 sheet has a significant d_{xy} contribution, close to the van Hove singularity, with an enhanced quasiparticle mass on γ_2, and its presence favors the magnetic instability of $Sr_3Ru_2O_7$ [34-36].

Macroscopically, $Sr_3Ru_2O_7$ is a paramagnetic metal, and magnetic instability dominates its physical properties [37]. Among them, two magnetic exchange mechanisms can strongly affect the overall magnetic properties in transition metal oxides: double exchange and super exchange. Both of which depend strongly on the change of bond lengths and bond angles of RuO_6 octahedra [38]. As shown in Figure 1.9a, applying a magnetic field of in-plane size ~5.5 T or out-of-plane

~7.7 T, the magnetization increases super linearly as a characteristic of its metamagnetic behavior [39]. Another peak of lower intensity ~5.8T dM/dH diagram below 1.7K was subsequently observed by Ohmichi et al. in Figure 1.9b [40].

$Sr_3Ru_2O_7$ also exhibits metamagnetic quantum critical point (QCP) behavior in the presence of an applied magnetic field, as shown in Figure 1.9c [4]. The QCP can be reached by magnetic fields, applied pressure, and chemical composition [41], and observed with "V-shaped" quantum critical region of Fermi liquid and non-Fermi liquid behaviors in the resistivity mapping in Figure 1.9c.

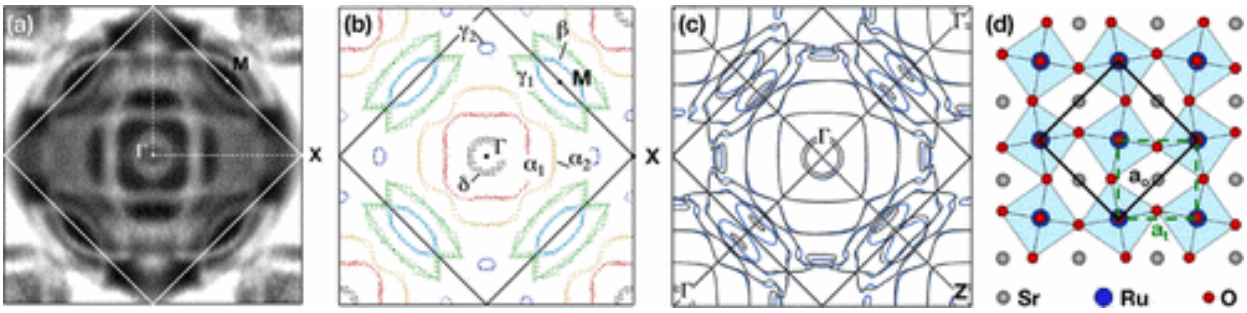

Figure 1.8. Fermi surface topologies and simulations of $Sr_3Ru_2O_7$. (a) experimentally obtained Fermi surface by ARPES. (b) Identification of the sheets on the Fermi surface. (c) The Linear Discriminant Analysis (LDA) calculated Fermi surface matches well with the experimental observations. (d) Illustration of RuO_6 octahedra rotation, the enlarged unit cell is marked with a black square, and the tetragonal lattice is marked with a dashed green square. The nearest Ru-Ru length and unit cell length are labeled. This figure is adapted from Ref. [36].

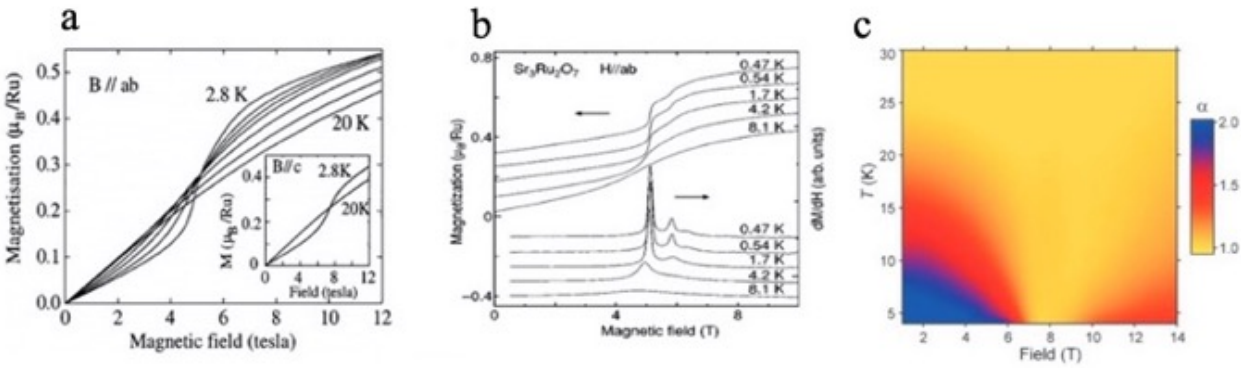

Figure 1.9. The double layered $Sr_3Ru_2O_7$ exhibits a metamagnetic (i.e., magnetic field tuned) quantum critical point (QCP). (a) Low-temperature magnetization measurements for $Sr_3Ru_2O_7$. (a) metamagnetic transition is characterized by rapidly increased magnetization in M(H) plot with applied in-plane field ~5.5 T and out-of-plane ~ 7.7 T (inset). (b) A second metamagnetism transition is observed at higher filed (5.8 T), below is dM/dH plot with a clear second peak at the right side of the major 5.5 T peak. Figure adapted from Ref. [39,40]. (c) Field and temperature revolution of $\boldsymbol{\alpha}$ from expression $\boldsymbol{\rho = \rho_{res} + AT^{\alpha}}$ near the metamagnetic transition region. $\boldsymbol{\alpha = 1}$ persists in the lower field $\alpha = 2$ recovered at both low and high fields, and $\alpha < 2$ only exists in a narrow field window [4].

1.2.2 Properties of $Sr_3(Ru_{1-x}Mn_x)_2O_7$

Mn doping provides a controlled way to explore the intrinsic magnetic and electronic instability of $Sr_3Ru_2O_7$. Mathieu et al. found that in $Sr_3(Ru_{1-x}Mn_x)_2O_7$, the RuO_6 octahedral rotation decreases with increasing x [42]. Density functional theory (DFT) calculations also confirm that octahedral variations are responsible for the different magnetic and electronic properties of bulk $Sr_3Ru_2O_7$ [43]. As x increases, there are magnetic and metal to insulator (MIT) transitions coupled to the octahedral rotation, and the two transitions gradually separate, suggesting a mixed Mott and Slater typed MIT [44]. The MIT also coincides with the onset of the AF island around Mn, rather than forming a long-range AFM correlation [42,45]. While the *E*-type AFM ground state is formed in the intermediate doping range of $0.12 < x < 0.16$, the T_M reaches a maximum at the optimum doped sample $x_c = 0.16$ ($T_M = 81$ K) [46]. Partial bulk phase diagram is shown in Figure 1.10a. Figure 1.10b shows that this AFM ordering has a two-dimensional behavior of the zigzag chain in

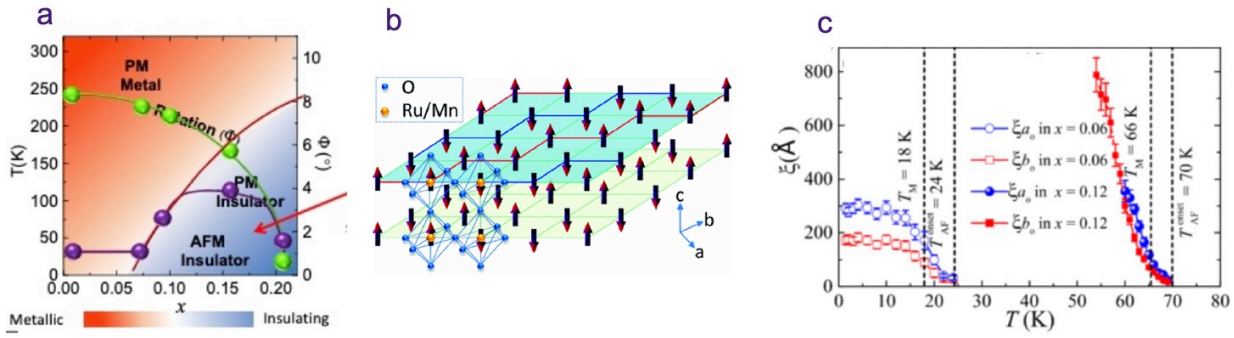

Figure 1.10. (a) Partial bulk phase diagram of $Sr_3(Ru_{1-x}Mn_x)_2O_7$ ($0 \leq x \leq 0.25$) showing structure-coupled magnetic/electronic properties [47]. The color bar in the bottom indicates different metallicity. (b) *E*-type AFM for $Sr_3(Ru_{0.84}Mn_{0.16})_2O_7$ with quai-2D zigzag chains marked on the top layer. (c) Magnetic correlation lengths obtained from elastic neutron scattering vs. temperature for $x = 0.06$ and 0.12 along the *a, b* direction. Figures are reproduced from Refs. [44,46].

the *ab* plane with a noticeable spin gap (~ 4 meV) . As seen in Figure 1.10c, the in-plane magnetic correlation length increases with increasing Mn (x). The correlation length is 200 Å for $x = 0.06$ and 800 Å for $x = 0.12$. This anisotropic behavior of ξ_{ao} and ξ_{bo} breaks the magnetic symmetry and forms a (2 × 1) magnetic unit cell [44]. Therefore, it is possible to see the correlation between the surface lattice structure and its magnetic properties.

1.3 Results from Prior Surface Studies on $Sr_3(Ru_{1-x}Mn_x)_2O_7$

Creating a surface causes a perturbation of the local density of states (LDOS). The formation of a surface breaks the translational symmetry and thus causes a perturbation in the system. Nobel laureate Wolfgang Pauli said, "God created the bulk, but the devil invented the surface." Electron correlations on surfaces are affected by cleavage planes and defects [48,49]. One example is the LDOS on the top few layers are affected by the reconstructed Si(111) surface [50,51]. So, the creation of surfaces disturbs the balance in CEMs, thus providing a different way to tune the system. The creation of surfaces drives the coupling of different degrees of freedom, resulting in different phase diagrams. The possible surface structural transitions include surface

segregation, surface melting, and surface reconstruction [52-54]. Also, the temperature of the structural transition, metal-insulator transition, and magnetic transition at the surface may be different from that of the bulk [55,56].

Our previous study found that the surface structure of $Sr_3(Ru_{1-x}Mn_x)_2O_7$ is fundamentally different from that of the bulk in the low-Mn region [11]. For the parent compound $Sr_3Ru_2O_7$, its surface has a unique octahedral tilt, as shown in Figure 1.11. For the surface octahedral rotation, the unit cell is marked as $\sqrt{2} \times \sqrt{2}R45^\circ$ relative to the bulk tet-(1×1). The LEED image in Figure 1.11a shows two perpendicular glide lines marked by red arrows. The surface octahedron also tilts along the edges. Without changing the primitive unit cell, the surface structure symmetry is broken to C_{2v}. The appearance of the fractional are represented by green circles in Figure 1.11b, and along these spots a glide line is broken [57]. For the quantitative analysis of the $Sr_3Ru_2O_7$ surface structure, it is shown that the surface octahedron has a high RuO_6 rotation angle at $\cong 11^\circ \pm 3^\circ$, and the tilt is around $2.6^\circ \pm 0.8^\circ$ at 86 K. The surface phase is summarized in Figure 1.12, and the tilt of the surface is considered to decrease with *x* by analysis of the intensity of the fractional spots in LEED image. The surface octahedral tilt favors the insulating phase at low doping regions [43]. In contrast, the surface conduction is better when the octahedra rotated at a higher angle. The surface metallicity shows tendencies opposite to the bulk's behavior from bulk from fitting the HREELS spectra with Fano *q* parameter. The surface is insulating while the bulk is metallic [58]. However, these surface measurements are far from complete. The LEED I-V analysis was performed only on undoped $Sr_3Ru_2O_7$ surfaces, and the detailed $Sr_3(Ru_{1-x}Mn_x)_2O_7$ surface structure at higher Mn concentrations is not known. The low temperature and the surface properties corresponding to the bulk AFM insulating phase are also investigated.

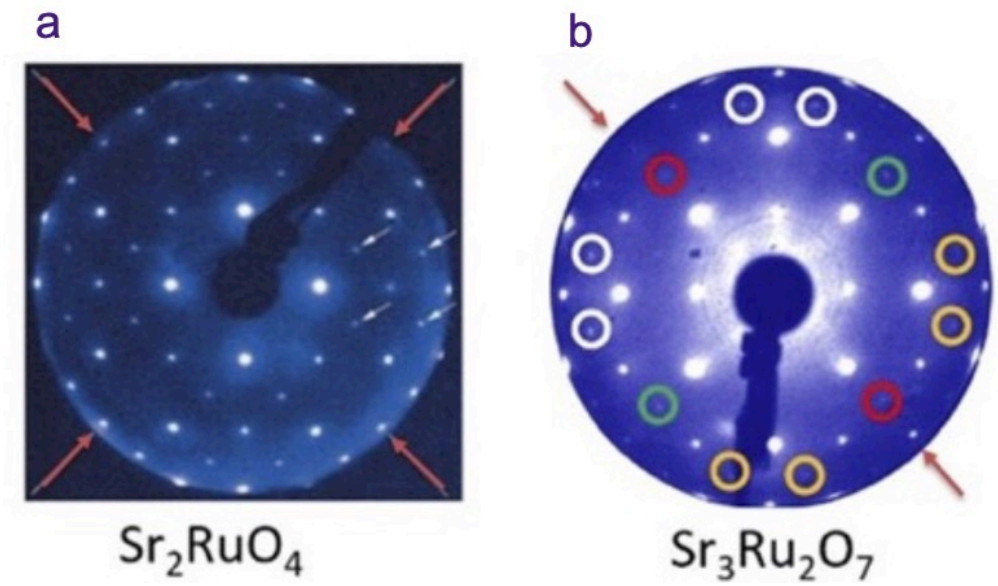

Figure 1.11. LEED diffraction patterns of different surface structures for single-layered Sr_2RuO_4 and bilayered $Sr_3Ru_2O_7$. (a) Octahedral rotation in Sr_2RuO_4 creates two perpendicular glide lines marked with two red arrows at 80 K. (b) Room temperature LEED pattern of $Sr_3Ru_2O_7$ shows one broken glide line as a result of surface-induced tilt. The fraction spots sensitive to the surface-induced tilt appear in the green circle, indicating the glide line symmetry along this direction is broken on the surface. Figure adapted from [56,58].

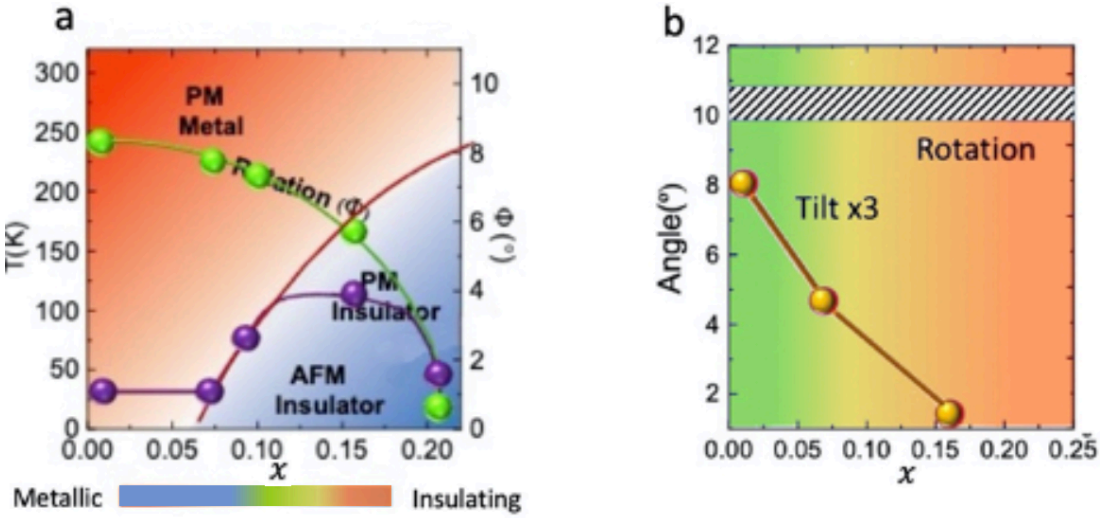

Figure 1.12. Comparison of the bulk and surface phase diagrams on $Sr_3(Ru_{1-x}Mn_x)_2O_7$ ($0 \leq x \leq 0.25$) at 86 K. (a) Bulk phase diagram for $Sr_3(Ru_{1-x}Mn_x)_2O_7$ ($0 < x < 0.25$). (b) Surface phase diagram for $Sr_3(Ru_{1-x}Mn_x)_2O_7$ ($0 \leq x \leq 0.25$) at 86 K. Figure is reproduced from Refs. [11,47].

1.4 Focus of This Dissertation

Previous data on the surface structure and properties of $Sr_3(Ru_{1-x}Mn_x)_2O_7$ are far from complete, and the structure of the bulk at low temperatures is not conclusive. Therefore, the primary focus of this dissertation is to provide a complete phase diagram of the $Sr_3(Ru_{1-x}Mn_x)_2O_7$ surface at low temperatures and in large Mn-doped regions. The $Sr_3(Ru_{1-x}Mn_x)_2O_7$ structure evolves with the Mn impurities. In Chapter 3, we will review the single-crystal X-ray diffraction refinement of $Sr_3(Ru_{1-x}Mn_x)_2O_7$ (x = 0.08, 0.16, 0.23, and 1) to understand the bulk structural changes at room and low temperatures with varying x. The magnetic transition appearing in bulk may be accompanied by a change in its structure. The surface may undergo a metal-insulator transition or a magnetic transition at a temperature that differs from bulk. In the bulk AFM insulating phase, the surface may also change. Therefore, in Chapter 4, we first characterize the sample surface symmetries evolved with x at 77 K. Quantify the detailed surface structure through LEED I-V calculations. The surface lattice dynamics with x is determined by the phonon peak shape and the energies from the collected HREELS spectra. The response of the surface to the bulk AFM is explored through measurements of the structure and physical properties of the surface at $Sr_3(Ru_{0.84}Mn_{0.16})_2O_7$ with temperature dependence.

Chapter 2. Experimental Techniques

Several bulk and surface characterization techniques are used in this thesis. Various temperature dependent single-crystal X-ray diffraction (SXRD) is collected for the bulk structural determination, and refined bulk structure is obtained at various temperatures. Reciprocal-space surface symmetry and structure refinement are done with low energy electron diffraction (LEED) measurements. Real-space surface electronic structure and local symmetry are probed with scanning tunneling microscopy/spectroscopy (STM/S). The surface plasmons, lattice vibrations (phonons), and inter/intraband electronic transition, information in the scattered electrons, are probed through HREELS techniques. In this Chapter, we will provide the working principle of each technique and the experimental setup.

2.1 Single Crystal X-ray Diffraction (SXRD)

Structural characterization is a prerequisite to understanding the physical properties of any crystalline material. X-ray diffraction (XRD) is a powerful method generating detailed structural information on the atomic scale. The availability of conventional in-house commercial X-ray sources with higher intensity leads to rapid crystallography study [59]. Sample preparation for the XRD experiments can be in either finely ground powder or single crystal form. The crystal structure determinations from both forms yield comparable results. The powder form is more beneficial for organic molecules or amorphous solids.

Single crystal XRD provides detailed geometric details for the determination and refinement of the crystal structure, including bond lengths and angles. After the structural model refinement is complete, the residual density map is probed. A small fragment of the $Sr_3(Ru_{1-x}Mn_x)_2O_7$ crystal, with approximate dimensions 0.3mm × 0.3mm × 0.3mm, was used for the measurement. We collected the $Sr_3(Ru_{1-x}Mn_x)_2O_7$ data on a Bruker D8 QUEST diffractometer with

a Mo Kα radiation (λ = 0.7107Å) and scattered intensities were measured with a PHOTON II detector. An Oxford helium cryo stream controller is equipped. The diffractometer is shown in Figure 2.1. Measurements were taken at 300K and 28K with a 5K/minute cooling/warming rate for each sample. Waiting time of 30 minutes is applied before each data collection for temperature stabilization after reaching the designated temperature set point. In order to estimate the quality of the sample, a set of XRD images (frames) is collected, and then, the XRD frame corresponding to the diffraction data is used to judge the crystal quality. The Bruker SAINT software integrates all frames and yields nearly 2000 reflections; the total measured reflections merged to independent reflections with R_{int}. The sample exposure time was ~2 hours for each measurement with θ range between 2 and 35 degrees. After data collection, absorption effects were corrected with a multiscan method. The SHELX package is used for analysis and refinement of the final crystal structure from approximately 250 reflections in the WinGX program [60,61]. The brief flowchart of the SHELX algorithm with main functions and applications of subroutines is drawn in Figure 2.1b [61].

The program, XPREP, is used to check various possible macro-symmetric operation elements, such as the screw axis, glide plane, etc., and determine the crystal space group. Cell geometry and space group of the merged diffraction data set was stored in momo-new.hkl; momo-new.ins is the operational command and expected atom type file for SHELX. Since the missing phase information in the scattered X-ray intensities, the phase angle problem is solved by Rietveld refinement to convert intensities to model the structure [62,63]. The final evaluation of the agreement between the experimental and theoretical structural models comes from the R factor. Whether the refinement is physically meaningful should be checked with a preliminary judgment of chemical rationality of the structural model (e.g., specific values of the bond length and angles).

All target parameters are refined and converged [64,65]. Finally, a missing symmetry test is checked with the embedded ADDSYM test in PLATON [66].

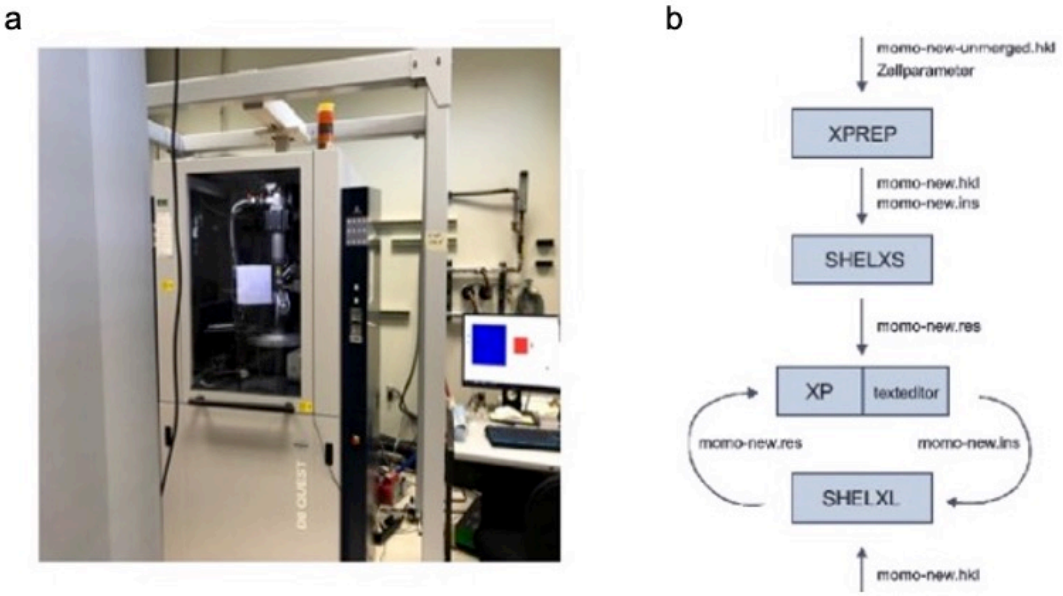

Figure 2.1 (a) Bruker D8 Quest X-ray crystallography system operating at liquid helium temperature. (b) Brief algorithm of SHELXS program solving single-crystal structures by single-crystal X-ray diffraction, the Figure is adapted from Ref. [61].

2.2 Low-Energy Electron Diffraction (LEED)

2.2.1 Diffraction Pattern Analysis

For the surface characterization, all surface preparation and experiments were done in an ultra-high vacuum (UHV) system to ensure a contamination-free surface during the experiment [67]. Our combined LEED-HREELS system runs under the normal pressure of ~1.0×10^{-10} Torr, as shown in Figure 2.2. There is a preparation chamber on the left side of the main LEED-HREELS chamber; sample loading/unloading, sputter/annealing, and other surface treatments are done in the preparation chamber. The main chamber has a vertical manipulator with an omicron LEED installed on the top part, and HREELS is shielded in the bottom cylindrical chamber. Samples are cooled by a liquid nitrogen cryostat; a thermal diode is mounted on the sample stage for precise

temperature measurements, and a custom double-layered oxygen-free copper thermal shield is designed for LEED measurements at 20K. LEED is surface-sensitive and used to determine the lattice symmetry and surface atomic positions. Our Omicron LEED has four grids of which grids 1 and 4 are grounded, and the remaining two grids have voltages slightly less than that of the incident beam voltages and are used to filter out electrons with energy loss.

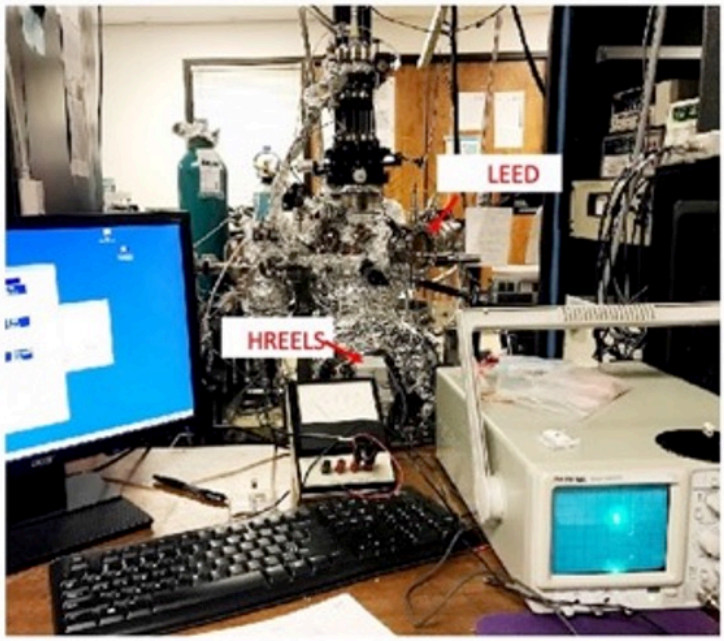

Figure 2.2. Photo of our sample preparation and LEED-HREELS chamber.

LEED has been widely used to solve complex structural results. Electron diffraction was first observed on nickel single crystals at Bell Labs [68]. The theory of electron diffraction is attributed to de Broglie, and the wavelength of an electron is related to its momentum, similar to a photon:

$$\lambda = \frac{h}{p} = \frac{h}{mv} = \frac{h}{\sqrt{2mE}} \quad (2.1).$$

Where E is for the collimated low energy electron beam (20-600eV), and h is Planck constant. With this equation handy, the electron has a wavelength of 1Å with a 150.4eV kinetic energy:

$$\lambda_{\mathrm{e}}[\text{Å}] = \sqrt{\frac{150.4}{E(\mathrm{eV})}} \tag{2.2}.$$

In addition, e, m are the charge and mass of the electrons. Based on the constructive diffraction condition:

$$dsin\theta = n\lambda \tag{2.3},$$

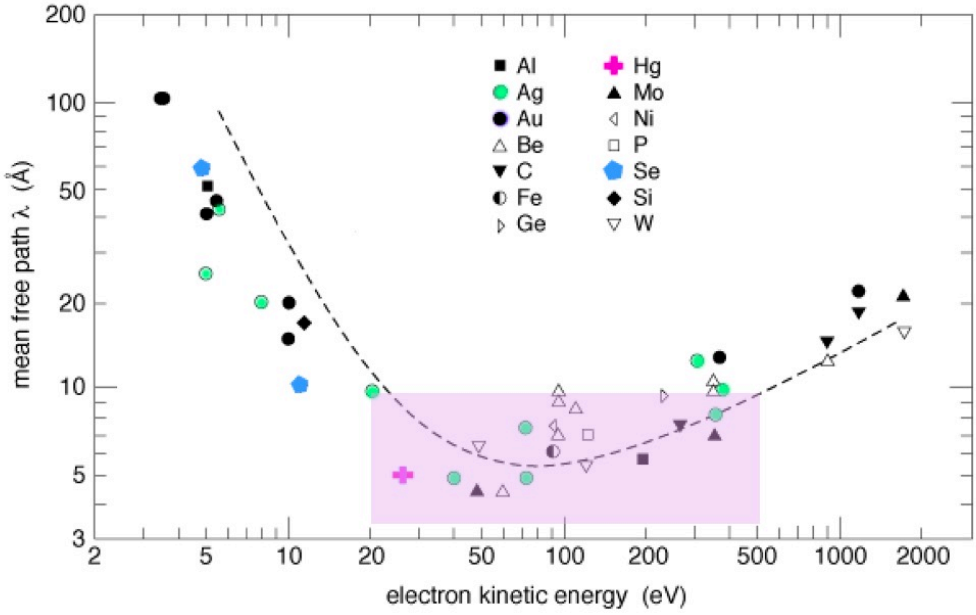

Figure 2.3. Universal curve of the energy-dependent inelastic mean free path of electrons. In this case, the purple rectangle marks the IMFPs in the low electron kinetic energy region, where it can be seen that the LEED has an electron penetration depth of about 6-10 Å . The figure is adapted from the literature [69].

at the same electron energy (λ is the same), for the same order of diffraction n, $sin\theta$ is proportional to 1/d, meaning the smaller lattice constant, the greater angle of diffraction. For different λ, sinθ ~ $1/\sqrt{E}$ for the same crystal, thus smaller energy, greater diffraction angle. The diffraction pattern is symmetric for positive and negative n when only the first layer is considered.

The penetration depth of the incident electrons for the sample is related to their kinetic energy of the electrons. As shown in Figure 2.3 the inelastic mean free path (IMFP) of the low kinetic energy electrons of LEED is about 5 to 10 Å in their energy range, and this penetration depth is equal to the length of the bilayer octahedra of surface ruthenium, such that the bulk atoms do not contribute to the LEED mode. X-ray and electron diffractions have similar diffraction principles, but LEED is often used for the surface two-dimensional symmetry operations due to lower electron energy and limited penetration depth. A LEED diffraction pattern in the 2D reciprocal space is a cut of the diffraction Ewald sphere. The Ewald sphere has a radius of the incoming electron wave vector and built-in 3D reciprocal space. By analyzing 2D patterns, the surface orientation and lattice symmetry are determined immediately. The two-dimensional surface lattice symmetry can be determined from the diffraction patterns showing on LEED florescent screen. The scattered electron obeys the energy and momentum conservation and can be written in the reciprocal lattice vector G:

$$E_i = Es \tag{2.4},$$

$$Q = K_i - K_s = G_{l1l2} \tag{2.5}.$$

The coherent length of LEED electrons is about 100 ~ 200 Å [70], where the ΔE and beam divergence limit the electron coherence. This length marks a circle with this radius where electrons are coherently scattered, and diffraction patterns are superimposed. Hence, the resultant patterns can be a mixture of different domains, ordered and disordered regions. For example, the 1×2 surface phase observed by LEED may be a mixture of different domains of 1×2 and 2×1 superlattices. Figure 2.4 shows an example from $Ca_{1.5}Sr_{0.5}RuO_4$ (001) [71] and $IrTe_2$ [72], where the surface has a sharp (1×1) pattern and two glide lines marked by the white arrows. The observed pattern in Figure 2.4a has a *p4gm* symmetry in contrast to the *p2gg* plane; Figure 2.4 b shows $IrTe_2$

surface has a mixture of 8×1 and 6×1 phase. An overall view of the pattern symmetries on $Ca_{2-x}Sr_xRuO_4$ was given in Figure 2.5. If the surface octahedra are not distorted in $Ca_{1.5}Sr_{0.5}RuO_4$ (001), the bulk truncated surface unit cell can be represented by the Figure 2.5a. The simulated diffraction pattern in Figure 2.5b shows diffraction patterns of all integer spots. When there is a surface reconstruction induced by octahedral rotation like in $Sr_3(Mn_{0.16}Ru_{0.84})_2O_7$, the reconstructed surface unit cell is shifted with one square of the original unit vector and generate a $(\sqrt{2} \times \sqrt{2})\ R45^\circ$ unit cell like in Figure 2.5c in which two glide line symmetries (translational reflection symmetry) are marked with two blue dashed lines. The resulting structure factor has a π phase mismatch, and fractional spots extinguish along the glide line direction as marked in the white arrow in Figure 2.5d. Furthermore, adding in the octahedral tilt distortion in Figure 2.5e,

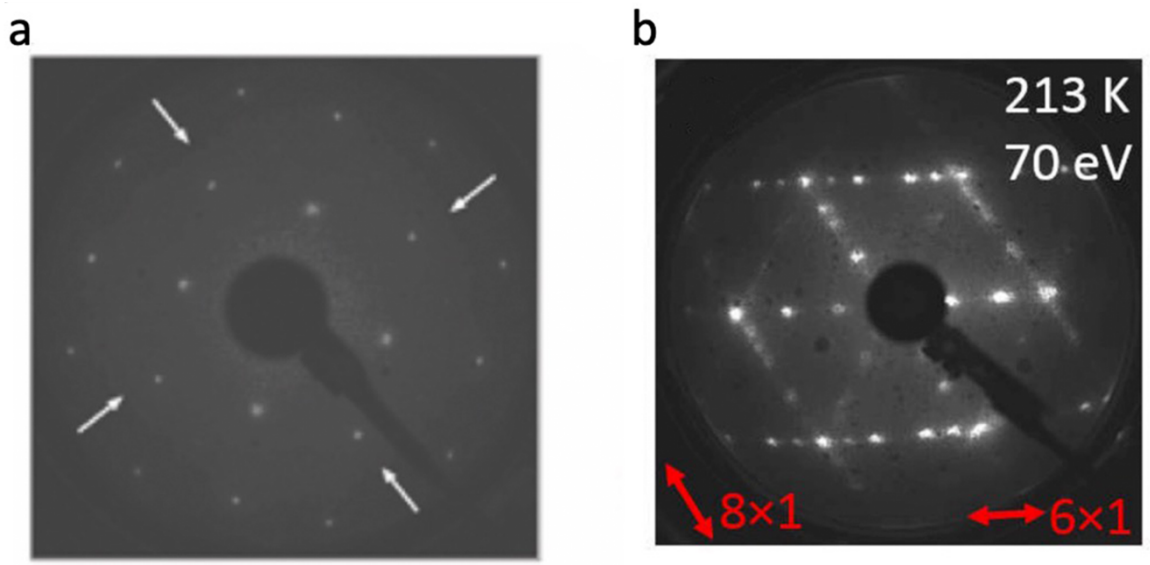

Figure 2.4. LEED diffraction patterns showing (a) un-reconstructed surface of $Ca_{1.5}Sr_{0.5}RuO_4$ with two glide line symmetry. (b)Coexistence of 6 × 1 and 8 × 1 phase on the surface of $IrTe_2$.

different atomic heights are compared to the surface in blue (below the surface without octahedral tilt) and orange (above the surface without octahedral tilt). Only one glide line symmetry remains which is along the broken symmetry line. The top and bottom atoms are at different positions, and

the fractional spots re-appeared in the diffraction pattern along the broken symmetry direction as seen in Figure 2.5e. Electron incidence angle also needs to be determined with the method described in [73]. We collected the LEED data in an approximated normal incident angle, the electron incident angle normal to the surface is determined with Newton's method for two chosen diffraction spots. For this, we use Jacobian matrix, J, with the procedure running for ith iteration until $\Delta\theta$ and $\Delta\varphi$ are less than a defined value.

$$\begin{bmatrix} J_{1\theta} & J_{1\varphi} \\ J_{2\theta} & J_{2\varphi} \end{bmatrix} \begin{bmatrix} \Delta\theta \\ \Delta\varphi \end{bmatrix} = \begin{bmatrix} -f_1(\theta_i, \varphi_i) \\ -f_2(\theta_i, \varphi_i) \end{bmatrix} \quad (2.6).$$

For an approximated experimental determination of normal incidence conditions, we tracked the real-time intensity-voltage curves for the symmetry equivalent spots. When the plots are in a good agreement, the normal incidence condition is met. Otherwise, we adjust the sample positions and repeat the procedure.

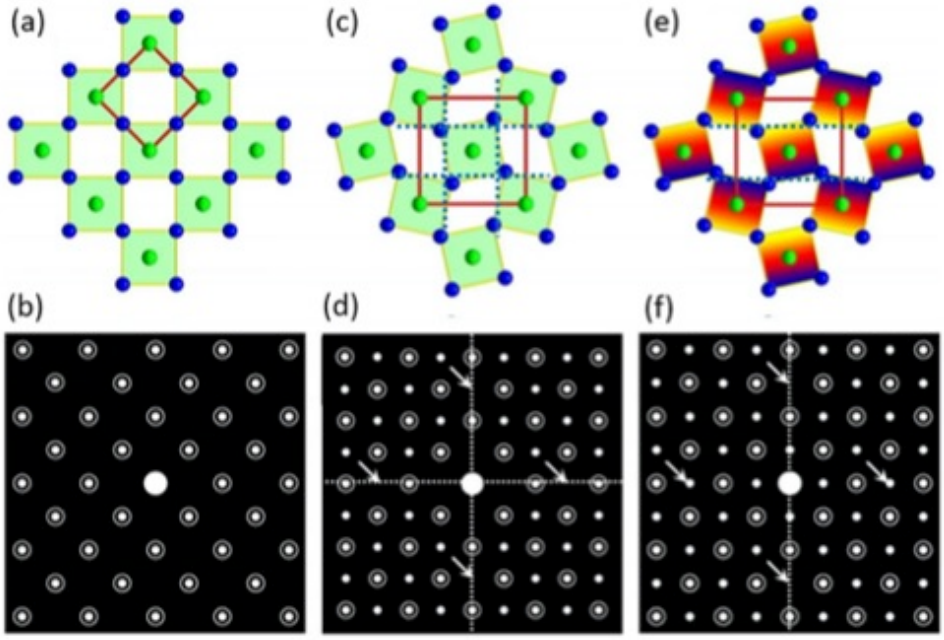

Figure 2.5. Illustration of the surface unit cell of $Ca_{2-x}Sr_xRuO_4$ (001) surface and corresponding simulated diffraction patterns. (a-b) Bulk truncated square surface lattice marked by the red square, and diffraction patterns show all integer spots. (c-d) For surface octahedra rotational distortion, the reconstructed surface unit cell is marked with an enlarged red square. Two perpendicular glide line symmetries are marked with the dashed white line. Along the line, fractional spots are distinguished. (e-f) For surface octahedra with rotation. One glide line is broken because of rotation and tilt, and the broken symmetry is reflected with emergent fractional spots along the missing glide line direction. This figure is adapted from Ref. [74].

2.2.2 Intensity vs. Voltage (I-V) Analysis

LEED diffraction patterns contain information of the surface atomic movements relative to the bulk and can quantitatively obtain the surface structure on an atomic scale. Van Hove has developed a detailed LEED I-V analysis on most simple surfaces [75], and both structural and non-structural parameters (e.g., Debye temperatures) are used in the surface structure modeling. During the LEED analysis's optimization process, the trial structures are created based on the deviations in atomic positions and compared with the experimentally collected I-V data. An indirect trial-and-error search procedure is employed for the optimized structure. The refined structure reliability is calculated with Pendry R_p factor by comparing the experimental and theoretical I-V curves [76]. Estimation in crystal potential can be a complicated process since a variety of shapes and sizes of the different atomic orbitals overlapped on the surface. Furthermore, we used muffin-tin (MT) potential approximation to estimate the crystal potential with a flat interstitial potential connecting each spherical well potential. The majority of transition metal oxides were solved successfully with the MT model [71]. For the one-dimensional kinematic approximation, the incident electrons scatter only on the very top layer. The incident electron plane wave $A_i = A_0 e^{-ik_i x}$ is transmitted along the x-direction and weakly scattered (kinematic approximation) once from a semi-infinite row of identical atoms with equal interlayer spacing d. However, the actual resultant scattered beams we collected are the summation of all reflected beams from every atomic layer j plus the travel back of the next layer j+1 transmitted beam,

$$A_s = A_0 \sum_{j=0}^{\infty} \mathrm{RT^{2j}e}^{ik2d_j} e^{-ikx} = A_0 \frac{i\sqrt{1-T^2}}{1-T^2 e^{ik2d}} e^{-ikx} \quad (2.7),$$

where T, and R are the electronic transmission and reflection coefficients. An electron traveling between the atomic layers of layered materials, it will experience an inner potential: $V_0 = V_{or} +$

iV_{oi} induced by the interstitial charge density as a part of the MT potentials. The change in momentum of the reflected electron can be expressed by the following equation:

$$k = \sqrt{\frac{2m(E-V_0)}{h^2}} = 2\pi\sqrt{\frac{E-V_{or}-iV_{oi}}{150[eV]}} \quad (2.8).$$

The inner potential's real and imaginary components are held constant, and larger real V_{or} can shift the peak position to higher energy. The imaginary part V_{oi} is used to denote electron attenuations where higher V_{oi} increase the peak width. Typical starting values are V_{or} ~ 16 V, and *a* simple phenomenological model is proposed for V_{oi} that reproduces its relation to the "Universal Curve" of the electron mean free path. In this case, the SATLEED code subroutine was modified to incorporate the phenomenological model, assuming a constant V_{oi} = -5 V for most TMOs' surfaces. Also, we used an energy-dependent Slater-like exchange term V_{xc} to account for the exchange and correlation effects between the incident electron and the surrounding electron sea on the sample surface. The exchange-correlation potential V_{xc} is defined as

$$V_{xc} = \left(\frac{\sum(\rho,r_s)}{\sum(k_F,r_S)}\right) u_{xc}(r_s) \quad (2.9),$$

which is a function of the distance r_s between the electrons at each scattering center, local electron density ρ, and added to the inner potential as an energy-dependent term:

$$V_o(E) = V_{oc} + V_{xc}(E) \quad (2.10).$$

We try to understand the energy-dependent MT inner potential in our calculations. Figure 2.6 provides an illustrative example of the computed MT potential for a 1D model in which such energy dependence has a pronounced effect on the shape and position of the calculated I-V curve.

The term shows an improved solution when simulating the actual MT potential, with the red energy-dependent and exchange-effect-derived $V_o(E)$ showing no anomalous contraction unlike what is seen in the blue curve V_o.

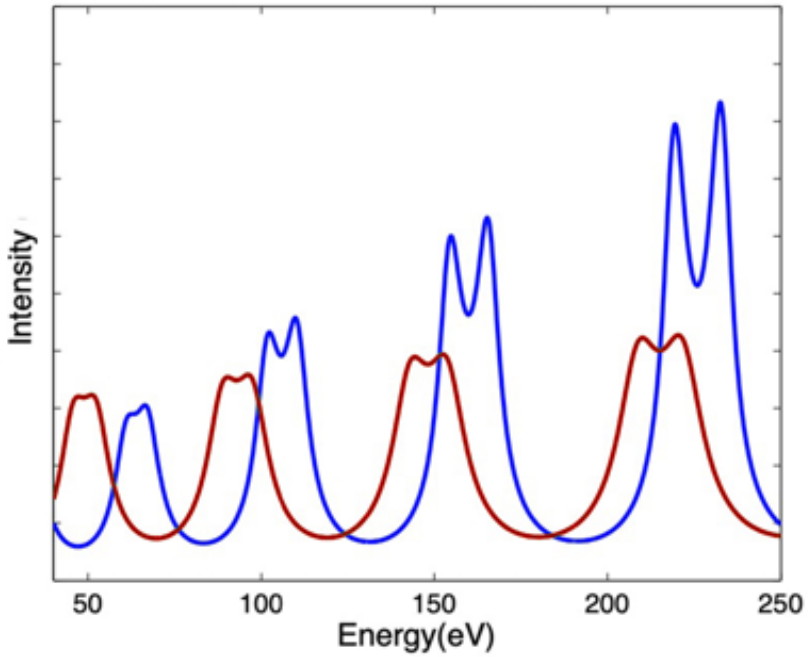

Figure 2.6. Comparison of the energy-dependent $V_o(E)$ marked in red and V_o marked in blue of the one-dimensional model.

In our Optimized Muffin-Tin (OMT) model proposed by Rundgren [77], the MT spheres of atomic species have a muffin tin radius r_{mft} and connected by energy-dependent flat potential $V_o(E)$. The MT total potential consists of two parts: superposition of the overlapped free-atom densities and the charge outside the muffin-tin. Within the radius of the atomic sphere $r_{rmf} < r < R$, the MT potential can be written:

$$V_{or}(E) = \sum_{i=1}^{N} \omega_i \int_r^R \left[V_{fei}(r) + V_{xci}(E,r)\right] 4\pi r^2 dr. \quad (2.11),$$

V_{fei} is the fast electron potential as a supplement term to the exchange $V_{xci}(E,r)$. So, at the muffin tin boundary, an energy-dependent potential step is created. The size of the r_{rmf} is

an adjustable parameter to minimize this potential step for calculating the corresponding phase shifts in this optimized MT approach. Such an example of phase shifts for Mn is provided in Figure 2.7 without any resonance feature. The incorporation of the energy-dependent inner potential has a noticeable improvement on the R_p values in the structural refinement results for the TMOs compared with that using the constant V_o [71].

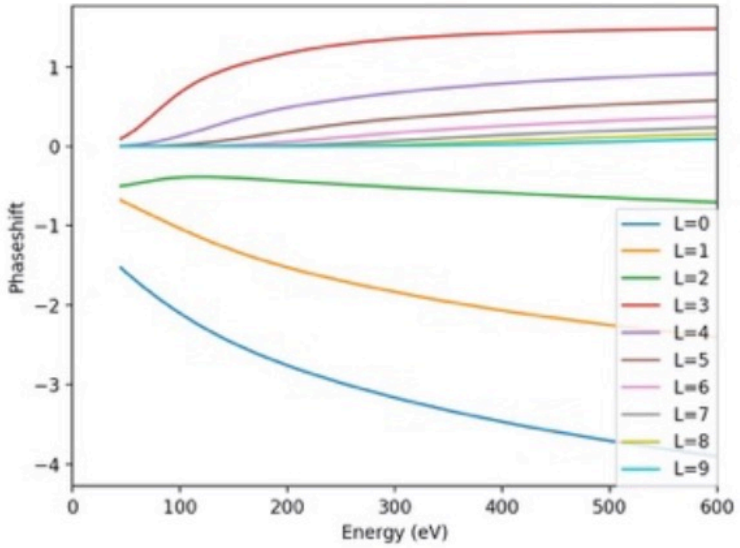

Figure 2.7. Calculated phase shifts the optimized MT potential method.

Calculating the LEED spectra is quite complicated. We must find the *t*-matrix storing the scattering amplitude for each element, the layer-diffraction matrix, and the multiple reflections occurring between the layers. Multiple scattering events occur in the interlayer and are calculated with the Renormalized Forward Scattering (RFS) method [78,79]. As shown in Figure 2.8, this RFS schematic conceptualization assumes that there is one reflection from each layer for the first-order perturbation and three reflections of the incident beam in the interlayer. This approach applies to our case when defining several composite layers, as shown in Figure 2.9, for the double layered $Sr_3(Ru_{1-x}Mn_x)_2O_7$. The interlayer spacing between each composite layer is more extensive

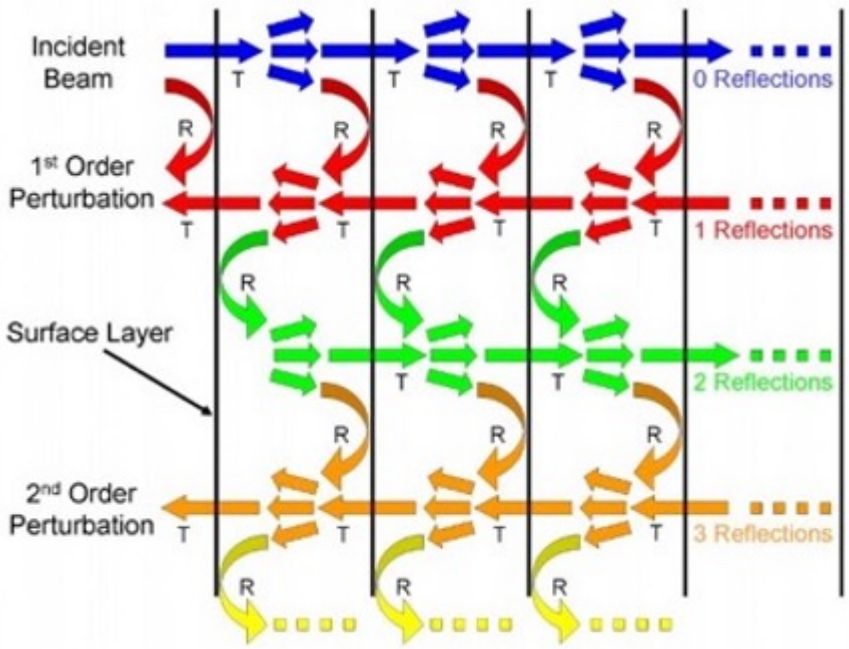

Figure 2.8. Schematic representation of the RFS method for the multiple scattering events in the interlayers. Figure adapted from Ref.[20].

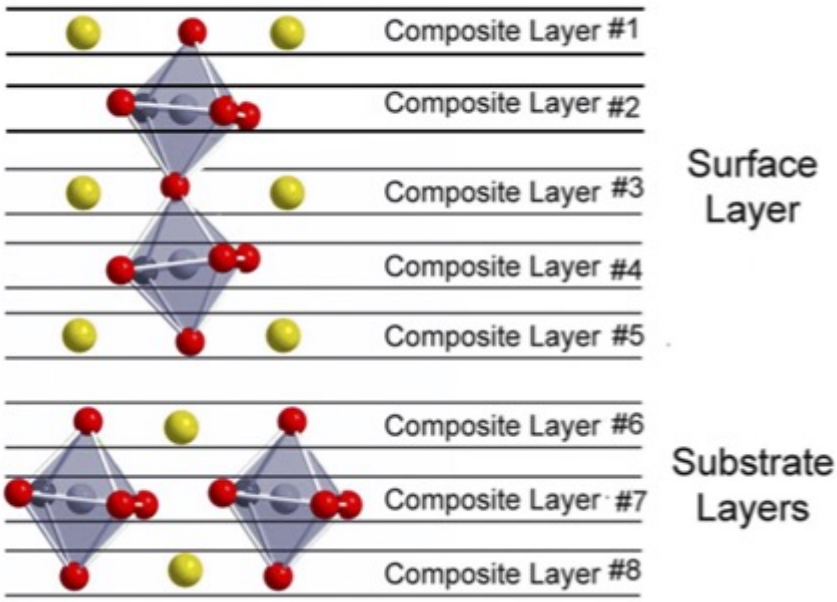

Figure 2.9. Schematic structure of the $Sr_3(Ru_{1-x}Mn_x)_2O_7$ used in the RFS method calculation. The doubled layered structure network is split into several composite layers. The layers are numbered consecutively from surface layers into the substrate layers.

than 1Å for the RFS method to converge. For our $Sr_3(Ru_{1-x}Mn_x)_2O_7$ samples, the calculation requires an additional Average T-matrix Approximation (ATA) method since the Mn sits in the same host Ru site [80]. The ATA approach is obtained via the mean-field approximation of the relative cation concentrations where the Ru and Mn are assumed identical. Finding the global optimal solution of the surface structure is done by comparing the difference between the theoretical and experimental I-V curves. We used the Differential Evolution (DE) algorithm for testing the tracing process, where the final structure (global minimum R_p) can be obtained by iteratively updating the value of Pendry factor R_p. The methodology for modeling the structure of the reference surface is further explained in the results section. The relative peak positions significantly influence R_p values, contributing to the equal weight of the small peaks and the large peaks [79]. These values R_p were calculated by taking into account several functions: the L function is the IV spectra intensity $I(E)$ derivatives, and the Y function depends on the imaginary part V_{oi} of the inner potential:

$$L = \frac{1}{I(E)} \frac{dI(E)}{dE} \tag{2.12}$$

$$Y = \frac{L}{1+V_{oi}^2 L^2} \tag{2.13},$$

Y_{exp} and Y_{the} represent the Y functions calculated from the experimental and theoretical I-V curves, respectively. We then calculate the R_p,

$$R_p = \frac{\int \left(Y_{exp} - Y_{the}\right)^2 dE}{\int \left(Y_{exp}^2 + Y_{the}^2\right) dE} \tag{2.14},$$

the total R_p is obtained based on the weighted individual beams *N,* which depend on the selected energy range ΔE to ensure all the inequivalent beams are equally weighted. The larger number of beams and energy range typically yields the most reliable refined structure:

$$R_P^{Total} = \frac{\sum_{i=1}^{N} (R_p)_i (\Delta E)_i}{\sum_{i=1}^{N} (\Delta E)_i} \quad (2.15).$$

A complete dynamical calculation is needed to obtain the best trial structure, and uncertainty in the LEED-IV analysis is written as the variance of the entire energy range function. V_{oi} and the minimum determined

$$R_{P\,min}^{Total} : \sigma = (R_{P\,min}^{Total}) \sqrt{\frac{8|V_{oi}|}{\Delta E}} \quad (2.16).$$

2.4 High-Resolution Electron Energy Loss Spectroscopy (HREELS)

HREELS is used to investigate the surface lattice dynamics by analyzing inelastically scattered electrons. The overall measured energy loss ranges from 2meV to about 1eV. From the LEED experiment, we could observe background intensity from both disordered crystal surfaces and inelastically scattered electrons where the scattered electrons and the wave vectors are notably different. The inelastically scattered electrons contain information regarding quasiparticle excitations on the surface. Thus, the HREELS can be widely utilized to investigate lattice vibrations (phonons), surface plasma, and interband electronic transitions on the surface.

The working mechanism is that an emission system injects a monoenergetic beam of electrons with energy E_i and momentum k_i incident on the sample surface at an angle θ_i. The electron can be inelastically backscattered into the vacuum with energy E_s, momentum k_s and at an angle θ_s. The general energy conservation law can be re-written to reflect the inelastic conditions: $E_s(k_s) = E_i(k_i) - \hbar\omega(q_{//})$, where $\hbar\omega = \Delta E$ is the energy of the surface excitation and $q_{//}$ is the momentum transfer parallel to the surface satisfying the momentum conservation law:

$$k_{s\parallel} = k_{i\parallel} - q_{\parallel} \pm G_{h,k} \quad (2.17).$$

$G_{(h,k)}$ is a two-dimensional reciprocal lattice vector parallel to the surface, and the excitation energy is usually in the range of tens of millivolts in correspondence to the incident monochromatic electron beam with meV energy resolution.

The description of HREELS theory and the apparatus design philosophy is presented in [81,82]. Typically, if the incident and scattered electrons are restricted in a plane, we only measure the momentum transfer parallel to the surface. The equation for such a transfer parallel to the surface can be simplify written as:

$$q_{\parallel} = \frac{\sqrt{2m_e}}{\hbar}(\sqrt{E_i}sin\theta_i - \sqrt{E_i - \hbar\omega_v}sin\theta_s) \pm G_{hk} \quad (2.18).$$

The two angles θ_i and θ_s with respect to the surface normal here are for the incident and scattering, respectively. Thus, we could set a specific momentum transfer by varying incident energy and angle, and we usually rotate the analyzer to change the scattering angle in an one-degree increment. The scattered low energy electrons are categorized into two different regimes: dipole scattering and impact scattering [83]. Dipole scattering is a forward scattering event, and it occurs when the vibration is excited by the electric field of the incoming incident electrons when the scattered beam is very near to the specular direction ($\theta_i = \theta_s$). The dipole scattering process results in a quasi-isotropic distribution of the scattered electrons and occurs near the surface by the surface excitation dipole field, as illustrated in Figure 2.10a, the scattering cross-section is a function of dipole field at the surface, incoming and scattered electron velocities, the cross-section is about the square root of the incident energy. By treating this situation with a semi-classical dialectical theory, a selection rule is deduced where vibrations with a dipole moment normal to the surface can be excited. Only active infrared modes along the *z*-direction can be observed. We simulated the scattering cross-section versus the specular geometry deviation in Figure 2.10b with the equation for an electron transit from the ψ_i to ψ_s state.

$$\frac{ds}{d\Omega} = \left(\frac{4mue}{h^2}\right) v_s/v_i \ \frac{1}{\cos\theta_i} \left|2\pi^2 \left\langle \psi_s \left| \frac{z}{|X|^3} \right| \psi_i \right\rangle\right|^2 \quad (2.18).$$

The elastic peak has highest intensity at the specular direction ($\theta_s = \theta_i$) and has a higher incoming electron energy. The cross-section becomes flat and negligible after 4 degrees angle deviation from the specular direction. The impact scattering is inelastic from the direct interaction of incident electrons with ion cores, which is a short range indicates isotropic scattering. Electrons are scattered further away from the specular direction, and the scattering cross-section increases with the beam electron energy. Symmetry considerations also result in specific selection rules: if the scattering plane coincides with a mirror plane of the surface, all modes with atomic displacements perpendicular to the mirror plane will not be excited. The odd modes are polarized entirely in the surface plane. Different vibrational modes can be excited by turning the analyzer to a non-specular direction, where the dipole regime disappears and the impact scattering is increasing.

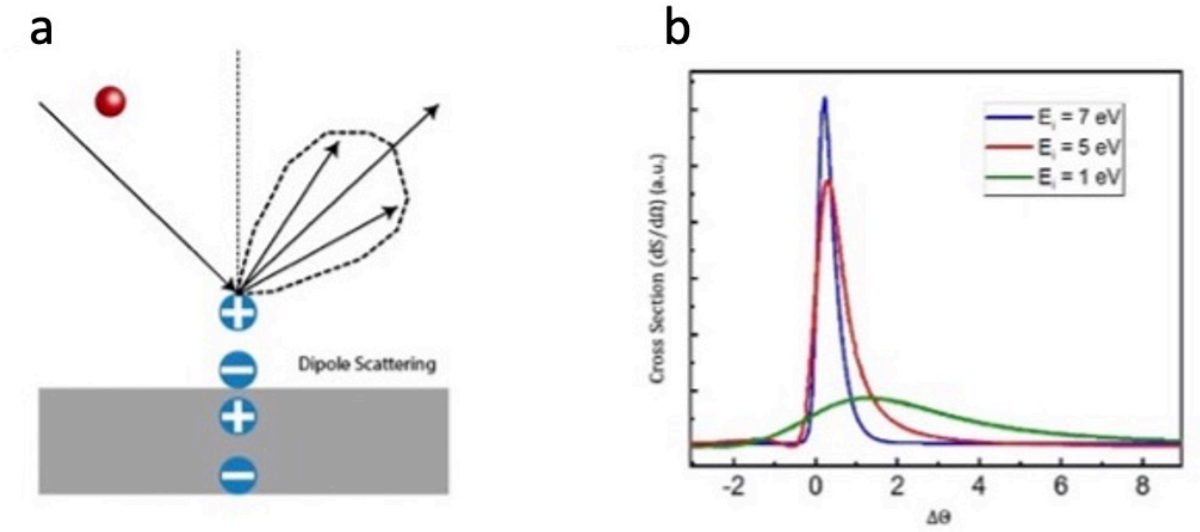

Figure 2.10. Dipole scattering process in HREELS. (a) Illustration of dipole scattering: dipole regime was limited to the specular direction, and electron was scattered by induced surface dipole field. (b) The scattering crossection is a function of incoming energy. The large inelastically scattered peak intensity in the vicinity of specular, and the peak intensity is proportional to the incoming electron energy.

Our LK5000 HREELS is a state-of-the-art spectrometer, and it is currently equipped with a multichannel electron energy analyzer with a guaranteed detector current $I_D \geq 10pA$ at 1.0 meV resolution under optimal condition as shown in Figure 2.11. Two consecutive electronic monochromators (coarse and fine) assemblies in HREELS are used to tune the electron beam's monochromaticity which are combined with a non-circular symmetric lens design (guide the electron trajectory path). After the sample surface reflects the electron beam, it goes through a fine analyzer first and then analyzed based on its energy loss. The fine analyzer also works just like the fine monochromators, and the weak energy loss signal is magnified by a channel electron multiplier operated at high voltage (> 1800V). The collected data is a counting rate with arbitrary units vs. energy loss spectrum with meV. A Lorentzian function standardly fits the loss peaks in the acquired spectrum. The peak center is the energy loss value, which is also the quasiparticle excitation energy, and the peak linewidth reflects the quasiparticle lifetime. If it is coupled with any other excitation, the linewidth will increase appreciably. Thus, these peaks could be phonons, plasmons, intra/interband transitions, and so on, depending on the energy and linewidth in different systems.

The MCA of ELS5000 has a maximum 70° off direct beam rotation angle to measure different momentum transfers on the sample surface. The quasiparticle excitation energy is measured when the analyzer is associated with a momentum transfer calculated from equation 2.18. There are various examples of HREELS dispersion measurements everywhere: Ref. [81] gives a simple physical picture to explain the negative surface-plasmon dispersion in which the energy loss peak is lower at higher $q_{//}$. Ref. [82] measures phonon dispersion. We measure surface phonons in a specular direction (thus, in the dipole scattering regime). The resulting spectrum has overtone peaks from the scattering process including a multi-scattering with surface phonons. EELS was

used to extract qualitative information regarding the surface metallicity with low energy excitation of electron-hole pairs across the Fermi energy. The intensity profiles of the optical phonons with scattering angles are plotted, and the surface metallicity can be derived from the peak asymmetry.

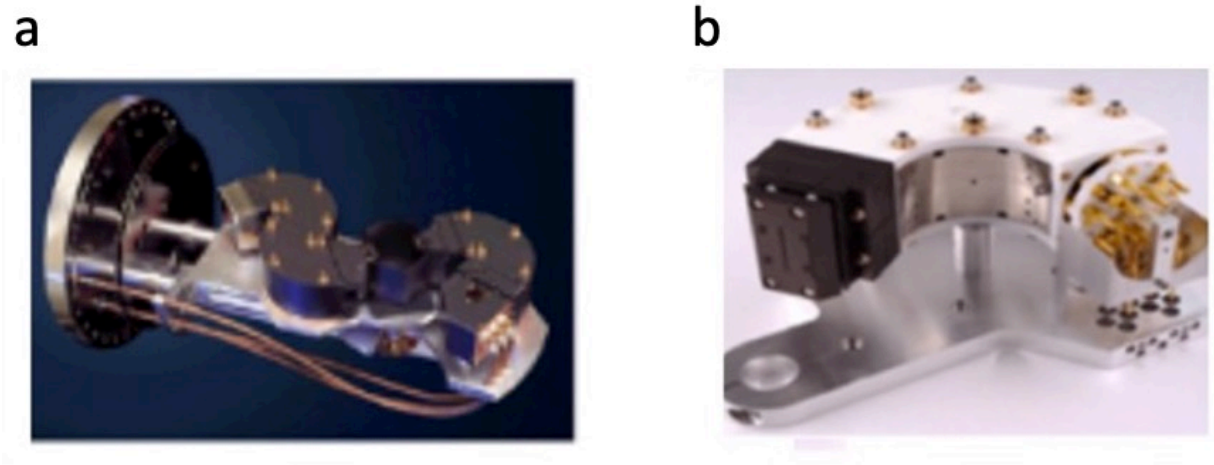

Figure 2.11. (a) Photograph of our LK5000 EELS, including the electron monochromator, guide lens and sample chamber in the middle. (b) Multichannel electron energy analyzer model EA5000MCA.

2.5 Scanning Tunneling Microscopy/Spectroscopy (STM/STS)

The Scanning Tunneling Microscopy (STM) was invented in 1981 at the IBM Zurich Research Laboratories in Switzerland, and its development brought Gerd Binning and Heinrich Rohrer the Nobel Prize in Physics in 1986 [84]. STM shows the surface topography with individual atomic resolution based on quantum tunneling. STM works well on conducting materials and can be extended to semiconducting TMO surfaces. With the STM tip sitting on a piezoelectric material, particles may tunnel through the potential barrier or tunnel through the vacuum between the STM tip and surface at a convenient operating voltage (2meV-2V) under the constant current mode of operation. The vertical tip movement is controlled by a feedback loop and recorded as a location (*x,y*). A schematic of the working principle of STM is shown in Figure 2.12. The tunneling current through an apparent barrier height (ABH) φ and tip-sample distance s is given in:

$$J_T \propto e^{-A\sqrt{\varphi}s} \quad (2.19),$$

where m is the free electron mass, and the ABH is related to the work function, which is the minimum energy required to excite the bulk electron to the vacuum. The current decay constant A is related to the applied voltage through the following relation [85]:

$$A = \sqrt{(4m}/\hbar)/\sqrt{V} \qquad (2.20).$$

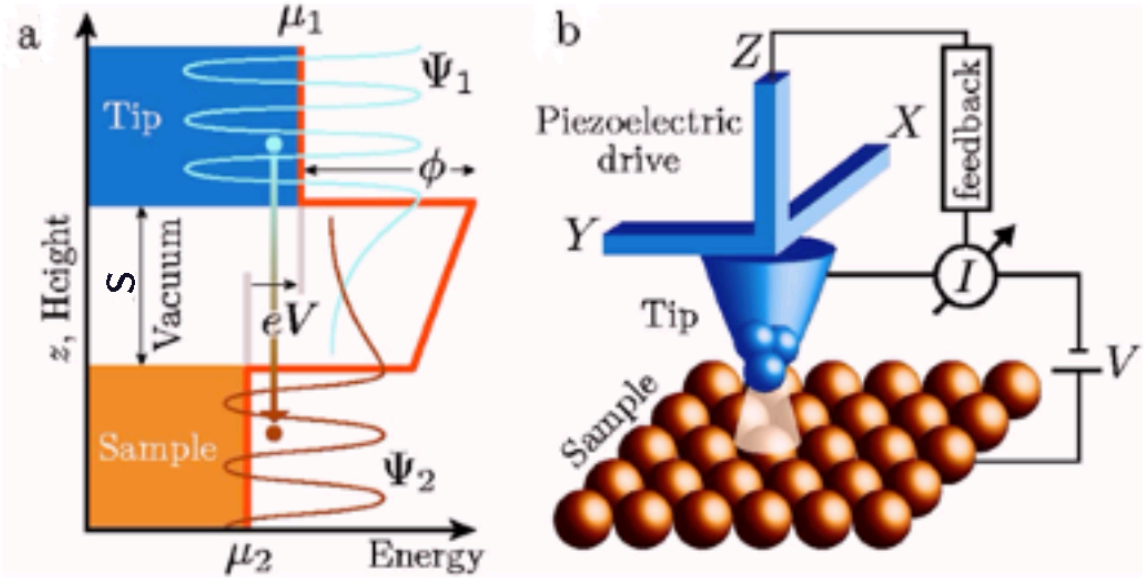

Figure 2.12. Schematic of STM (a) Tunneling process with barrier width s and barrier height ϕ. ψ was the decaying wave function. (b) Schematic view of the tunneling process with a voltage V applied between the tip and surface in a piezoelectric drive. This figure is adapted from Ref. [86].

The constant-current mode is commonly used in probing surface topography. The surface is mapped with a height profile of the tip-sample distance as a surface location function (x, y). The total height is based on the negative exponential relation to the tunneling current J_T and related to LDOS integration over an energy range near the Fermi surface. For real-world measurements, the tip has a finite structure, and a specific electron density of the waves is induced on the sample surfaces by defects. Therefore, we assume that the LDOS integral of this surface is constant and depends on the bias voltage.

The surface topography is bias-dependent. Bias-voltages is carefully selected to obtain a good image contrast. The bias voltage choice is essential when the surface has a relatively flat LDOS, which is not the case for most ruthenate surfaces. Both the atomic height and LDOS difference can influence the height profile greatly. When the surface has a different electronic structure, the STM topography is bias-dependent, and hence the topographic Δz maps the LDOS integration near the Fermi surface. In Figure 2.13, $Sr_3Ru_2O_7$ is an example that shows the surface topography is bias dependent. Figure 2.13a shows the expanded surface cell due to the rotation of the surface octahedron, where the top surface electronic structures at +100 mV and +7 mV for 1×1 and $(\sqrt{2} \times \sqrt{2})\, R45^{\circ}$ are marked as yellow dashed lines accordingly in Figure 2.13b, c, respectively

We are interested in Scanning Tunneling Spectroscopy (STS) AS WHELL. STS collects the dI/dV with tip scanning over the sample surface with a fixed tunneling current. For small tunneling bias voltage, the surface density of states is treated as the local density of states (LDOS). At the Fermi level, tunneling current $I \propto \sum_{E_n=E_F-eV}^{E_F} LDOS(s,E)$, thus the differential tunneling conductance dI/dV provides a valid measurement of the sample LDOS with the following expression:

$$\frac{dI}{dV} \propto \rho_t(0)\rho_s(eV)T(eV,eV,d,\phi), \tag{2.21}$$

Where V is the small bias voltage between tip and sample (otherwise, the tunneling condition breaks down), and $\rho(E)$ is the LDOS near the surface. T is a transfer matrix that depends on the energy of the states involved. The tunneling conductance dI/dV(V) reflects LDOS with structureless tip DOS (i.e., absence of tip). The Lock-in technique generates a sine voltage wave in the collecting process, and the I/V signal is amplified and differentiated to output the dI/dV signal. dI/dV is also bias voltage dependent. To obtain an undistorted STS curve, we then

normalize the dI/dV curve by dividing the I/V curve. We can do STS mapping g(r(*x,y*), V) on large sample surfaces with dI/dV recorded for every pixel. Typically, STS mapping is visualized for surface band dispersion with the evolving wave vector interference.

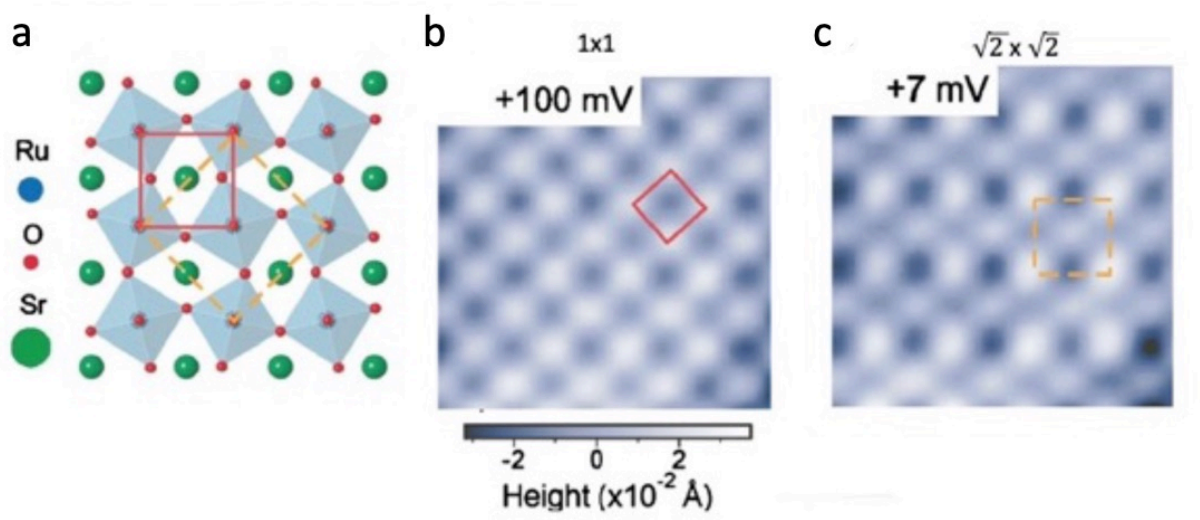

Figure 2.13. $Sr_3Ru_2O_7$ surface unit cell and bias-voltage dependence of STM images illustrating (a) the bulk truncated 1×1 surface unit cell (red solid square) and the surface octahedral rotated unit cell (orange dashed square). (b) The 1×1 unit cell with four bright top Sr sites is marked by red circles at a sample bias voltage of +100 mV. (c) Pure electron reconstruction of the $(\sqrt{2} \times \sqrt{2})\, R45^{\circ}$ surface is observed at a low bias voltage of +7 mV. The corresponding cell is in a yellow dashed square. This figure is adapted from Ref. [87].

Fourier-Transformation (FT) of STM images and conductance is a valuable tool transforming the real-space information containing a long-range wave-like modulation to patterns of spots in reciprocal space like in Figure 2.14, which shows the STM/S for the $Sr_3(Mn_{0.05}Ru_{0.95})_2O_7$ surface. The STM topography in Figure 2.14a shows a square lattice, and Mn dopant is marked with blue dots. Real-space conductance mapping (Figure 2.14b) reveals the electronic distribution. In contrast, its FT-image in Figure 2.14c shows quasiparticle interference (QPI). There are two associated wave vectors: the AFM-related Q_{AFM} and charge ordering-related Q* which are marked in red. Similarly, the FT-STM topographic image visualizes the two-dimensional Fermi surface and contains structural and electronic structure information.

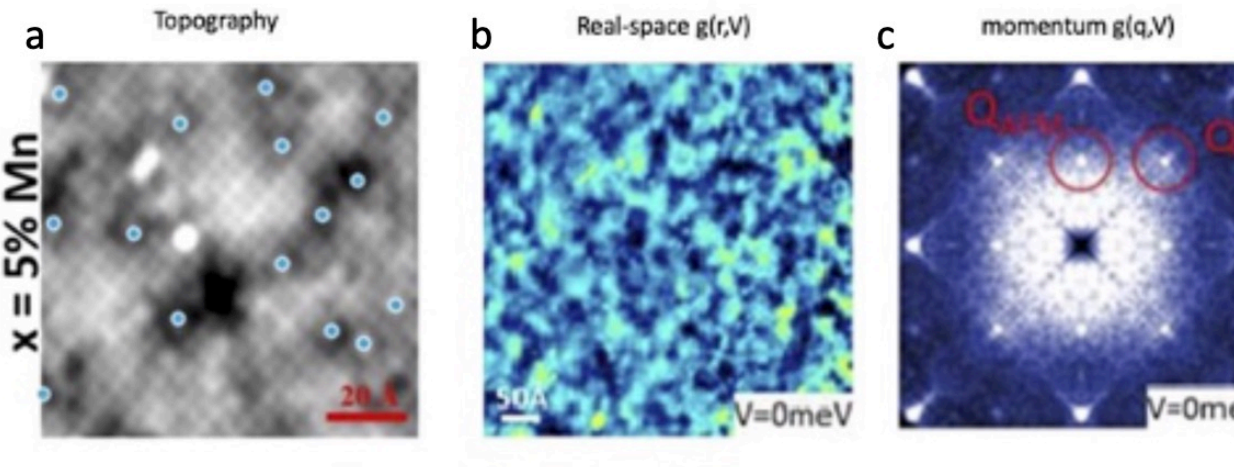

Figure 2.14: Constant-current STM/STS and FT- images on $Sr_3(Ru_{0.95}Mn_{0.05})_2O_7$ at 13 K. (a) STM topography on the (001) surface with V_s = 200mV, I_s = 500pA. A large atomic flat surface is observed with dark regions of defects and Mn dopants marked with blue dots. (b) conductance mapping in real space, where the electron distribution on the sample surface is visualized in different colors. (c) FT image of g(*r,V*) has non-dispersive features where the QP shows two peaks, Q_{AFM} and Q*. All FT have C_{4v} symmetry. This figure adapted from Ref. [88].

Our variable temperature STM/STS was collected with a homemade one with reproducible atomic resolution at CNMS ORNL. The entire STM of CNMS is placed in an isolated acoustic chamber, and in addition mechanical vibrations are isolated by placing the system on an optical table with air legs. Minimum thermal drift is achieved (temperature fluctuation is 0.05 K/h), with an outer shell of the apparatus is filled with liquid nitrogen. The lowest operation temperature is 4 K. This STM also has a 0 to 9 T applied magnetic field capacity. In order to achieve a defect free surface, all sample cleaving is done at 77 K, and the samples are subsequently cooled to 4 K. Various sample-tip bias voltages are tested to get a clear atomically resolved image. To obtain clear atomically resolved surface images of $Sr_3(Ru_{1-x}Mn_x)_2O_7$ samples, we chose a large bias voltage range of -1.5V to 1.5V, where the tunneling current is in the pA range. The tungsten tip is polished on a newly sputtered and annealed Au(111) surface. Lock-in frequency is optimized to

reduce the system noise. The lock-in frequency is chosen in the range of half-integer times electrical base frequency. This instrument was proposed, designed, and constructed by Professor Plummer and Jin when they were at ORNL.

Chapter 3. Bulk Structural Characterization of $Sr_3(Ru_{1-x}Mn_x)_2O_7$

3.1 Bulk Crystal Structures of $Sr_3(Ru_{1-x}Mn_x)_2O_7$ (x = 0, 0.08, 0.16, 0.23 and 1)

The double-layered $Sr_3(Ru_{1-x}Mn_x)_2O_7$ is a complex system and offers a significant advantage for studying structure-property correlations. Its layered structure also provides an opportunity to measure the surface properties in order to probe any hidden bulk phase. The properties of $Sr_3Ru_2O_7$ can be manipulated by doping Mn on the Ru site. $Sr_3(Ru_{1-x}Mn_x)_2O_7$ is an AFM insulator in the region $x < 0.05$. The structural and magnetization measurements show evidence of the local structural change driven magnetic and metal-insulator (MIT) transitions. T_{MIT} pushed to higher temperatures with x . The initial aim of our experimental work was to investigate the structural properties of $Sr_3(Ru_{1-x}Mn_x)_2O_7$ as a function of x at low temperatures. Furthermore, the bulk structural change is accompanied with the emergence of long-range AFM ordering. Correlation between the lattice structure, unit cell volume, and the magnetic transition is studied. The process of characterizing these crystals allow us to understand in more detail the roles of temperature and Mn dopant in the local structural change of $Sr_3(Ru_{1-x}Mn_x)_2O_7$.

We performed Single Crystal X-ray Diffraction measurements at temperatures from 298 K to 28 K through a helium cryo-jet on $Sr_3(Ru_{1-x}Mn_x)_2O_7$ single crystals, which have all been assigned to the same tetragonal space group. The Rietveld method is used to fit diffraction patterns that minimize the difference between the experimental data and a model based on the profile information, crystallographic parameters, and atom positions discussed in Chapter 2. The atomic position and the occupancy equatorial oxygen atoms O3 are left to be a refinement parameter. A unit cell structure of $Sr_3(Ru_{1-x}Mn_x)_2O_7$ is shown in Figure 3.1 with Ru (4*mm*), Mn (4*mm*), Sr_1 (4/*mmm*), Sr_2 (4*mm*), O_1 (4*mm*), O_2 (4/*mmm*), O_3 (4*mm*) [89]. The Ru/Mn ratios in the crystals were obtained using energy dispersive X-ray analysis (EDAX) measurements.

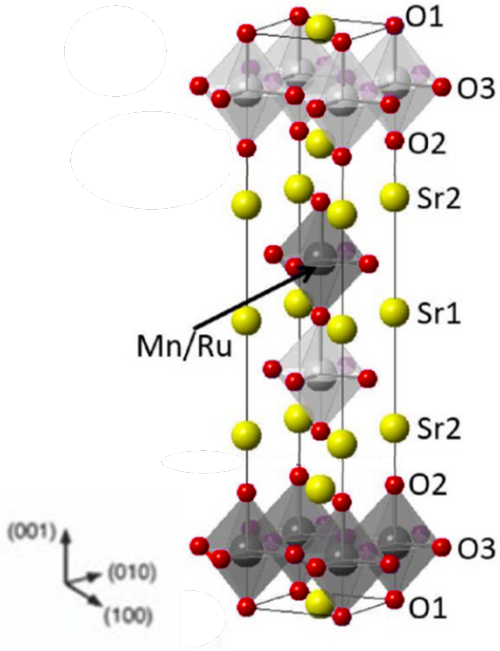

Figure 3.1. The crystal structure of $Sr_3(Ru_{1-x}Mn_x)_2O_7$. The red, yellow, and gray balls represent the O atom, the Sr atom and the (Ru/Mn) atom in the middle of the octahedron, respectively.

The precession image obtained from the collected X-ray diffraction was used to assess the crystal quality. An example of one of the precession images collected on four $Sr_3(Ru_{1-x}Mn_x)_2O_7$ samples ($x = 0$, 0.08, 0.16, and 0.23) with different frames is shown in Figure 3.2a. The iso intensity contour map of electron residual in reciprocal space is included in Figure 3.2b, and the color represents the diffraction peak intensities normalized to the maximum peak intensity. The contour map is symmetric, indicating that the crystals are of a single phase. The precession images are calculated from low-temperature single-crystal X-ray diffraction data at 28 K, and the corresponding image plot is shown in Figure 3.3 for direct comparison. The diffraction spots intensity, image contrast, and resolution were all enhanced at low temperatures. The possibility of twinning in our single crystals was also considered, which is a known problem in tetragonal and orthorhombic systems. By comparing the intensities of equivalent peaks, no clear

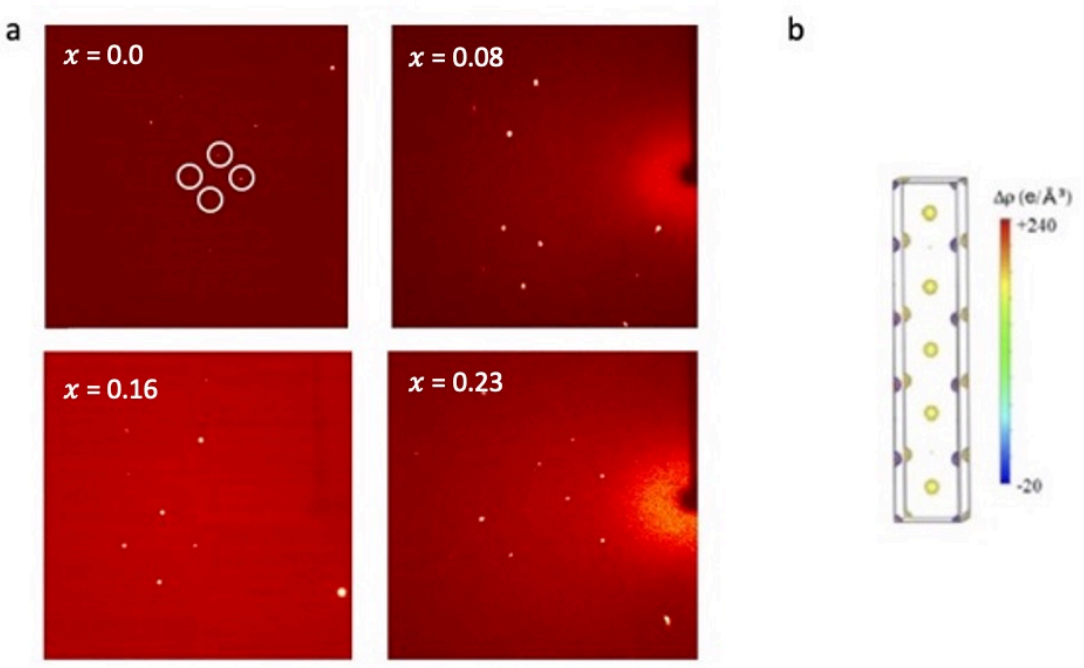

Figure 3.2. (a) Precession images from collected XRD data for four $Sr_3(Ru_{1-x}Mn_x)_2O_7$ (x = 0, 0.08, 0.16 and 0.23) samples at 77 K in the (hk0) plane. The X-ray is directly parallel to the in-plane axis of the I4/*mmm* unit cell marked in the white circle (b) One iso intensity contour map of the $Sr_3(Ru_{0.84}Mn_{0.16})_2O_7$ electron-density residual structure with a resolution of 0.08 $e^-/Å^3$.

sign of twinning was observed from the above precession images. Attempts were made to solve this structure with a tetragonal model, as previously suggested [90]. The details of bulk refinement parameters are given in Table 3.1, where both R_1 and R_2 are reflection-based parameters and computed the difference between real and theoretical models. The quality of the fit to the data is also limited due to nearly 2000 reflections and data collected at different temperatures, and all converges with final R_1 (< 0.02), R_2 (< 0.1), and a final difference map of < 2 $eÅ^{-3}$. The R-factors for this refinement suggest our sample structure can be fitted adequately with the tetragonal structure.

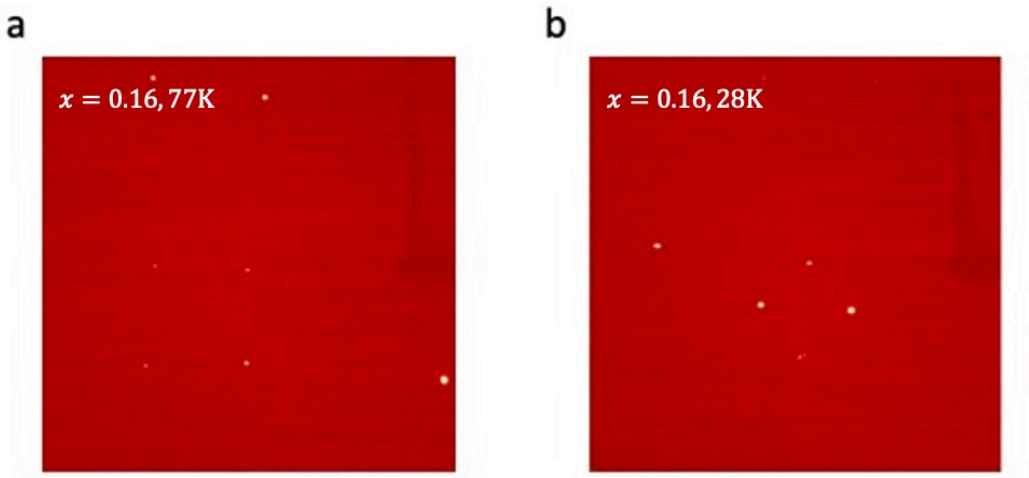

Figure 3.3. Temperature dependence precession images in the reciprocal space from the diffraction data collected at 77 K and 28 K for $Sr_3(Ru_{0.84}Mn_{0.16})_2O_7$.

Refinement of the structure of the $Sr_3(Ru_{1-x}Mn_x)_2O_7$ samples revealed the lattice parameters at 28K for different Mn (x) : $a = b = 3.9031(6)$Å, $c = 20.663$Å for $x = 0.08$. $a = b = 3.9107(6)$Å, $c = 20.613(4)$ Å for $x = 0.16$. For $x = 0.2$, $a = b = 3.9010(6)$Å, $c = 20.385$Å. In this case, the out of the plane lattice parameter c shows a contraction while in-plane lattice constants a and b monotonically increase for $x < x_c$ and then decrease beyond the turning point $x_c = 0.16$. The lattice parameters, fitting details, and temperature dependence of the lattice parameters for the $Sr_3(Ru_{1-x}Mn_x)_2O_7$ ($x = 0.08$, 0.16, and 0.23) samples obtained by structural refinement are given in Tables 3.2 - 3.4, respectively. Selected interatomic distances or the bond lengths are provided in Tables 3.5 – 3.7. The refinement also includes anisotropic thermal parameters, which further improves refinement. As the temperature is reduced, the diffraction peaks appear at positions corresponding to the same I4/*mmm* space group for $x_c = 0.16$. We can see that no structural phase transitions occur upon cooling well below the magnetic transition temperature. The refined structure agrees with the neutron structural studies at ORNL using Lamour rotation where the lattice parameters $a = b$ [44,90]. Starting from the lighter doped $Sr_3(Ru_{0.92}Mn_{0.08})_2O_7$, O atoms split into three Wyckoff positions with 2*b* for O1, 4*e* for O2 and 8*g* for O3. For $x = 0.16$, the O3 Wyckoff

position changes from 8*g* to 16*n* when cooled down from 298 K to 90 K as seen in the $Sr_3Ru_2O_7$ *I*4/*mmm* model [31], then further to 28(2) K, both U_{eq} and O3 Wyckoff position remained unchanged compared to their 298 K values. The refined Wyckoff positions for the partially occupied O3 site is quite different, which may have caused some of the challenges we experienced in refining the positions.

Table 3.1. Single crystal refinement parameters for $Sr_3(Ru_{1-x}Mn_x)_2O_7$ system at 77 K.

Refined Formula	$x = 0.08$	$x = 0.16$	$x = 0.23$
F.W. (g/mol)	569.39	562.01	557.39
Space group	*I*4/mmm ;	*I*4/mmm ;	*I*4/mmm ;
a (Å)	3.9031(6)	3.9107(6)	3.9010(6)
c (Å)	20.663(4)	20.613(4)	20.385(4)
V (Å^3)	314.78(11)	315.25(11)	313.40(11)
Z	2	2	2
Extinction Coefficient	0.0123(10)	0.081(9)	0.065(9)
θ range (º)	3.945 - 34.940	1.976 - 34.878	3.999-35.036
Measured reflections	1747	2174	1913
Independent reflections	246	255	255
Parameters	20	20	26
[b] $R_1[F^2 > 2\sigma(F^2)]$	0.0186	0.0193	0.0270
[c] $wR_2(F^2)$	0.0474	0.0409	0.1118
$\Delta\rho_{\max}(e\text{Å}^{-3})$	0.977	0.972	7.657
$\Delta\rho_{\min}(e\text{Å}^{-3})$	-1.544	-1.091	-3.525

[a] $R_{\text{int}} = [\Sigma \mid F_0^2 - F_c^2(\text{mean}) \mid / (n-p)\,]^{1/2}$
[b] $R_1 = \Sigma \mid \mid F_0 \mid - \mid F_c \mid \mid / \Sigma \mid F_0 \mid$
[c] $wR_2 = [\,\Sigma\,[\,w(\,F_0^2 - F_c^2\,)^2 / \Sigma\,[\,w(\,F_0^2\,)^2\,]\,]^{1/2}$
[d] $S = [\,\Sigma\,[\,w(\,F_0^2 - F_c^2\,)^2 / \Sigma\,(n-p)]^{1/2}$

Table 3.2. Atomic coordinates and equivalent isotropic displacement parameters of $Sr_3(Ru_{0.92}Mn_{0.08})_2O_7$.

Atom	*Wyckoff* position	*x*	*y*	*z*	Occ.[a]	U_{eq} (Å^2)[b]
T = 298(2) K						
Sr1	2*b*	0	0	1/2	1.000	0.0090(4)
Sr2	4*e*	0	0	0.31520 (5)	1.000	0.0083(4)
Mn1	4*e*	0	0	0.09740 (3)	0.091(10)	0.0038(4)
Ru1	4*e*	0	0	0.09740 (1)	0.909 (10)	0.0038(4)
O1	2*a*	0	0	0	1.000	0.0124(19)
O2	4*e*	0	0	0.19500(3)	1.000	0.0112(13)
O3	16*n*	0	1/2	0.09640(2)	0.500	0.013(4)
T = 90(2) K[1]						
Sr1	2*b*	1/2	1/2	0	1.000	0.0053(5)
Sr2	4*e*	1/2	1/2	0.18 (6)	1.000	0.0053(4)
Mn1	4*e*	0	0	0.09746 (4)	0.080(1)	0.0034(5)
Ru1	4*e*	0	0	0.09746 (4)	0.092(1)	0.0034(5)
O1	2*a*	0	0	0	1.000	0.0080(2)
O2	4*e*	0	0	0.19500 (4)	1.000	0.0080(2)
O3	16*n*	1/2	0	0.09600 (2)	1.000	0.0080(2)
T = 28(2) K						
Sr1	2*b*	1/2	1/2	0	1.000	0.0032(2)
Sr2	4*e*	1/2	1/2	0.1871 (2)	1.000	0.0027(2)
Mn1	4*e*	0	0	0.0982 (2)	0.083(1)	0.0020(2)
Ru1	4*e*	0	0	0.0982 (2)	0.092(1)	0.0020(2)
O1	2*a*	0	0	0	1.000	0.0047(9)
O2	4*e*	0	1/2	0.19520 (2)	1.000	0.0061(7)
O3	8*g*	0	1/2	0.09640 (2)	1.000	0.0026(1)

[an] Occupancy of atoms
[b] U_{eq} is defined as one-third of the orthogonalized U^{ij} tensor.

Table 3.3. Atomic coordinates and equivalent isotropic displacement parameters of $Sr_3(Ru_{0.84}Mn_{0.16})_2O_{7.}$

Atom	*Wyckoff* position	*x*	*y*	*z*	Occ.[a]	U_{eq} (Å^2)[b]
T = 298(2) K						
Sr1	2*b*	1/2	1/2	0	1.000	0.0086 (6)
Sr2	4*e*	1/2	1/2	0.18507 (8)	1.000	0.0080 (5)
Mn1	4*e*	0	0	0.09741 (6)	0.165 (13)	0.0040 (6)
Ru1	4*e*	0	0	0.09741 (6)	0.835 (13)	0.0040 (6)
O1	2*a*	0	0	0	1.000	0.012 (3)
O2	4*e*	0	0	0.1960 (5)	1.000	0.011 (2)
O3	8*g*	1/2	1/2	0.0969 (3)	0.500	0.0191 (17)
T = 90(2) K[1]						
Sr1	2*b*	1/2	1/2	0	1.000	0.0059 (6)
Sr2	4*e*	1/2	1/2	0.18508 (8)	1.000	0.0054 (6)
Mn1	4*e*	0	0	0.09726 (6)	0.157 (16)	0.0036 (6)
Ru1	4*e*	0	0	0.09726 (6)	0.843 (16)	0.0036 (6)
O1	2*a*	0	0	0	1.000	0.010 (3)
O2	4*e*	0	0	0.1951 (6)	1.000	0.011 (2)
O3	16*n*	1/2	0	0.0510 (6)	0.5	0.006 (5)
T = 28(2) K						
Sr1	2*b*	1/2	1/2	0	1.000	0.0047 (3)
Sr2	4*e*	1/2	1/2	0.1853 (5)	1.000	0.0040 (3)
Mn1	4*e*	0	0	0.0974 (4)	0.16 (2)	0.0024 (3)
Ru1	4*e*	0	0	0.0974 (4)	0.84 (2)	0.0024 (3)
O1	2*a*	0	0	0	1.000	0.008 (2)
O2	4*e*	0	0	0.19540 (4)	1.000	0.006 (1)
O3	8*g*	0	1/2	0.09670 (3)	1.000	0.021 (2)

[a] Occupancy of atoms
[b] U_{eq} is defined as one-third of the orthogonalized U^{ij} tensor

Table 3.4. Atomic coordinates and equivalent isotropic displacement parameters of $Sr_3(Ru_{0.76}Mn_{0.23})_2O_{7.}$

Atom	*Wyckoff* position	*x*	*y*	*z*	Occ.[a]	U_{eq} (Å^2)[b]
T = 298(2) K						
Sr1	2*b*	0	0	1/2	1.000	0.0090(4)
Sr2	4*e*	0	0	0.31520 (6)	1.000	0.0083(4)
Mn1	4*e*	0	0	0.09740 (2)	0.091(10)	0.0038(4)
Ru1	4*e*	0	0	0.09740 (2)	0.909 (10)	0.0038(4)
O1	2*a*	0	0	0	1.000	0.0124(19)
O2	4*e*	0	0	0.19500 (4)	1.000	0.0112(13)
O3	8*g*	0	1/2	0.09640 (2)	0.500	0.013(4)
T = 90(2) K[1]						
Sr1	2*b*	1/2	1/2	0	1.000	0.0053(5)
Sr2	4*e*	1/2	1/2	0.18607 (6)	1.000	0.0053(4)
Mn1	4*e*	0	0	0.09733 (4)	0.080(1)	0.0034(5)
Ru1	4*e*	0	0	0.09733 (4)	0.092(1)	0.0034(5)
O1	2*a*	0	0	0	1.000	0.0080(2)
O2	4*e*	0	0	0.19500 (4)	1.000	0.0080(2)
O3	8*g*	1/2	0.064(2)	0.09600 (2)	1.000	0.0080(2)
T = 28(2) K						
Sr1	2*b*	1/2	1/2	0	1.000	0.0049 (6)
Sr2	4*e*	1/2	1/2	0.18710 (2)	1.000	0.0078 (7)
Mn1	4*e*	0	0	0.09820 (1)	0.021 (3)	0.0053 (6)
Ru1	4*e*	0	0	0.09820 (1)	0.079 (3)	0.0053 (6)
O1	2*a*	0	0	0	0.088 (9)	0.0050 (6)
O2	4*e*	0	0	0.19560 (10)	0.090 (8)	0.0016 (6)
O3	8*g*	0	1/2	0.09660 (6)	0.085 (5)	0.0013 (4)

[a] Occupancy of atoms
[b] U_{eq} is defined as one-third of the orthogonalized U^{ij} tensor.

Table 3.5. Refined Bond Lengths (Å) and Angle of $Sr_3(Ru_{0.92}Mn_{0.08})_2O_7$.

	298 (2) K	90 (2) K[1]	28 (2) K
Bond Lengths			
Sr1 - O1	2.7507 (14)	2.73792 (14)	2.760 (5)
Sr1 – O3	2.635 (15)	2.613 (6)	2.789 (3)
Sr2 – O2	2.445 (11)	2.7446 (7)	2.767 (6)
Sr2 – O3	2.534 (3)	2.891 (6)	2.685 (3)
Ru1 – O1	2.0195 (11)	2.0263 (10)	2.012 (6)
Ru1 – O2	2.040 (10)	2.046 (9)	2.022 (5)
Ru1 – O3	1.9490 (2)	1.9553 (10)	1.952 (4)
Bond Angles			
O1 - Ru1 – O3	89.39 (19)	89.70 (15)	89.44 (10)
O2 - Ru1 – O3	90.61 (19)	90.30 (15)	90.96 (10)
Rotation			
$(Ru/Mn)O_6$ rotation	6.7(6)	8.1(2)	6.6 (2)

[1] Table generated from reference [91].

of oxygen due to the shift in these positions. Previous work has identified a structural phase transition with the Mn concentration *x,* mainly in the octahedral rotation angle, which is believed to be from a lower orthorhombic symmetry phase to the I4/*mmm* unit cell [90]. This study at 77 K has also revealed a similar evolution of the octahedral rotation which disappeared at all temperatures beyond the critical concentration. This change has also been attributed to the orbital ordering from a recent resonant X-ray diffraction study [92].The distance from outer apical oxygen to the octahedral center or Ru/Mn-O2 bond lengths remains unchanged upon cooling for $x = 0.08$ and 0.16. In contrast, for $x = 0.23$, the inner apical oxygen to the octahedral center Ru/Mn-O1 bond length increases from 1.983(3)Å at 298 K to 2.002(3)Å at 28 K while the Ru/Mn-O2 bond

length (1.987(9)Å at 298 K to 1.990(3)Å at 28K). The Ru/Mn-O3 bond length (from 1.956(3) Å at 298 K to 1.961(4)Å at 28K) experiences little change. The bond angle difference in O1-Ru/Mn-O3 and O2-Ru/Mn-O3 indicates a slight symmetrical buckling.

Table 3.6. Refined Bond Lengths (Å) and Angle (°) of $Sr_3(Ru_{0.84}Mn_{0.16})_2O_7$.

	298 (2) K	90 (2) K[1]	28 (2) K
Bond Lengths			
Sr1 - O1	2.765 (4)	2.7570 (2)	2.765 (5)
Sr1 – O3	2.784 (5)	2.641 (17)	2.792 (5)
Sr2 – O2	2.433 (11)	2.7646 (9)	2.773 (8)
Sr2 – O3	2.661 (5)	2.811 (19)	2.738 (3)
Ru1 – O1	1.9926 (12)	1.9915 (13)	2.007 (10)
Ru1 – O2	2.016 (11)	2.004 (12)	2.020 (9)
Ru1 – O3	1.9554 (11)	1.960 (2)	1.955 (4)
Bond Angles			
O1 - Ru1 – O3	89.7 (2)	89.6 (3)	89.59 (19)
O2 - Ru1 – O3	90.3 (2)	90.4 (3)	90.41 (19)
Rotation			
$(Ru/Mn)O_6$ rotation	0	5.8 (7)	0.55 (0.5)

[1]Table generated from reference [47].

Refinement results of the $Sr_3(Ru_{1-x}Mn_x)_2O_7$ samples from the X-ray diffraction data are plotted in Figure 3.4. The lattice parameter *a* reaches maximum at the critical point x_c. Room temperature structural refinements of the two end compounds of $Sr_3Ru_2O_7$ and $Sr_3Mn_2O_7$ are added for better discrimination of structure change [91,93]. Even though the unit cell volume of $Sr_3Mn_2O_7$ is also significantly reduced, the *c/a* ratio increased to the value near x_c, as seen in Figure 3.4a-d. Figure 3.4e-g shows the refined bond lengths from the octahedral center Ru/Mn to the three

oxygen sites. These bond lengths at 298 K and 28 K are more or less the same with monotonic decreasing trends with *x.* It is also clear that across the bulk magnetic transition temperature, the octahedral distortion at $x = 0.16$ changes more or less steeply at 298 K as shown in Figure 3.4h with the calculated δ_{JT} = [Ru/Mn-O1 + Ru/Mn-O(2)]/2 × Ru-O(3)] parameter. The results we obtained from the single crystal XRD reveal dynamic structural variation with the Mn (x) concentration. For the critical compound x_c, we obtained the magnitude of the octahedral rotation from the O1-Ru/Mn-O3 bond angles of the adjacent octahedra. The rotation angles are close to 0 degrees at 298 K and 28 K compared to 5.8 (7) degrees at 90 (2) K. For the bond lengths, we observed little change throughout the bulk T_M.

Table 3.7 Refined Bond Lengths (Å) and Angle (°) of $Sr_3(Ru_{0.8}Mn_{0.23})_2O_7$

	298 (2) K	90 (2) K	28 (2) K
Bond Lengths			
Sr1 - O1	2.765 (3)	2.761 (7)	2.773 (5)
Sr1 – O3	2.771 (7)	2.762 (3)	2.779 (9)
Sr2 – O2	2.773 (3)	2.444 (8)	2.778 (14)
Sr2 – O3	2.658 (6)	2.664 (3)	2.693 (9)
Ru1 – O1	1.983 (3)	1.985 (7)	2.002 (3)
Ru1 – O2	1.987 (9)	1.987 (8)	1.990 (3)
Ru1 – O3	1.956 (3)	1.953 (5)	1.950 (4)
Bond Angles			
O1 - Ru1 – O3	89.4 (3)	89.10 (15)	89.10 (4)
O2 - Ru1 – O3	90.6 (3)	90.90 (15)	90.95 (4)
Rotation			
$(Ru/Mn)O_6$ rotation	0	0	0

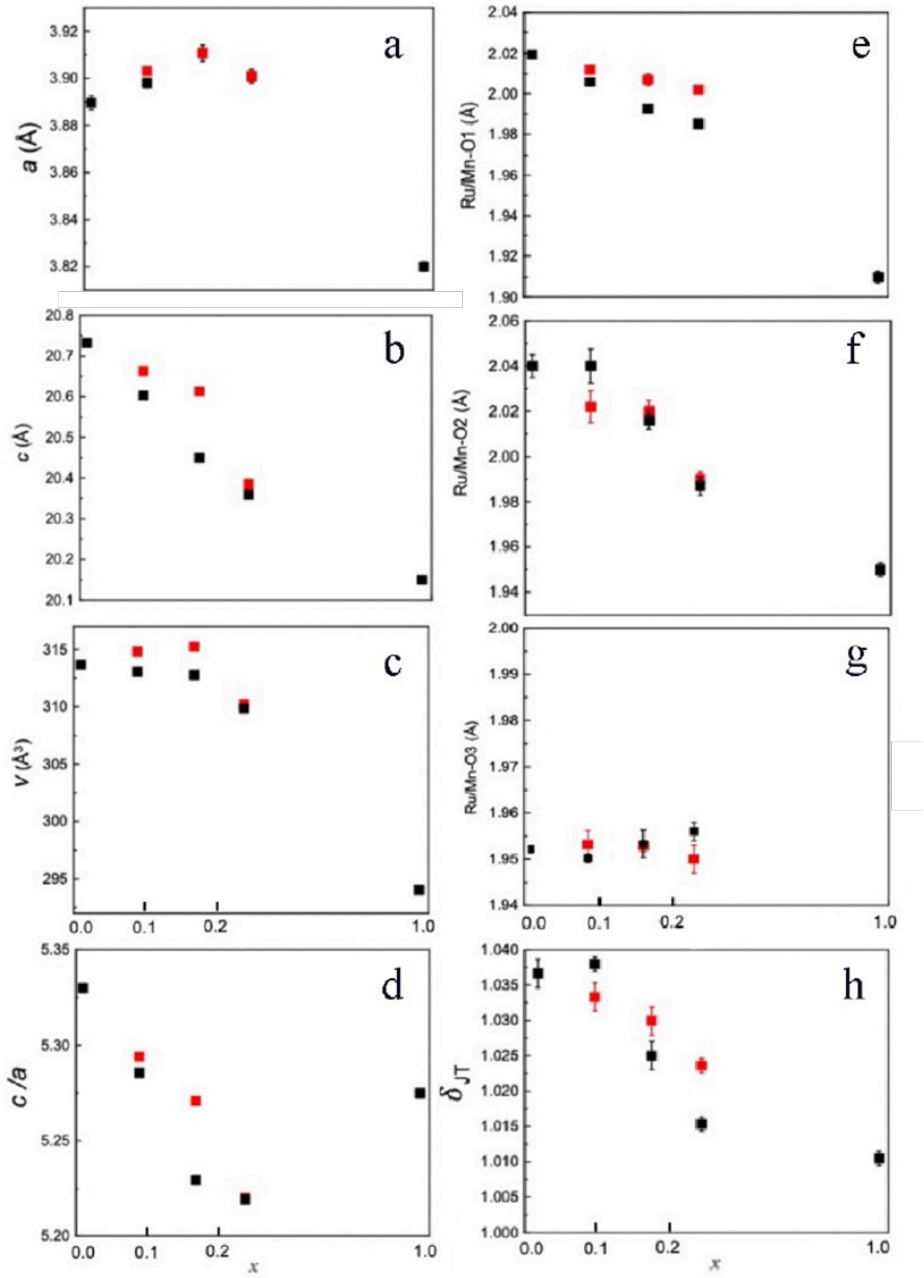

Figure 3.4. Mn concentration dependence of lattice parameters, volume, *c/a*, bonding lengths, and Jahn-Teller distortion (δ_{JT}) at 298 K (black squares) and 28 K (red squares). (a) – (d) Tetragonal lattice parameter *a*, *c*, V, and the ratio *c/a* of $Sr_3(Ru_{1-x}Mn_x)_2O_7$ respectively. (e) – (g) Refined bond lengths of Ru/Mn- O(1), Ru/Mn – O(2), and Ru/Mn – O3 respectively. (h) The calculated δ_{JT} room temperature refinement data of the two end compounds, $Sr_3Ru_2O_7$ and $Sr_3Mn_2O_7$, are added for comparison [91,93].

3.2 Comparison with Neutron Scattering Experiment

Another option for obtaining crystalline structural information is neutron scattering. Since interaction between neutrons and nuclei is independent of the number of electrons, the diffraction signal of neutrons from one element has the same order of magnitude as that of the other elements. In the X-ray diffraction measurements, the scattering of X-ray by atoms involves interaction with electrons. Thus, X-ray scattering factor is related to the number of electrons in atoms. Due to the spatial delocalization of electron density, the X-ray scattering factor decreases with the increase of the scattering vector. The scattering vector is defined as $Q = 4\pi sin\theta/\lambda$, where θ and λ are the diffraction angle and the wavelength. Thus, the contribution from the light elements (such as H, O) can be challenging to distinguish in the presence of heavier elements. Moreover, since the different oxidation states of a given element have different numbers of electrons, the scattering contribution of the redox-active transition metal will also vary according to the charge state. However, neutron scattering in neutron diffraction (ND) measurement involves interaction with the nucleus, and the neutron scattering length varies irregularly with atomic number and isotope, which is not related to Q. The differential scattering cross-section is also proportional to the square of the scattering lengths:

$$\frac{d_\sigma^2}{d\Omega_f dE_f} = N\frac{k_f}{k_i}\frac{\sigma}{4\pi}S(Q,\omega) \qquad (3.1).$$

This equation suggests that in a specific energy window dE, the incident neutron is scattered with a solid angle $d\Omega$. With the presence of atomic isotopes, it generates a spatial fluctuation in its scattering length. It contributes an incoherent factor to the overall scattering cross-section where neutrons can distinguish the neighboring elements (close Z) and pick up the atomic isotopes. The rest is the significant coherent contribution from single atomic species that interferes with the scattered waves. Therefore, the XRD refinement results highly depend on the X-ray scattering

factor of atoms in the structure model and the Q range. Generally, the structural model uses a factor of free neutral or ion. However, the scattering factor of free atoms will significantly deviate from the actual scattering of atoms in the lattice since charge transfer could occur between atoms, so the actual charge density on the atoms will deviate from their formal charges [25,94].

The variability of the neutron scattering length can help distinguish between low atomic numbers and similar atomic number species. A lower symmetry is usually adopted in modeling the neutron scattering data as superlattice, weaker peaks, and lighter-mass peaks [25]. The Q independence of the scattering length makes ND more suitable than XRD for determining atomic displacement parameters. This section takes Ba_2CoO_4 and $Sr_3(Ru_{1-x}Mn_x)_2O_7$ as examples to illustrate the sensitivity and limit of X-ray and neutron powder diffraction when solving the bulk structures of transition metal oxides.

The actual scattering coefficients of atoms are estimated using a linear combination of the scattering coefficients. Considering that the Mn scattering coefficient in the actual structure is smaller than O and Sr, the coherent scattering lengths b_j are -3.73 fm for Mn, 5.803 fm for O, 7.03 fm for Ru, and 7.02 fm for Sr [95]. The change of the scattering coefficient Mn has little effect on the refining effect, thus it is assumed that the scattering coefficient for Mn is constant. In terms of X-ray scattering, the concept of atomic scattering factor f_j is similar to that of b_j, but f_j is proportional to the Z number [96]. The peak positions and amplitudes contain the structural information, where the peak intensity is a function of *hkl* data and related to the sample angle θ, the unit cell volume V, and the beam of wavelength λ with the following equation:

$$I = \frac{A\lambda^3 |F_S(hkl)|^2}{\mathrm{V}^2 \sin 2\theta} \qquad (3.2).$$

This difference is more pronounced when it comes to the energy-dispersive measurements, where the difference between the two techniques is more notable. Neutrons have a reasonably large wavelength, resulting in anisotropic neutron scattering amplitude as the scatter angle increased. In comparison, X-ray scattering has a lower peak amplitude with $\frac{\sin\theta}{\lambda}$ due to the interference effects for X-ray scattering by each atom [97]. Thus, the resolution for XRD is worse.

Once we have the diffraction data and all the diffraction peaks are identified with known phases, the overall peak profiles are fitted with a full-pattern Rietveld refinement [63]. The refinement yields different values depending on the constrained structural parameters, resulting in false results if the constrained parameters are not fully characterized in another method. For example, the nominal stoichiometric ratio may deviate from the actual stoichiometric ratio, and compositional heterogeneity may result in a stoichiometric distribution of individual crystallites. To solve the structure for doped transition metal oxides $Sr_3(Ru_{1-x}Mn_x)_2O_7$, the refinement cannot converge with lower *Pban* and *Bbcb* orthorhombic space group models. Diffraction aberration due to absorption also occurs in both ND and XRD measurements, but our XRD refinement of the absorption coefficient produced a smaller value (< 0.1), indicating that the absorption here has little effect on the result.

The structural refinement results of Ba_2CoO_4 show the same situation. Even though the previous neutron and X-ray diffraction measurements adopted the same monoclinic space group $P2_1/n$ model [98,99], as shown in Table 3.8, X-ray diffraction analysis yields a 1.675 $Å^3$ larger unit cell volume at room temperature and larger refined lattice constants *a, b*, and *c* compared to the neutron measurement. Such discrepant findings are due to the X-ray scattering factors of Ba, Co, and O, and its low penetration power as a function of the increased atomic number affects the collected peak intensities causing a less accurate refinement result from the X-ray measurement.

We now return to the comparison of the refined lattice parameters for $Sr_3(Ru_{1-x}Mn_x)_2O_7$. In Figure 3. 5 XRD and neutron diffraction (ND) results of lattice parameters at 298 K and 23 K are shown. Temperature makes little impact on the refinement results of the lattice parameter and unit cell volumes. The lattice parameters determined from our single-crystal X-ray diffraction marked in blue agree well with previous results marked in red at 298K [89]. Figure 3.5a shows that the in-plane lattice parameter determined from neutron diffraction (ND) is notably smaller. This difference is particularly evident (~ 0.036 Å) at $x_c = 0.16$, where the in-plane lattice parameter *a* at 298 K and 23 K from neutron measurements are marked in yellow and black respectively. The *a* and *c* lattice parameters are reduced with Mn doping from the ND measurement in Figure 3.5a and b. The findings measured with the single-crystal XRD where *a* first increases and reaches a maximum at $x_c \sim 0.16$ and then decrease with *x* is shown in Figure 3.5a and b. The calculated unit cell volume is reduced with increasing Mn *x* in both measurements in Figure 3.5c.

Table 3.8. : Difference in the lattice constants *a*, *b*, and *c* of Ba_2CoO_4 using X-ray and neutron scattering.

Lattice Constants	Neutron Diffraction 5 K[1]	Neutron Diffraction ext. to RT	X-ray RT[2]	Difference[2]
a(Å)	5.884	5.905	5.9176	0.0126
b(Å)	7.541	7.614	7.6192	0.0052
c(Å)	10.343	10.371	10.379	0.008
Unit Cell Volume(Å^3)	458.93	466.29	467.96	1.675
Angle *a and b* (°)	90.524		91.734	1.210

[12] Table generated from reference [98,99].

Overall, the Rietveld refining of X-ray and neutron diffraction measurements can obtain the precise structural information for $Sr_3(Ru_{1-x}Mn_x)_2O_7$. While the setup for neutron measurements is more advanced and complicated than the in-house X-ray measurements, neutron diffraction is an excellent method for the structure determination of light atom positions with few electrons. For the Rietveld refinement of XRD data, the linear combination of the X-ray scattering factors for atoms results in changes in the refined structural parameter values. Comparing the refinement results from XRD, ND suggests that although there is a substantial difference in absolute value; however, both techniques can capture the trend of structural parameter evolution with changes in temperature and doping level x. More advanced electron density models are needed for XRD to obtain comparable refined bond lengths to the neutron diffraction [100,101]. We should be aware of the limitations and sensitivity of the X-ray diffraction method. Simultaneously using both techniques could result in the best structural model for $Sr_3(Ru_{1-x}Mn_x)_2O_7$ characterization.

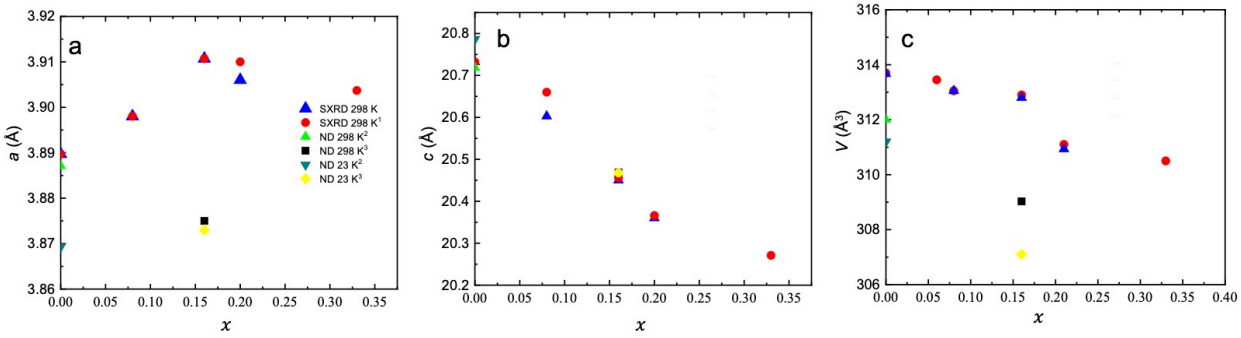

Figure 3.5. The Mn concentration dependence of (a-b) lattice parameters and (c) calculated volume from X-ray and neutron diffractions (ND) at 298 K and 23 K. The SXRD data from Ref. [90] and ND data from Refs. [31] [44] is added for comparison.

Chapter 4. Surface Structural Analysis and Lattice Dynamics of $Sr_3(Ru_{1-x}Mn_x)_2O_7$

In this Chapter, surface studies reveal how breaking the bulk translational symmetry changes the surface structure and lattice dynamics of $Sr_3(Ru_{1-x}Mn_x)_2O_7$. Early-stage surface structure studies showed that the LEED patterns of $Sr_3Ru_2O_7$ have broken glide line symmetry at both room temperature and low temperatures, confirming the presence of lattice tilt distortion on the surface [11]. This broken glideline reduces the symmetry of the LEED pattern to a lower C_{2v} than that of C_{4v} from a rotational-only surface. Detailed calculations show that creating a surface yields an enhanced ~10.5° rotation of the surface RuO_6 and a ~2.6° octahedral tilt [11]. The tilt of surface RuO_6 octahedra drives the surface metallicity of $Sr_3Ru_2O_7$ to be less than that of the bulk, while the disappearance of the tilt promotes the surface metallicity of $Sr_3(Ru_{0.84}Mn_{0.16})_2O_7$. The above examples show that the surface broken symmetry disturbs the balance between structural, electronic, and magnetic degrees of freedom, which leads to the emergence of novel properties. The need to further investigate the changes in the surface structure is obvious: LEED I-V analysis of the detailed surface structure of $Sr_3(Ru_{1-x}Mn_x)_2O_7$ at low temperatures (below bulk T_M) and varying x is necessary to understand the intricate coupling observed in the bulk phases. And the , the new surface phases to establish their unusual structure-property relations in the system.

In this study, we use LEED to probe the symmetry of the surface structure and LEED I-V calculations to quantify the surface octahedral rotation and tilt of $Sr_3(Ru_{1-x}Mn_x)_2O_7$. Highly surface-sensitive HREELS were then used to explore the electronic and lattice dynamics at the crystal surface, by measuring the surface electron-phonon coupling as a function of Mn doping in the temperature range of 77 K - 20 K. The combined results of these surface-sensitive tools confirm

that there are differences in the surface and bulk structures of $Sr_3(Ru_{1-x}Mn_x)_2O_7$ that affect its metallicity.

4.1 LEED I-V Analysis of $Sr_3(Ru_{1-x}Mn_x)_2O_7$ (x = 0, 0.08, 0.16, 0.23, and 1)

4.1.1 LEED Measurements of $Sr_3(Ru_{1-x}Mn_x)_2O_7$ (x = 0, 0.08, 0.16, 0.23 and 1)

The RuO_6 octahedra in $Sr_3(Ru_{1-x}Mn_x)_2O_7$ bulk have an intrinsic rotation around the *c*-axis. For freshly cleaved $Sr_3(Ru_{1-x}Mn_x)_2O_7$ (001) surfaces, octahedra with opposite chirality on the surface result in the same bulk truncated structure. The evolution of the $Sr_3(Ru_{1-x}Mn_x)_2O_7$ surface structure with x and the corresponding LEED patterns are illustrated in Figure 4.1. Figure 4.1a demonstrates surface $(Ru/Mn)O_6$ octahedral rotation with the black box connecting four surface octahedra with the same rotation direction while the middle octahedron has an opposite rotation. Thus, the surface has the same orthorhombic structure as the bulk and the surface lattice constant is equal to $\sqrt{2}$ multiplied by the lattice constant obtained by refining the tetragonal lattice structure used in Chapter 3 ($a_{surface} = a_{tet} \times \sqrt{2}$). Figure 4.1b is the side view of bilayered octahedra, where it tilts along the octahedral edge direction in upward and downward directions as marked with the arrow. The vertical position of the top oxygen atom is lowered and the glide plane parallel to the tilt direction is broken. For surface $(Ru/Mn)O_6$ octahedral rotation only, the corresponding LEED pattern has two perpendicular glide lines as shown in Figure 4.1c (labeled with two perpendicular dashed lines). To conveniently label the LEED diffraction spots, we use a *tet*-(1 × 1) unit cell where the integer points (0, 1) and (1, 0) are marked. The surface and *tet* -(1 × 1) unit cells are marked with black and orange squares, respectively. Figure 4.1d shows the reappearance of the fractional (±3/2, ±3/2) spots along one glide line parallel to the surface $(Ru/Mn)O_6$ octahedral tilt direction. Hence, the fractional spots in the LEED pattern (with respect to *tet*-(1 × 1)) are tilt sensitive. In order to improve the accuracy of our LEED I-V calculation, we choose as many spots

as possible. With surface octahedral tilt, the symmetry of the planar group is reduced to that of the *pg* planar group. So, in Figure 4.1e-f the temperature dependence of the LEED patterns for $Sr_3(Ru_{0.77}Mn_{0.23})_2O_7$ (001) and $Sr_3(Ru_{0.92}Mn_{0.08})_2O_7$ (001) at 77 K with 188eV beam voltage, the missing fractional diffraction spot reappears along the glide line and is circled in green for $Sr_3(Ru_{0.92}Mn_{0.08})_2O_7$ (001) surface.

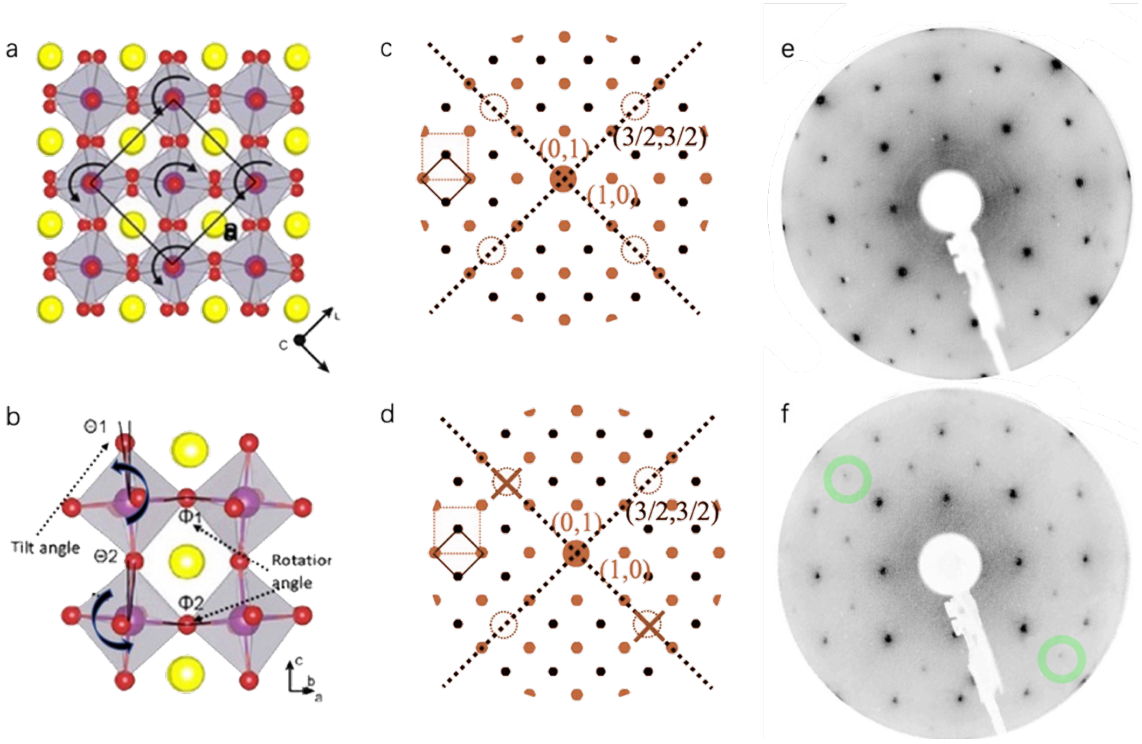

Figure 4.1. Evolution of $Sr_3(Ru_{1-x}Mn_x)_2O_7$ (001) surfaces structures and corresponding LEED images. (a) Surface octahedral rotation along *c*-axis with different chirality. (b) Illustration of the surface octahedral tilt up and down along the edge direction as marked with black arrows. The angles are labeled with θ_1 and θ_2. (c) LEED diffraction pattern labeling based on a *tet*-(1 × 1) unit cell, where the two mutually perpendicular smooth lines are marked with dashed lines. (d) For the tilt of the surface octahedron, the fractional spots (±3/2, ±3/2) along one of the glide lines reappear and break the glide line in this direction. (e-f) are the corresponding LEED patterns for $Sr_3(Ru_{0.77}Mn_{0.23})_2O_7$ (001) and $Sr_3(Ru_{0.92}Mn_{0.08})_2O_7$ (001) surfaces at 77 K with 188eV beam voltage. The green circles mark the reappearance of the fractional point in the middle of the two integer points (-1, 2) and (-2, 1).

For the LEED I-V analysis, we collected the intensities of the diffraction spots spaced along two glide lines, such as (3/2, 3/2), (5/2, 5/2), which are more sensitive to rotation and tilt. Prior to the analysis, the LEED I-V data were smoothed using the Savitzky-Golay method and a third-order polynomial. Each I-V curve is the sum of up to four equivalence points. For example, the integer spot (1, 3) is obtained by averaging the symmetrized points (1, 3), (1, -3), (-3,-1) and (3,-1). Surface atoms are also allowed to relax while maintaining the observed lattice symmetry and serving as

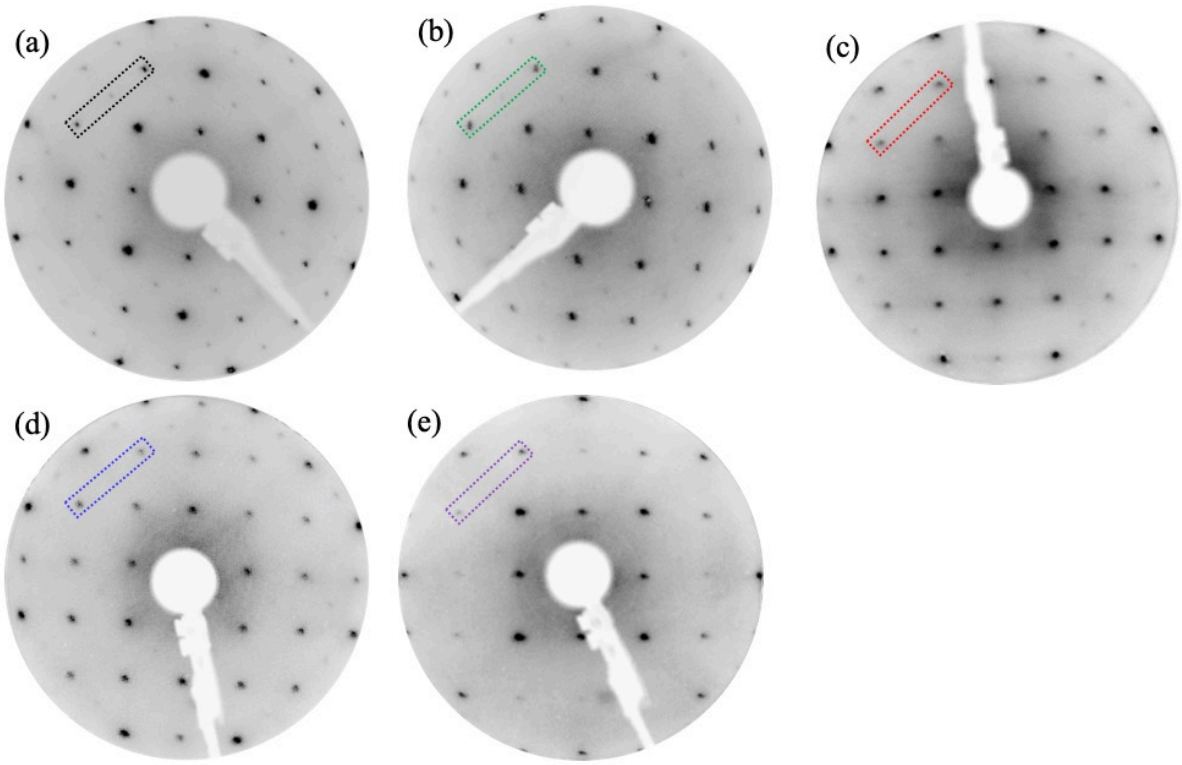

Figure 4.2. LEED diffraction patterns on the surface of freshly cleaved $Sr_3(Ru_{1-x}Mn_x)_2O_7$ (001) collected at 220 eV beam energy vary with x at 77 K. (a-e) x = 0, 0.08, 0.16, 0.2 and 1. The intensities were scanned perpendicular to a glideline in the direction marked inside the colored dashed rectangular box. The intensities of the integer (-2, 1), (-1, 2) and (-3/2, 3/2) diffraction spots were normalized.

the main constraint for atomic relaxation. Figure 4.2 shows the x dependence LEED patterns for the cleaved $Sr_3(Ru_{1-x}Mn_x)_2O_7$ (x = 0, 0.08, 0.16, 0.23, and 1) (001) surface at a fixed beam energy

of 220 eV. To verify whether the $x = 0.08$ surface has an octahedral tilt, we compared its LEED pattern (Figure 4.2b) with the observed C_{2v} lattice symmetry of $Sr_3Ru_2O_7$. Along differently colored dashed rectangles in the LEED image, if the diffraction spot (-3/2, 3/2) appears between the (-1, 2) and (-2, 1), it indicates a broken glide line along this direction. The LEED images were rotated for a better view. From the line profile of the diffraction spots intensities is plotted in Figure 4.3, we found that after normalizing the integer diffraction spots to the highest peak intensity, the presence of (-3/2, 3/2) spot on the freshly cleaved (001) surface in any of our cooling and heating cycles for $x = 0$, 0.08 samples, at any applied beam voltage, which demonstrates that the surface

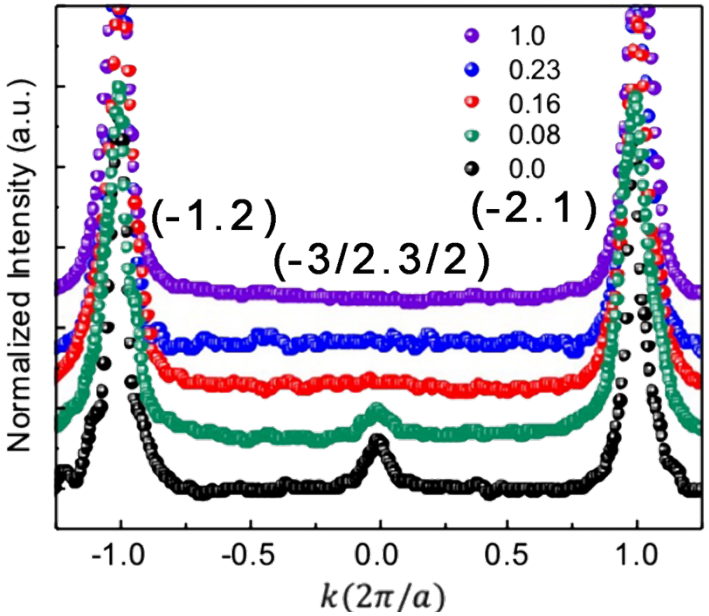

Figure 4.3. : Line scan of the LEED diffraction pattern of $Sr_3(Ru_{1-x}Mn_x)_2O_7$ (001) at 77 K. The surface C_{4v} and C_{2v} lattice symmetry is assigned according to the appearance of the intermediate (-3/2, 3/2) spot and its intensity. The intensity of the (-3/2, 3/2) spot drops to zero due to the absence of surface tilt.

symmetry is reduced to C_{2v} due to the presence of a surface octahedral tilt. Also, we observe that the decrease in the (0, 3) peak at $x = 0.08$ represents a decrease in the magnitude of its surface octahedral tilt compared to $x = 0$. For $x \geq x_c$, the disappearance of the (-3/2, 3/2) spot on the surface for $x = 0.16$, 0.23, and 1.0 shown in Figures 4.2c-e, indicates that the surface octahedra are not

tilted and that the lattice structure shows C_{4v} symmetry. Figure 4.4 a-b shows the LEED patterns obtained for the same x_c surface at 77 K and up to 25 K which is used to study the response of the

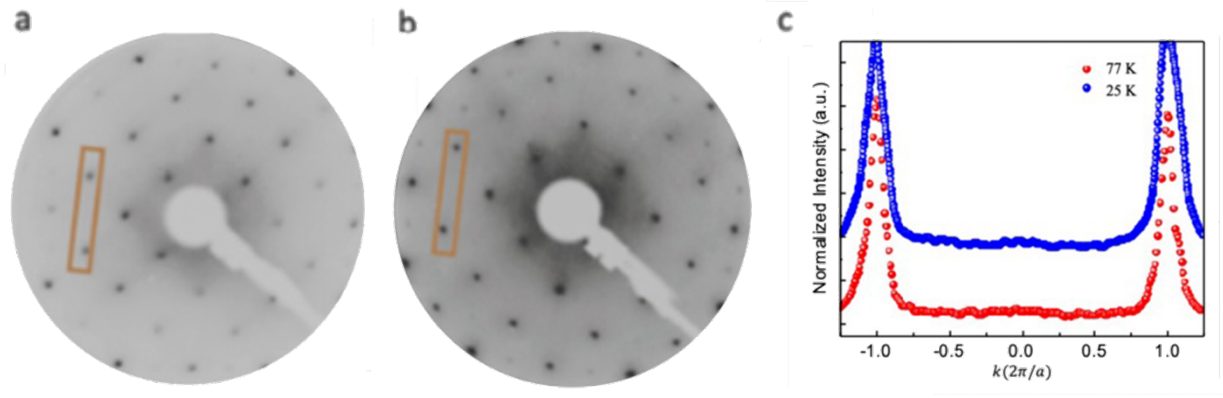

Figure 4.4. LEED diffraction pattern of $Sr_3(Ru_{0.84}Mn_{0.16})_2O_7$ (001) surface at (a) 77K, 220eV beam energy (b) 25K, 210eV beam energy. (c) Line profile of the diffraction spots along the orange box. The disappearance of the (0, 3) spot indicates that the octahedral surface is not tilted at both temperatures.

surface lattice structure to the bulk AFM phase. In Figure 4.3.c, we also did a line intensity profile for the tilt-sensitive (-3/2, 3/2) spot along the direction of the dashed orange rectangular box marked in each LEED pattern and found that the x_c surface has a C_{4v} symmetry at both temperatures. We also observed tilt domains from this experiment. Figure 4.5 shows three LEED pattern images taken at 77 K from $Sr_3(Ru_{0.92}Mn_{0.08})_2O_7$ surface. The three pictures show that multiple terraces and the tilt domains co-exist on the surfaces for sample moving laterally to different positions in a direction perpendicular to the incident electron beam. Figure 4.5a. shows a clear multiple tilt domain on the cleaved sample surface, where both glide lines have been destroyed with factional spots as marked with the green circle resulting in higher *pm* plane group symmetry. The sample is then panned by 0.5 mm, as shown in Figure 4.5b. We observe a single tilted domain with only one glide line with the red circles marking extinct (3/2, 3/2) spot. When the sample is further moved to another position, the LEED pattern has a single tilted domain as shown in Fig. 4.5c, but the glide lines appear to be rotated by 90° from the original direction, and the *pg* symmetry is restored.

Since the diameter of the LEED incident electron beam is about 1 mm and the lateral translation of the sample between images a and c is 2 mm, the tilted domains of the sample surface have different tilt directions with a size in the range of several square millimeters.

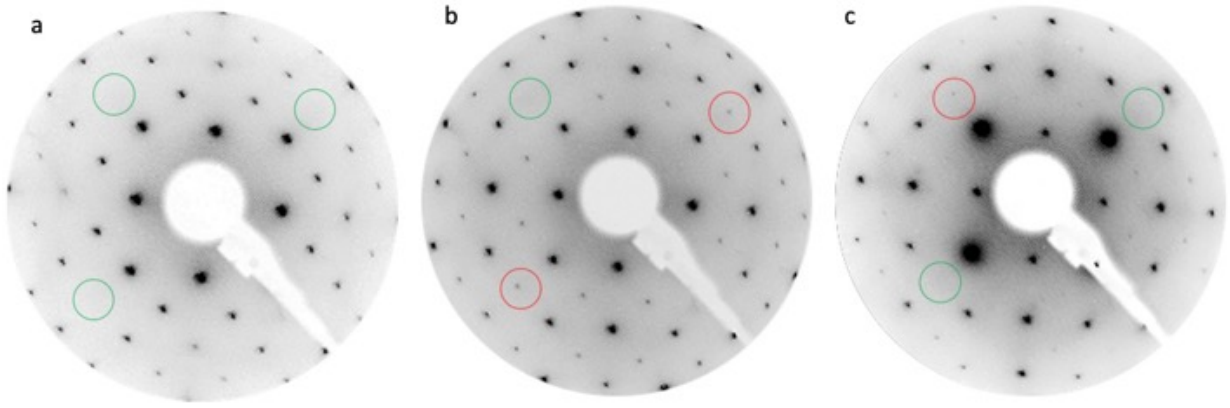

Figure 4.5. LEED patterns with the tilt domains for $Sr_3(Ru_{0.92}Mn_{0.08})_2O_7$ at 77 K. The tilt-sensitive spots are marked by green circles. The appearance of tilt-sensitive the spots along the glides is drawn with the red circles (a) at 190 eV with no glide planes, (b) after the position change at 216 eV which shows one glide line symmetry along the red circles (c) the tilt axis shows a 90-degree rotation with a further lateral 1mm movement. The LEED pattern has one glide line symmetry at 250 eV.

Subsequent cleavage of individual samples also showed the observed rotation of the tilt axis, and the cleavage of the sample was favorable at the boundary of the tilt domain. Since the LEED pattern for $x = 0.08$ shows a similar tilt to the surface for $x = 0$, a reference structure was generated using the $x = 0$ data obtained in the previous section for LEED IV calculation. For $x \geq x_c$, due to the similarity of the overall structure at different x and temperatures, we used the bulk structure for x_c at 77 K as the reference structure. Experimental I-V spectra of a set of unequal beams over a similar energy range (60-600 eV) were collected for different samples. These unequal beams were then averaged to reduce the error that arises when implementing data collection.

4.1.2 Surface Model Construction and Structural Refinemnt of $Sr_3(Ru_{1-x}Mn_x)_2O_7$ (x = 0, 0.08, 0.16, 0.23 and 1)

We used a customized SATLEED package for a detailed analysis of the surface structure for $Sr_3(Ru_{1-x}Mn_x)_2O_7$ (x = 0, 0.08, 0.16, 0.23 and 1) samples [102]. The experimental IV curves were collected in 1 eV increments in the energy range, where we could obtain clear LEED images while satisfying the normal incidence condition. Figure 4.6 shows how the normal incidence condition can be confirmed by comparing the intensities of the symmetric diffraction points. Figure 4.6a. shows the $Sr_3Ru_2O_7$ surface at 77 K, where the symmetrical (3, 0), (2, 2) beams are marked with yellow and blue circles, respectively. To meet the experimental conditions, the difference between each beam must be kept within $R_p < 0.3$. Figure 4.6b and c shows the comparison of the calculated R_p differences between the selected (3, 0), (-3, 0) and (2, 2), (-2, 2) individual beams. Ten different sets of I-V curves were collected and analyzed for different samples at different temperatures. Ten symmetrical equivalent integer and fractional beams were recorded and averaged to generate the IV data for experiment, and all beams were normalized to the sample current I_0. The collected beams were smoothed with a weighted 5-point adjacency averaging method in order to obtain a low statistical R_p error: $\mathrm{var}(R_p) = R_p^{\min}\sqrt{8Voi/\Delta E}$ over the total energy range of 2754 eV to 4134 eV [76].

The initial reference surface model of $Sr_3(Ru_{1-x}Mn_x)_2O_7$ surface was split into two parts as discussed in the previous section, with x_c as the turning point. The surface modeling process is shown in Figure 4.7. Figure 4.7a shows the modeling of the surface slab containing five composite layers sitting on top of the bulk structure, with the cleaved surface at the top, and above the surface is the vacuum. The interlayer distances between each surface layer are optimized to allow the phase shift to converge. The surface unit cell with octahedral rotation is shown in Figure 4.7b, where two

different O1 atoms are labeled as O1_1 and O1_2. The bulk data show that (Ru/Mn)O_6 octahedra can be considered as rigid objects. Without breaking the surface symmetry observed in the LEED

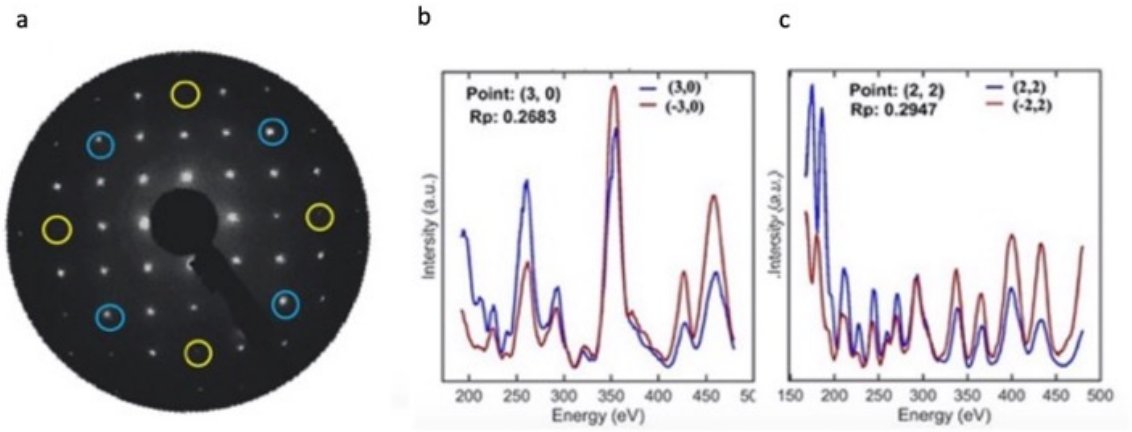

Figure 4.6. Example of the LEED I-V collections for $Sr_3Ru_2O_7$ (290eV) at 300K. (a) Symmetrized (3,0) and (2,2) beams were marked with yellow and blue circles. (b-c) Experimental comparison between two symmetrized points (3,0), (-3,0) and (2,2), (-2,-2) respectively. Individual R_p listed for checking the normal incidence condition.

pattern, the *pg* plane set allows distortions to be made to the surface octahedra. The symmetry generator allows us to determine the fitting parameters for the 24 atoms of the surface layer, and several atoms can be combined. For example, the Ru/Mn atom in the center of the octahedron can be moved vertically on the O1 substrate without breaking the observed pattern. Furthermore, the length of the Ru/Mn-O2 bond from the center of the octahedron to the top and bottom oxygen atoms can have different values. We tested different combinations of fitting parameters and found that the final R_p did not change for different surface rotations.Therefore, we always assume the same direction of rotation for the surface octahedron. Vertical displacements of the surface atoms significantly improve the final results (R_p decreases by 0.03). Furthermore, allowing the tilt of O1 to be different from the tilt of O2 does not improve the final results, and therefore two tilt angles with $\theta 1 = \theta 2$ are used as optimization parameters. The fitting parameters used in this optimization

method define the tilt and rotation of the surface octahedron. Figure 4.8 illustrates the fitting parameters for individual atoms of the surface bilayer octahedron. Due to rotation, the

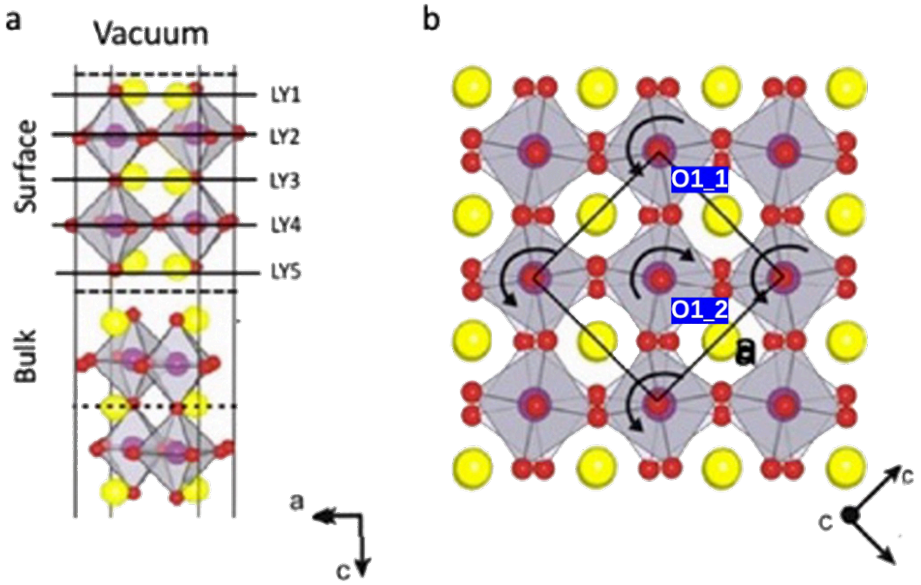

Figure 4.7. Reference surface structure for the initial LEED I-V calculations (a) model with five surface layers above the bulk layer, with interlayer distances optimized for convergent phase shifts. (a) Top view of the surface bilayer octahedron. There are two different O1 atoms on top: O1_1 and O1_2.

lateral shift of the surface oxygen atoms in the *a*- and *b*-axis coordinates is estimated as $\Delta x_1 = \tan(\phi_1)/4$. Similarly, $\Delta x_2 = \tan(\phi_2)/4$ is for the lateral shift of the oxygen in the second half bilayer octahedron. For $x < x_c$, the tilt of the octahedron shifts the oxygen atoms, O1 and O3, vertically along the *c*-axis by $\Delta h = \tan(\theta)/10$. The Δt_x and Δt_y estimates (*x, y*) coordinate shifts of O1 and O3 where $\Delta t_x = \Delta h \times 3.8$, $\Delta t_{y_1} = \Delta t_x \times \tan(\phi_1)$ in the first layer and $\Delta t_{y_2} = \Delta t_x \times \tan(\phi_2)$ in the second layer. The positive rotation angles ϕ_1 and ϕ_2 with positive indicate the exact octahedral rotation directions. The two tilt angles θ_1 and θ_2 are the same, but the signs are opposite because the bilayered octahedra share one common oxygen atom. Therefore, the rotation and tilt angle can be determined from refinement with the global minimum R_p. Figure 4.9. and Table 4.1 label and list the initial positions of the different atoms in each of the five layers of the

surface in units of surface cells. The lattice constants of the surface cells are determined by multiplying a constant $\sqrt{2}$ from the lattice constants of the bulk tetragonal unit cell as shown in Table 4.2 so that the actual Cartesian coordinates (*x, y, z*) of the atoms in each layer of the surface are achieved by multiplying them by lattice parameters.

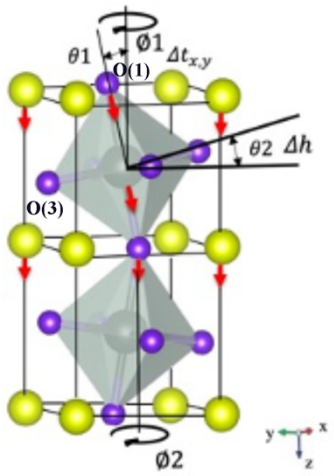

Figure 4.8. View of the surface bilayered octahedra with different rotation angles ϕ_1, ϕ_2 and two tilt angles θ_1 and θ_2 . The vertical shift of oxygen atoms is estimated with Δh. Δt_x and Δt_y estimate the (*x, y*) coordinate shifts of O1 and O3 from the octahedral rotation.

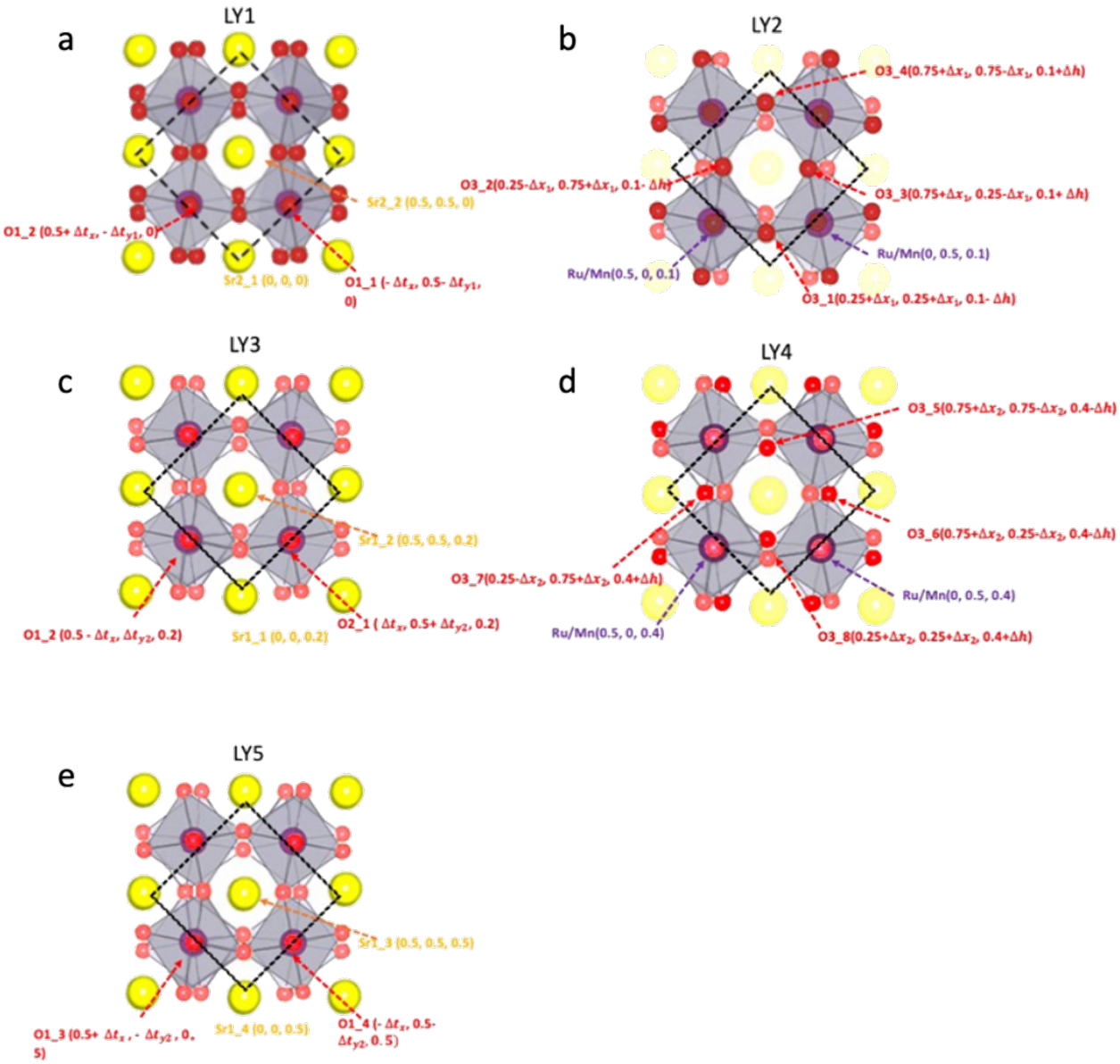

Figure 4.9. : Positions of different atoms in each surface layer. Each equivalent atomic site position is estimated with $\Delta h, \Delta t_x$ and Δt_y as a function of the surface octahedral rotation and tilt.

Table 4.1: Atomic coordinates for a total of 5 planes and 24 atoms in the top surface octahedra with the symmetry consideration. All fit parameters are given in unit length, and the actual Cartesian coordinates (*x, y, z*) are from multiplying by the lattice parameter.

#	Atom	*x*	*y*	*z*
1	Sr2_1	0	0	0
2	Sr2_2	0.5	0.5	0
3	O1_1	$-\Delta t_x$	$0.5-\Delta t_{y1}$	0
4	O1_2	$0.5+\Delta t_x$	$-\Delta t_{y1}$	0
5	O3_1	$0.25+\Delta x_1$	$0.25+\Delta x_1$	$0.1-\Delta h$
6	O3_2	$0.25-\Delta x_1$	$0.75+\Delta x_1$	$0.1-\Delta h$
7	Ru/Mn	0	0.5	0.1
8	Ru/Mn	0.5	0	0.1
9	O3_3	$0.75+\Delta x_1$	$0.25-\Delta x_1$	$0.1+\Delta h$
10	O3_4	$0.75-\Delta x_1$	$0.75-\Delta x_1$	$0.1+\Delta h$
11	O2_1	Δt_x	$0.5+\Delta t_{y_2}$	0.2
12	O2_2	$0.5-\Delta t_x$	Δt_{y2}	0.2
13	Sr1	0	0	0.2
14	Sr1	0.5	0.5	0.2
15	O3_5	$0.75-\Delta x_2$	$0.75-\Delta x_2$	$0.4-\Delta h$
16	O3_6	$0.75+\Delta x_2$	$0.25-\Delta x_2$	$0.4-\Delta h$
17	Ru/Mn	0.5	0	0.4
18	Ru/Mn	0	0.5	0.4
19	O3_7	$0.25-\Delta x_2$	$0.75+\Delta x_2$	$0.4+\Delta h$
20	O3_8	$0.25+\Delta x_2$	$0.25+\Delta x_2$	$0.4+\Delta h$
21	O1_3	$0.5+\Delta t_x$	$-\Delta t_{y2}$	0.5
22	O1_4	$-\Delta t_x$	$0.5-\Delta t_{y2}$	0.5
23	Sr2_3	0.5	0.5	0.5
24	Sr2_4	0	0	0.5

Table 4.2 : Lattice parameters of $Sr_3(Ru_{1-x}Mn_x)_2O_7$ (x = 0, 0.08, 0.16, 0.23 and 1) surface unit cells.

x	a (Å)	b (Å)	c (Å)
0	5.474	5.474	20.798
0.08	5.519	5.519	20.663
0.16	5.523	5.523	20.613
0.23	5.516	5.516	20.385
1.0	5.401	5.401	20.15

Phase calculations based on a given surface or bulk slab are performed by implementing a modified symmetrized auto-tensor SATLEED package [71]. This method uses the optimized muffin-tin (OMT) potential for the excited states of the surface plate proposed by Rundgren [77] to eliminate the quasi-standing waves and resonant behavior near the atomic radius. The electron density of the neighboring atoms is determined iteratively and superimposed to the next closest atomic unit to reach a predetermined electron density limit. For calculating the doped samples, we used the *t*-matrix approximation by modifying the subroutine in the program [77]. The phase shifts of the surface slabs calculated by the OMT method are shown in Figure. 4.10., where neutral and uniformly charged atoms have no significant effect on the phase shift. The internal potential V_o = $V_o(E) = V_{or}(E) + iV_{oi}(E)$ of the complex oxide surface contains two parts of the energy-dependent real part $V_{or}(E)$ and imaginary part $V_{oi}(E)$ with the relationship:

$$V_{or}(E) = \begin{cases} \text{const}, & \text{for } E < E_c \\ A_0 + \frac{A_1}{\sqrt{E+A_2}}, & \text{for } E > E_c \end{cases} \quad (4.1).$$

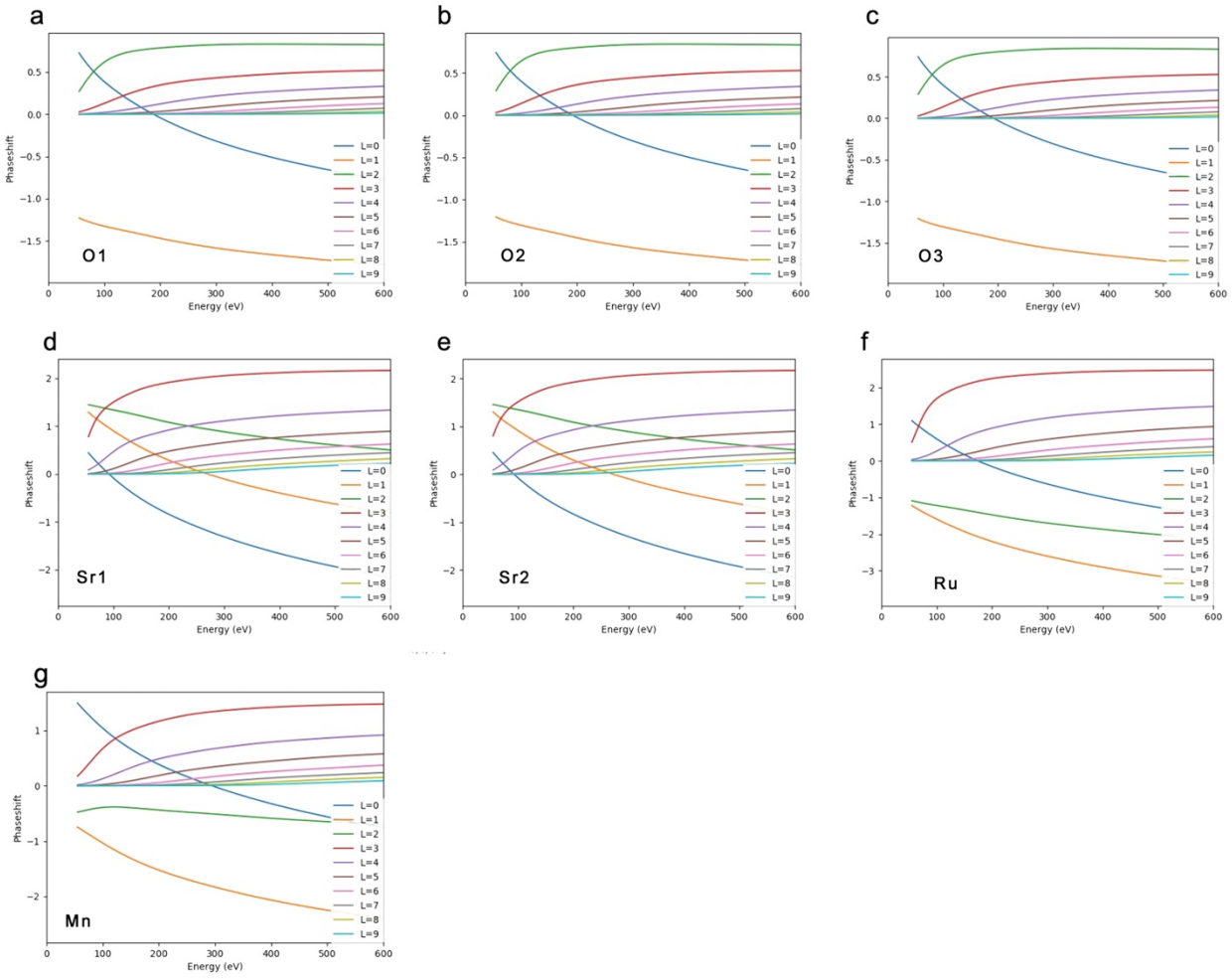

Figure 4.10. Plots of the calculated phase shift for 7 atoms using OMT method in $Sr_3(Ru_{1-x}Mn_x)_2O_7$. No significant change in the phase shift was observed for the same elements (Sr1 vs Sr2, and O1, O2, O3).

Through the phase shift calculations, we obtain the cutoff energy E_c =11.2V, A_0 = - 0.12, A_1 = - 46.62, and A_2 = 21.30, where the cutoff energy and coefficients are used in the subroutine for the modified electron beam energy calculations. We used a differential evolution (DE) algorithm for the optimization of the surface structure solution. The DE algorithm achieves global minimum optimization by searching an ample space using a simple Python package [103]. The parameter used for the search is the R-factor, which is used to find the minimum difference

between the model structure and the experimental I-V. The maximum value of the relaxation of each atom under the symmetry constraint was set to < 0.05 Å, and the robustness of this solution is typically tested by varying one of the fitting parameters to check the deviation from the global minimum R_p visually. The whole searching process consists of the following steps. (1) The rotation angle $\emptyset_1$ of the top bilayer is first optimized while fixing the second layer $\emptyset_2$. Due to the penetration depth limit of LEED, it is expected o be more sensitive in finding $R_p(\emptyset_{1minimum})$. (2) Using $\emptyset_1 = \emptyset_{1minimum}$, the rotation angle $\emptyset_2$ of the second layer was optimized. Different rotation directions and amplitudes were tested, and $R_p(\emptyset_{1minimum},\emptyset_{2minimum})$ was obtained. (3) An additional step was performed for $x < x_c$, and the tilt angle θ was optimized with ($\emptyset_{1minimum}$, $\emptyset_{2minimum}$). (4) The vertical atomic displacements were performed under the allowed coordinates as discussed in the previous section. (5) The final step is the optimization of the surface Debye temperature θ_D for each element. Due to the low accuracy of the determination of θ_D, steps (1)-(4) are first repeated until the DE terminates with a reasonable level of convergence in the resulting R_p.

The uncertainty associated with the atomic motion is determined by the divergence of the structure in the range (R_{pmin} - var(R_p), R_{pmin} + var(R_p)) as shown in Figure 4.11. The lowest global minimum of R_p is marked with a red cross, and the deviation from this structure in the range determined by var(R_p) is marked with a dashed line to resolve the associated uncertainty. Figure 4.12 shows a comparative plot of selected experimentally and theoretically generated IV curves corresponding to the surface structural refinement results for $Sr_3(Ru_{1-x}Mn_x)_2O_7$ (x = 0, 0.08, 0.16, 0.2 and 1) samples at 77 K with ten different individual curves for each sample listed separately. The refined surface structural parameters and the total R_p values are listed in Table 4.3. The selected bulk bond lengths are listed for comparison. The optimized parameters of

$Sr_3(Ru_{0.84}Mn_{0.16})_2O_7(001)$ surface structure at two temperatures, 77 K and 25 K, are listed in Table 4.4, and its optimized surface Debye temperature for different elements is shown in Table 4.5.

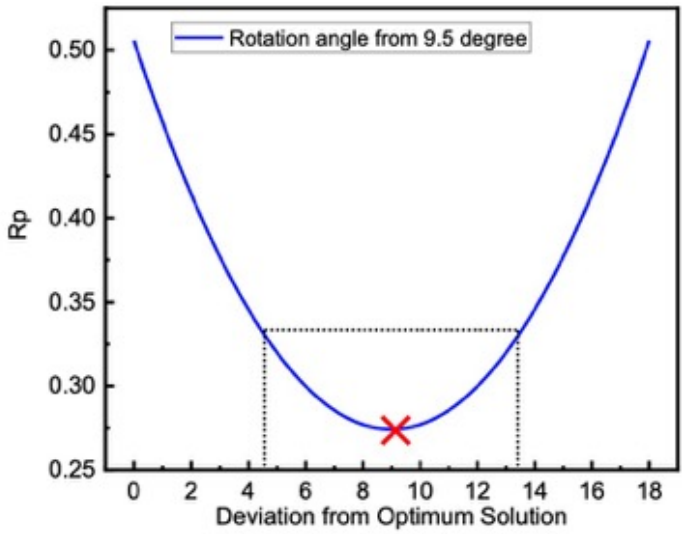

Figure 4.11. Determination of relative uncertainties in the top layer surface octahedral rotation by the $\mathrm{var}(R_p)$ for $Sr_3(Ru_{0.84}Mn_{0.16})_2O_7$ (001) at 77 K. The global optimization was achieved for $\emptyset_1 = (9 \pm 5)^{\circ}$ marked by minimum R_p in the red cross. The corresponding uncertainty was then obtained from the black dashed line in the bounds shown in the plot ($R_{P\min}$ - $\mathrm{var}(R_p)$, $R_{p\min}$ + $\mathrm{var}(R_p)$

a

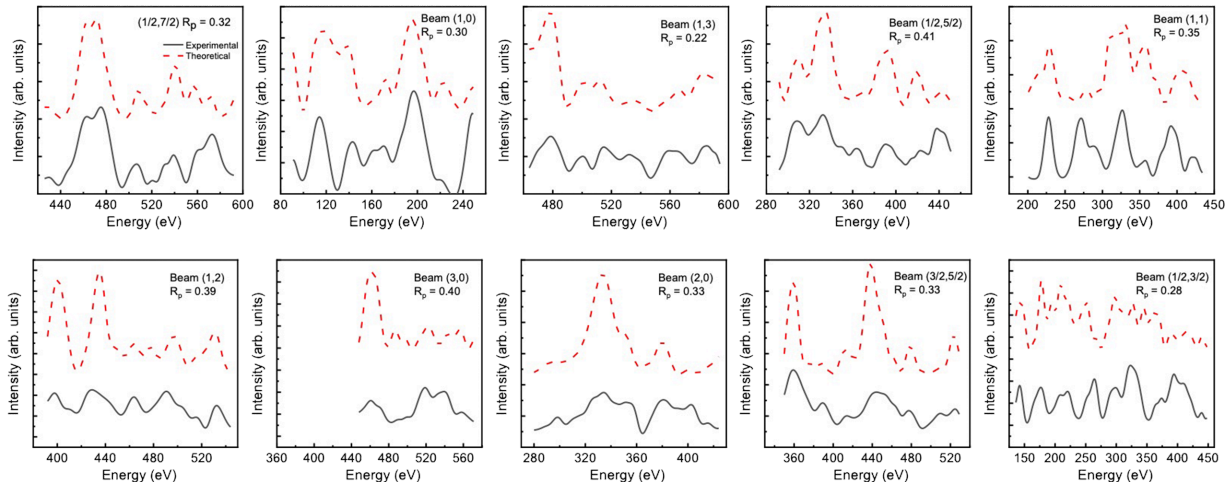

Figure 4.12. Selective comparison of averaged experimental (black) and theoretically generated IV curves (red) for (a) $Sr_3Ru_2O_7(001)$. (b) $Sr_3(Ru_{0.92}Mn_{0.08})_2O_7$ (001). (c) $Sr_3(Ru_{0.84}Mn_{0.16})_2O_7$ (001). (d) $Sr_3(Ru_{0.80}Mn_{0.23})_2O_7$ (001).(e) $Sr_3Mn_2O_7$ (001) surfaces at 77 K.

(fig. cont'd.).

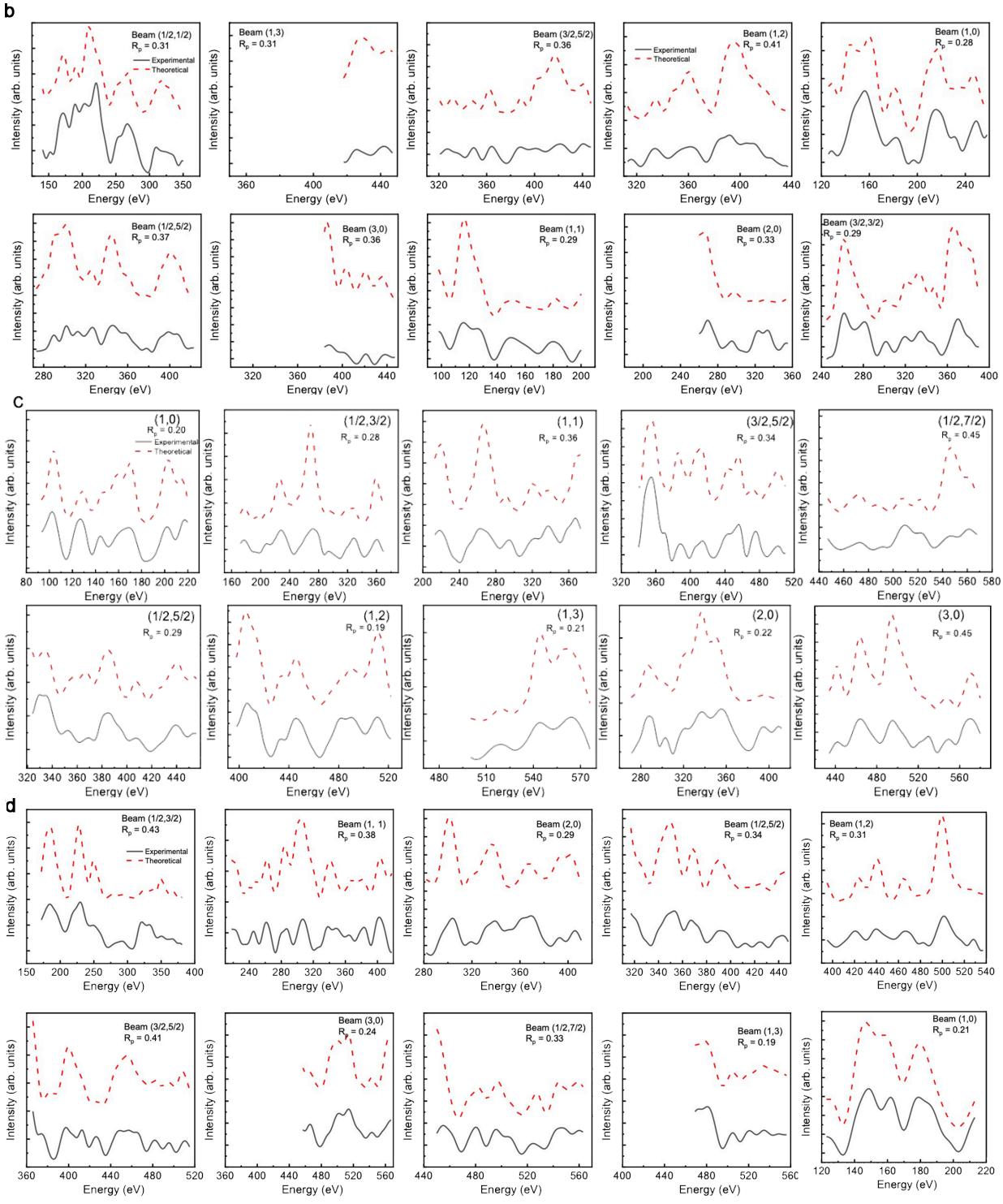
b
Beam (1/2,1/2)
Rp = 0.31
Experimental
Theoretical
Beam (1,3)
Rp = 0.31
Beam (3/2,5/2)
Rp = 0.36
Beam (1,2)
Rp = 0.41
Beam (1,0)
Rp = 0.28
Beam (1/2,5/2)
Rp = 0.37
Beam (3,0)
Rp = 0.36
Beam (1,1)
Rp = 0.29
Beam (2,0)
Rp = 0.33
Beam (3/2,3/2)
Rp = 0.29
Intensity (arb. units)
Energy (eV)
c
(1,0)
Rp = 0.20
Experimental
Theoretical
(1/2,3/2)
Rp = 0.28
(1,1)
Rp = 0.36
(3/2,5/2)
Rp = 0.34
(1/2,7/2)
Rp = 0.45
(1/2,5/2)
Rp = 0.29
(1,2)
Rp = 0.19
(1,3)
Rp = 0.21
(2,0)
Rp = 0.22
(3,0)
Rp = 0.45
d
Beam (1/2,3/2)
Rp = 0.43
Experimental
Theoretical
Beam (1, 1)
Rp = 0.38
Beam (2,0)
Rp = 0.29
Beam (1/2,5/2)
Rp = 0.34
Beam (1,2)
Rp = 0.31
Beam (3/2,5/2)
Rp = 0.41
Beam (3,0)
Rp = 0.24
Beam (1/2,7/2)
Rp = 0.33
Beam (1,3)
Rp = 0.19
Beam (1,0)
Rp = 0.21

(fig. cont'd.).

e

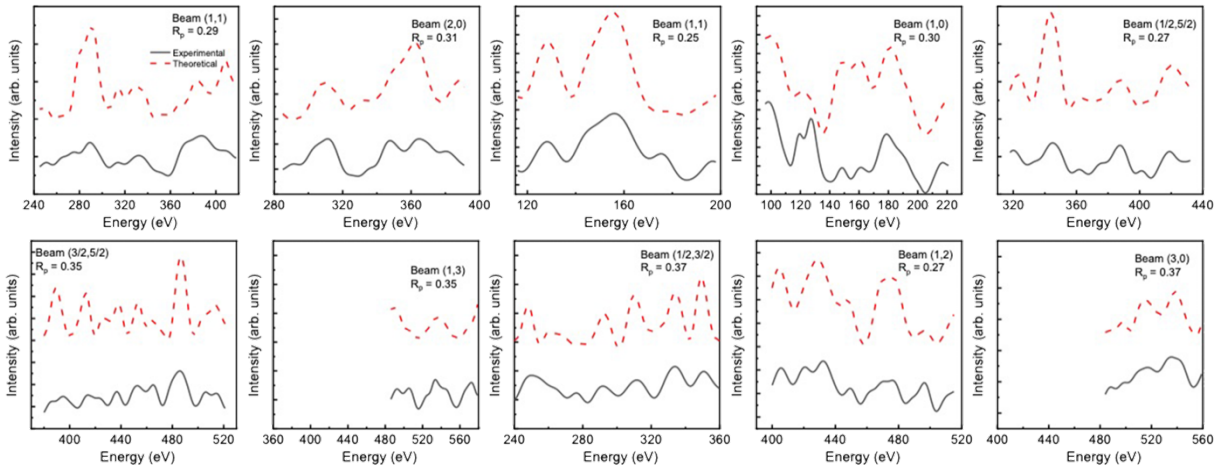
Beam (1,1)
R_p = 0.29
Experimental
Theoretical
Beam (2,0)
R_p = 0.31
Beam (1,1)
R_p = 0.25
Beam (1,0)
R_p = 0.30
Beam (1/2,5/2)
R_p = 0.27
Beam (3/2,5/2)
R_p = 0.35
Beam (1,3)
R_p = 0.35
Beam (1/2,3/2)
R_p = 0.37
Beam (1,2)
R_p = 0.27
Beam (3,0)
R_p = 0.37
Intensity (arb. units)
Energy (eV)

Table 4.3. Refined $Sr_3(Ru_{1-x}Mn_x)_2O_7$ (x = 0, 0.08, 0.16, 0.23, and 1) (001) surface structures at 77 K. The atomic displacement (Å) was compared to the bulk truncated structure from SXRD refinement, and the motion was constrained along (001) direction. The bulk Ru/Mn – O2, Ru/Mn – O1, Ru/Mn – O2, and octahedral rotation and tilt angles are listed for comparison.

Parameter	$Sr_3Ru_2O_7$	$Sr_3(Ru_{0.92}Mn_{0.08})_2O_7$	$Sr_3(Ru_{0.84}Mn_{0.16})_2O_7$	$Sr_3(Ru_{0.8}Mn_{0.23})_2O_7$	$Sr_3Mn_2O_7$
Displacement (Å)					
ΔZ1(O2)	(0.05±0.04)	(0.07±0.04)	(0.04±0.02)	(0.02±0.03)	(0.06±0.07)
ΔZ2(Sr2)	(0.03±0.04)	(0.04±0.04)	(0.01±0.03)	(0.04±0.02)	(0.04±0.03)
ΔZ3(Ru/Mn)	(0.03±0.02)	(0.03±0.02)	(-0.01±0.03)	(-0.02±0.04)	(0.00±0.01)
ΔZ4(O3)	(0.04±0.02)	(0.03±0.02)	(-0.06±0.04)	(-0.07±0.04)	(-0.01±0.02)
ΔZ5(O1)	(0.04±0.05)	(0.03±0.02)	(0.01±0.04)	(0.03±0.02)	(0.03±0.02)
ΔZ6(Sr1)	(0.02±0.03)	(0.04±0.03)	(0.01±0.02)	(0.02±0.03)	(0.03±0.03)
Bond length(Å)					
Ru/Mn – O2	(2.10±0.05)	(2.00±0.03)	(2.0±0.1)	(2.0±0.1)	(1.90±0.03)
	Bulk: 2.05	Bulk: 2.02	Bulk: 2.01	Bulk: 1.99	Bulk: 1.91
Ru/Mn – O3	(1.95±0.03)	(1.95±0.07)	(1.98±0.06)	(1.95±0.03)	(1.89±0.06)
	Bulk: 1.96	Bulk: 1.95	Bulk: 1.97	Bulk: 1.96	Bulk: 1.91
Ru/Mn – O1	(2.04±0.06)	(2.01±0.03)	(2.04±0.04)	(2.03±0.08)	(1.97±0.05)
	Bulk: 2.03	Bulk: 2.01	Bulk: 2.02	Bulk: 1.99	Bulk: 1.95
Angle (∘)					
$(Ru/Mn)O_6$ rotation ϕ_1	(12±5)	(10±4)	(8±4)	(5±3)	(1±2)
	Bulk:8.0	Bulk:7.3	Bulk:5.8	Bulk: 0.0	Bulk: 0.0
$(Ru/Mn)O_6$ rotation ϕ_2	(10±3.0)	(9.0±4)	(8±4.0)	(4.0±3.0)	(0.0±1.0)
$(Ru/Mn)O_6$ tilt θ	(2.5±1.0)	(1.0±0.8)	0	0	0
R_p	0.27 ± 0.03	0.25 ± 0.04	0.28 ± 0.05	0.26 ± 0.04	0.29 ± 0.06

Table 4.4. Optimized surface Debye temperature for the elements in of $Sr_3(Ru_{0.84}Mn_{0.16})_2O_7$ at a specular angle. θ_D from XRD (K) are determined from mean square displacements from bulk XRD refinement. The surface Debye temperature was much smaller than the bulk values.

Elements	Atomic Weight (amu)	θ_D from XRD (K)	θ_D (K) from LEED 77K	θ_D (K) from LEED 20K
O	15.990	600	360(80)	270(85)
Mn	54.901	420	220(45)	150(55)
Sr	87.620	258	130(55)	120(40)
Ru	101.070	420	320(75)	240(60)

Table 4.5. Temperature dependence of the optimized structure of $Sr_3(Ru_{0.84}Mn_{0.16})_2O_7$ (001) surface at 77 K and 25 K. Bulk values for the octahedra rotation and Ru-O distances are presented for comparison.

Fitting parameter	77 K	25 K
Displacement (Å)		
ΔZ1(O2)	(0.04±0.02)	(0.08±0.05)
ΔZ2(Sr2)	(0.01±0.03)	(0.05±0.04)
ΔZ3(Ru/Mn)	(-0.01±0.03)	(-0.05±0.03)
ΔZ4(O3)	(-0.06±0.04)	(-0.04±0.02)
ΔZ5(O1)	(0.01 ±0.04)	(0.03 ±0.04)
ΔZ6(Sr1)	(0.01±0.02)	(0.01±0.03)
Bond length(Å)		
Ru/Mn – O2	(1.99±0.05)	(1.92±0.08)
	Bulk: 2.01	Bulk: 2.02
Ru/Mn – O3	(1.98±0.07)	(1.98±0.05)
	Bulk: 1.97	Bulk: 1.96
Ru/Mn – O1	(2.04±0.07)	(2.07±0.07)
	Bulk: 2.02	Bulk: 2.01
Angle (∘)		
$(Ru/Mn)O_6$ rotation ϕ_1	(9.0±4.0)	(6±4)
	Bulk:5.8	Bulk: 0.55
$(Ru/Mn)O_6$ rotation ϕ_2	(8±4)	(5±4)
$(Ru/Mn)O_6$ tilt θ	0	0
R_p	0.28 ± 0.05	0.28 ± 0.04

The above experimental results demonstrated that the cleaved $Sr_3(Ru_{1-x}Mn_x)_2O_7$ ($x = 0$, 0.08, 0.16, 0.23, and 1) (001) surfaces have different lattice symmetries, and the C_{4v} symmetry of the surface is reduced to C_{2v} when the sample surface octahedra are tilted. The x_c surface shows no change in the lattice symmetry for the variable temperature experiments from 77 K to 25 K. We also performed an independent LEED IV analysis for each collected experimental IV data. The structure of the surface octahedra is shown in Figure 4.13. The top surface octahedra are compressed asymmetrically. The top O2 and Sr2 planes have the largest inward motion and the Ru/Mn-O1 bond length is smaller than the Ru/M-O2 bond length as shown in Figure 4.13a-d. The Ru/Mn-O2 and Ru/Mn-O3 bond lengths and octahedral volumes are largest on the x_c surface. The Jahn-Teller distortion δ_{JT} calculated from the bond lengths is also the smallest on the x_c surface (Figure 4.13e). In Figure 4.13f, the rotation of the surface $(Ru/Mn)O_6$ octahedra is always a few degrees larger than its bulk value and decreases gradually with x. For the end compound, the reference structure for $x = 1.0$ is the bulk truncated tetragonal structure with no sign of $(Ru/Mn)O_6$ rotation. This trend of decreasing rotation angle has similarities with the bulk structure. In Tables 4.3- 4.4, when the surface octahedron tilt is present, the tilt angle of the $x = 0.08$ surface octahedra decreases to ~1.0° compared to the 2.5° tilt angle of the $x = 0$ surface and disappears at the x_c surface. For the sample surface of x_c, there seems to be a thermal contraction of the surface layer as the system cools. While the surface structural parameters change in the bulk MIT, the $(Ru/Mn)O_6$ rotation does not significantly change. The x_c surface structure at 25 K has a static nature, and the Ru/Mn-O2, Ru/Mn-O3 bond lengths at 25 K are similar to the values at 77 K. Hence, the octahedra do not flatten significantly, and the bandwidth and orbital occupancy should also not change. The surface thus retains its metallicity at 25 K for x_c. Even these small structural differences between the bulk and surface can profoundly affect the electronic properties. This

surface atomic motion produces IR-activated bulk Raman modes at the surface. The lattice dynamics at the sample surface will be discussed next.

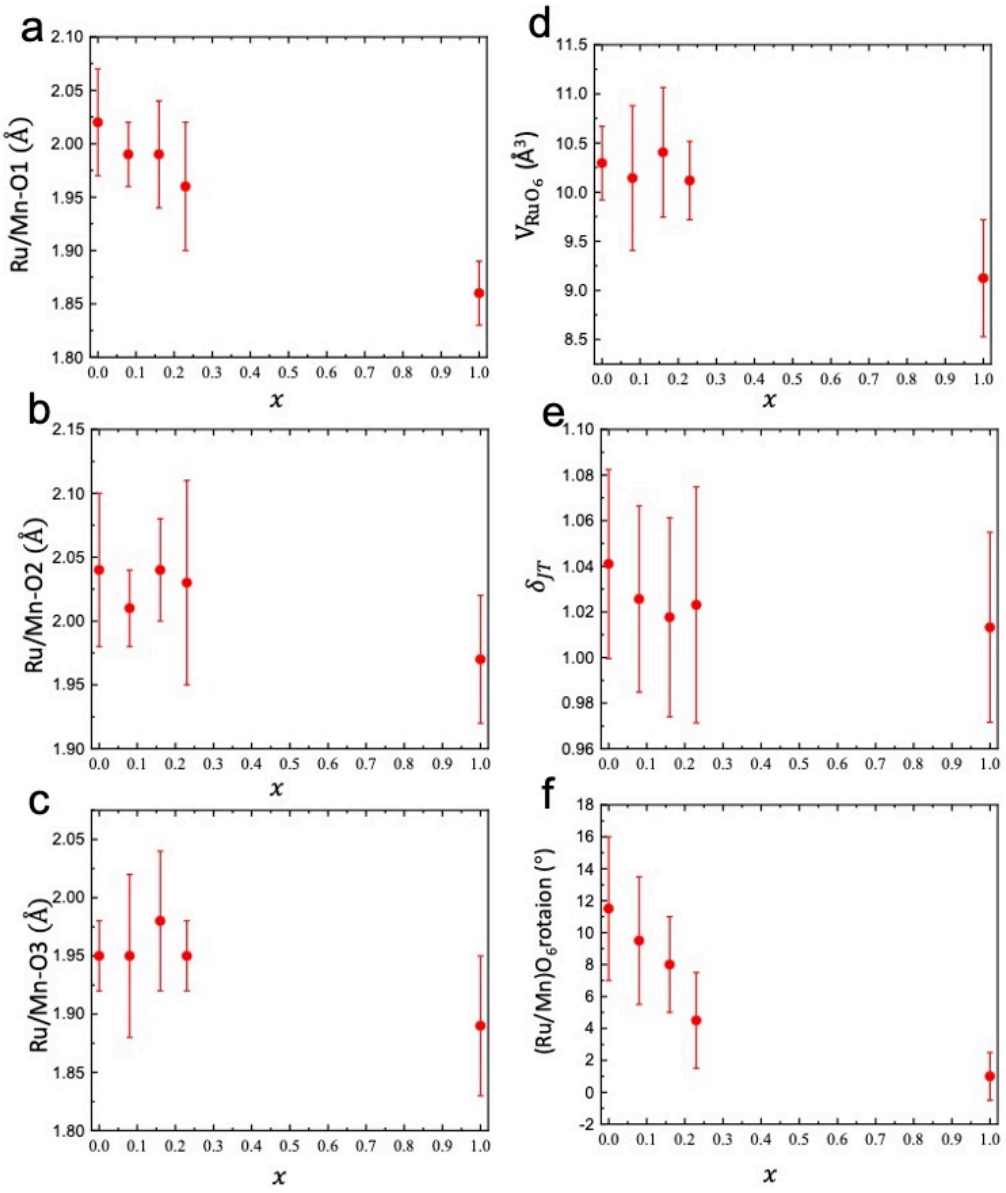

Figure 4.13. Different bond lengths, volume, Jahn-Teller distortion (δ_{JT}) and rotation angle for $Sr_3(Ru_{1-x}Mn_x)_2O_7$ (001) surface octahedra refined using LEED I-V at 77 K. (a) Ru/Mn-O1, (b)Ru/Mn-O2, and (c)Ru/Mn-O3 bond lengths. (d) Volume of the surface octahedron. (e) δ_{JT} calculated from the bond lengths. (f) Rotation angle of the surface octahedron.

4.2 HREELS Analysis of $Sr_3(Ru_{1-x}Mn_x)_2O_7$ (x = 0, 0.08, 0.16, 0.23, and 1)

Although LEED images at different temperatures show no change in the symmetry of the $Sr_3(Ru_{1-x}Mn_x)_2O_7$ sample surface over the temperature range measured by HREELS (77 K - 25 K), the surface atoms have different displacements. Similar to the surface of single-layered Sr_2RuO_4, the induced strain on the surface freezes the phonons at the boundary, causing the RuO_6 octahedron to rotate, changing the overall phonon spectrum and leading to an increase in phonon energy [104]. We can assume that the phonon modes on the surface of $Sr_3(Ru_{1-x}Mn_x)_2O_7$ are also influenced by its surface structure.

To probe the electronic and lattice dynamics at the crystal surface, HREELS directly detects the dielectric response at the surface by quasi-particle excitations (e.g., phonons and protons, and intra-band transitions in Drude metals) [105]. Before HREELS measurements, we take LEED images to ensure the quality of the cleaved surface and the absence of significant surface defects. Another challenge we met is the charging between the sample and silver epoxy interface, which we surmounted by brushing the Electrodag 1415M solution of graphite to maintain low resistance such that the incident electron beam at 7 - 20 eV is not exposed to epoxy. After quantitative LEED-IV structure analysis of the $Sr_3(Ru_{1-x}Mn_x)_2O_7$ surface was performed in the previous section, the HREELS measurements were all collected in a specular arrangement with an incidence angle of 70° and an instrumental resolution of ~2 meV. There are five dipole-active optical phonons obtained from the Sr_2RuO_4 surface: $A_{2u}(1)$, $A_{2u}(2)$, $A_{2u}(3)$, $A_{1g}(1)$, and $A_{1g}(2)$ which are shown in Figure 4.14s [106]. The surface phonons have significantly higher energies than the corresponding modes in the bulk. $Sr_3(Ru_{1-x}Mn_x)_2O_7$ has similar phonon modes, but due to the observed large terraces and tilt domains on the cleaved surface, there is a wide range of incident

electron angles that degrade the inelastic spectrum. Thus, only the most vital $A_{1g}(2)$ oxygen stretching mode is evident.

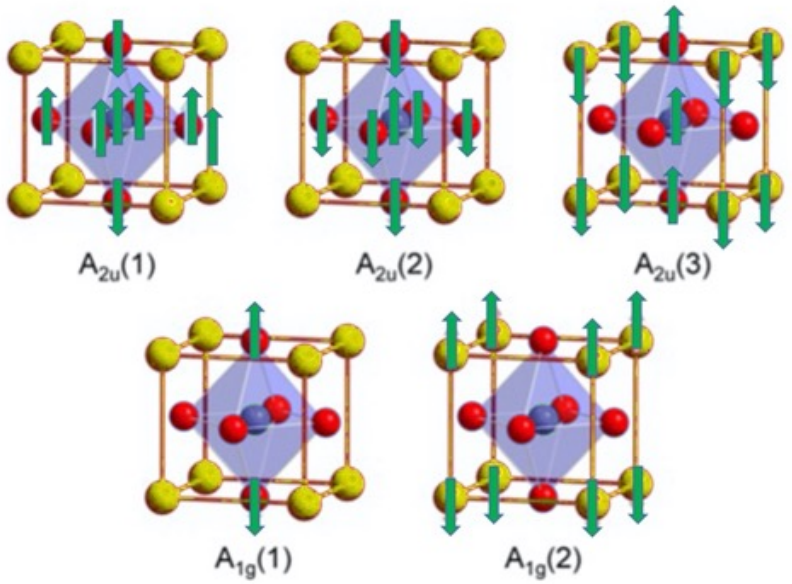

Figure 4.14. Surface dipole active optic phonon modes for a single-layered K_2NiF_4 structure. The movement of atoms is illustrated by green arrows [106].

Figure 4.15. illustrates the loss spectra of the x_c surface at 77 K with the strongest $A_{1g}(2)$ mode around ~75meV which is larger than the corresponding bulk phonon energy (~71.5 meV) [106]. In Figure 4.15a., we fit the left side of the elastic peak centered at 0 meV using a Gaussian function and then remove the elastic peak and background from the raw data. As shown in Figure 4.15b., three of the visible peaks are labeled as $\omega_1 \sim 30$ meV, $\omega_2 \sim 50$ meV, and $\omega_3 \sim 75$ meV and correspond to $A_2u(3)$, $A_2u(2)$, and $A_{1g}(2)$ phonon modes. The background consists of the elastic peak, Drude tail, and Shirley background [58]. Since the Drude tail can also make the spectral peaks asymmetric, the inelastic spectrum in the region around the phonon is the convolution of the Drude tail and the $A_{1g}(2)$ phonon. After subtracting the Drude tail, the single $A_{1g}(2)$ surface phonon peak is fitted with a multi-Lorentz function as shown in Figure 4.15c. Since neither of the other two phonons has a good enough signal-to-noise ratio for line analysis, and the change of the surface

conductivity of $Sr_3(Ru_{1-x}Mn_x)_2O_7$ with x is obtained analytically from the $A_{1g}(2)$ surface phonon with its Fano lineshape [107-109].

The asymmetry of the ω_3 peak shows the surface metallicity due to the interference between the discrete resonance and the continuum background [110]. Discrete resonances here refer to phonon excitations, while electron-hole paired excitations are the continuum background in the HREELS experiment. The Fano parameter q is used to fit the Fano line shape of the ω_3 peak using the following function: $I(\omega) = \frac{I_u(\varepsilon+q)^2}{1+\varepsilon^2} + A_0$. The phonon energy ω_0 and the intrinsic linewidth Γ are obtained from the relation $\varepsilon = (\omega - \omega_0)\Gamma$. Therefore, if there is more DOS near the Fermi level, it leads to more excitations, and therefore, the fitting parameter q becomes smaller. The smaller q corresponds to a more asymmetric lineshape of the $A_{1g(2)}$ surface phonon peak and is a direct measure of the surface metallicity. Figure 4.16. shows the HREELS spectra of $Sr_3(Ru_{1-x}Mn_x)_2O_7$ (x = 0, 0.08, 0.16 and 0.23) (001) surfaces at 77 K. All data are normalized to the elastic peak as shown in Figure 4.16a. , and we observe that the intensity of the $A_{1g}(2)$ phonon remains constant for all measured surfaces, with the linewidth remaining at ~15 meV. The variation of the q parameter with x is demonstrated in Figure 4.16b, where the spectrum of the x_c sample surface has the most asymmetric peak shape and the smallest q value (~ 4.2). By comparing the magnitude of the values of q obtained from the fitting, the x_c surface has the best conductivity, followed by x = 0.23 (q = 7.5), x = 0.08 (q = 12.5), and x = 0 (q = 20.1). Also, the $A_{1g}(2)$ phonon energy is significantly shifted upward on the x_c surface, reaching ~ 76 meV, which is 6 meV higher than that observed on $Sr_3Ru_2O_7$. This upward shift of the surface phonon energy can be understood by the observed contraction of the Ru/Mn-O2 bond length between x_c and x = 0. For the end compound $Sr_3Mn_2O_7$, the HREELS spectrum is shown in Figure 4.17. The results indicate an insulating surface phase where only the elastic peak is visible. Thus, a relationship between surface structural

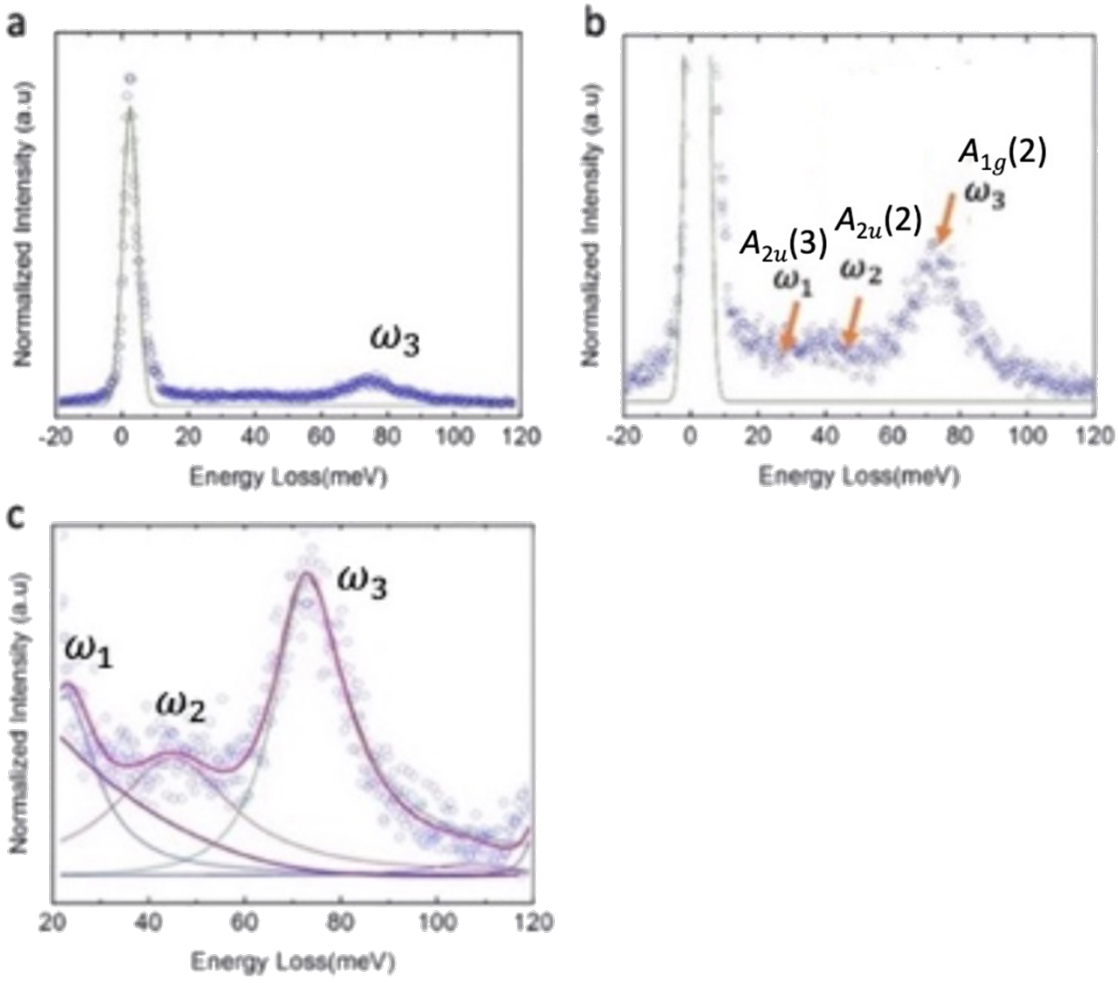

Figure 4.15. Illustration of the fitting process for the HREELS on x_c sample at 77 K. (a) Full HREELS spectra with a symmetric Gaussian function fitted elastic peak on the left side marked with a solid green line. A clear ω_3 peak is observed ~ 75meV. (b) Zoomed-in image of (a). The three different phonon modes are marked, where ω_1 and ω_2 correspond to the vibration and bending modes of Sr atoms along c-axis, respectively. Limited instrument resolution left the ω_3 of primary interest. (c) A multi-Lorentzian function was used to fit the above three peaks, and the ω_3 peak is fitted by the Fano lineshape. All three peaks are marked separately. The resultant fitting curve is shown across the dotted data points. The Drude spectral weight on the right side of the elastic peak and the Shirley background on the high energy side are subtracted.

and physical properties can be inferred from this, where the metal to poor metal transition is coupled to the tilt angle phase. Considering that the tilt angle is zero above x_c, the surface is more metallic and coupled to the rotation angle.

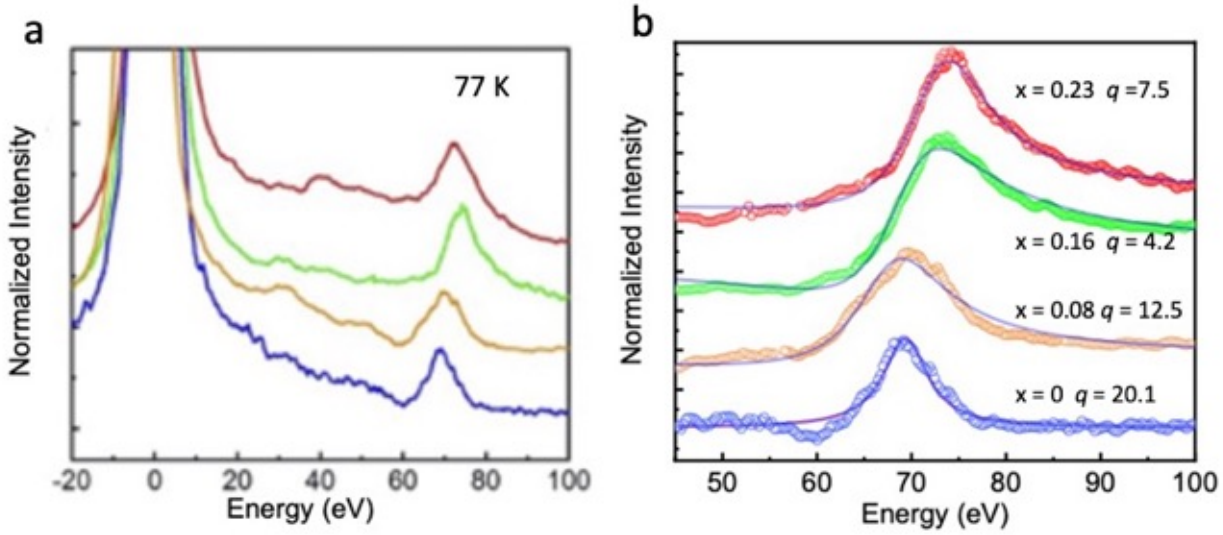

Figure 4.16. HREELS spectra on $Sr_3(Ru_{1-x}Mn_x)_2O_7$ surfaces at 77 K with an incident electron energy of 7.0 eV as a function of the Mn doping. (a) Zoomed-in image of the raw HREELS spectra with the elastic peak and all phonon peaks. (b) Fano q parameter for x = 0, 0.08, 0.16 and 0.23.

The phonon dynamics of the sample surface as a response to the insulating phase of the bulk AFM is investigated by temperature dependence HREELS measurements on the x_c surface. As shown in Figure 4.18, q value on x_c surface is labeled as a function of temperature. The phonon intensity remains constant during the cooling cycle. At 20K, there is a ~ 2 meV shift in phonon energy without a change of the phonon intensity. When the bulk enters the AFM insulating phase below 80K, the vibration of the apical oxygens changes according to LEED I-V analysis, corresponding to the elongation of the (Ru/Mn)-O2 bond length contributing to the downward shift of the phonon energy. However, the transfer of phonon energy is small, and we obtain relatively large uncertainties from LEED I-V ~ 0.06 Å. Thus, we conclude that x_c surface has a stable metallic

phase. Further STS measurements are necessary to investigate the presence of insulating gaps on the surface.

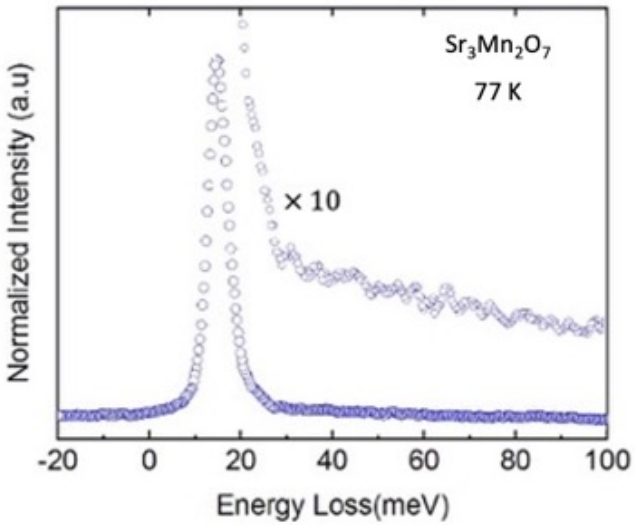

Figure 4.17. Specular HREELS spectrum of $Sr_3Mn_2O_7$ surface at 77 K demonstrating insulating surface behavior with obvious surface charging effect. The inset is 10 times zoomed-in image of the marked loss energy area.

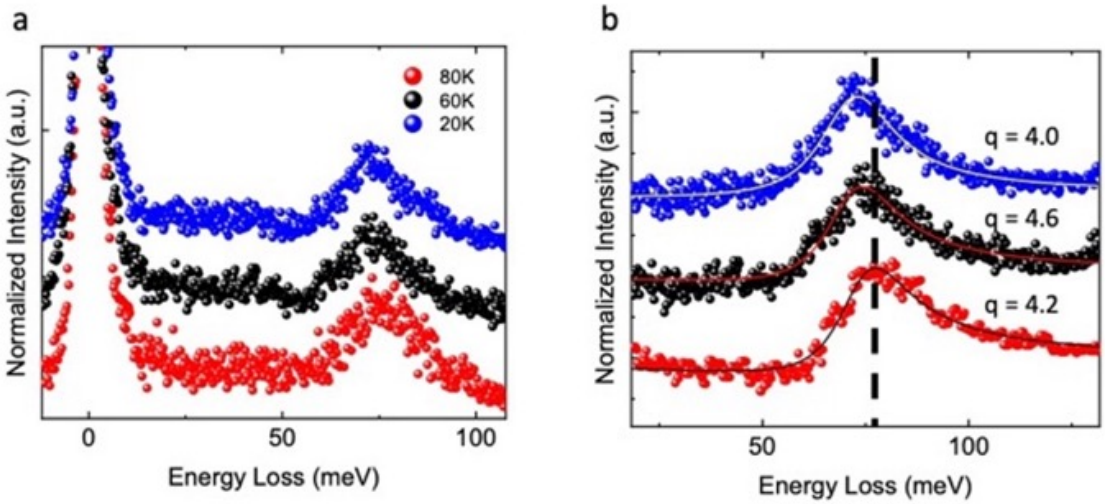

Figure 4.18. Temperature dependence of HREELS spectra of x_c surface. (a) Full HREELS spectra at 80 K, 60 K, and 20 K. (b) A fit the $A_{1g}(2)$ phonon peak after subtraction of the background and other peaks. The dashed line is added as a guide to the shift of phonon energy, and the Fano q parameter is included.

Chapter 5. Surface Electronic Properties of $Sr_3(Ru_{1-x}Mn_x)_2O_7$

5.1 STM Topographies of $Sr_3(Ru_{1-x}Mn_x)_2O_7$ (x = 0, 0.08, 0.16, 0.23, and 1)

In Chapter 4, we studied the effect of chemical doping on the surface lattice structures of single-crystal $Sr_3(Ru_{1-x}Mn_x)_2O_7$ through LEED measurements. We found that in addition to the rotational deformation of the octahedra seen in the bulk, there is a unique tilt deformation at the surface. Thus, the symmetry decreases from C_{4v} in the bulk to C_{2v} at the surface. For RP ruthenates, First principle calculations show that the structure of the RuO_6 octahedra determines the electronic structure near the Fermi energy [111]. Any change in the latter will affect the physical properties of the system (for both bulk and surface) [112]. Because of the tilt of the RuO_6 octahedron at the surface, it lowers the RuO_2 sheet which will affect its electronic structures [113]. In the absence of atomic surface reconstruction, the surface appears electronically ordered such that the surface DOS may contain features not present in the bulk [87].

An important question remains: what is the effect of chemical doping on the electronic structure and local density of states (LDOS) of the $Sr_3(Ru_{1-x}Mn_x)_2O_7$ surface? In this section, we study the electronic structure through STM and the effect of Mn on the LDOS disturbances such as local electronic inhomogeneities. The electronic/magnetic properties of $Sr_3(Ru_{1-x}Mn_x)_2O_7$ are also expected to change dramatically due to the evolution of the surface structure with Mn. Similar to the single layered $Ca_{2-x}Sr_xRuO_4$, the physical properties of Sr_2RuO_4 are also coupled with the RuO_6 structure [43,114]. The ferromagnetic (FM) metallic state is favored by the RuO_6 octahedral rotation. While octahedral tilt stabilizes the antiferromagnetic (AFM) insulating ground state. The STM topography of the cleaved surface of $Sr_3Ti_2O_7$ at 400 mK also demonstrates the feasibility of verifying the surface electronic structure [115]. With 3*d* Mn replacing 4*d* Ru, the Coulomb correlation is enhanced, and a long-range antiferromagnetic ordering appears in the bulk. The

response of the surface properties to the metal-to-insulator phase transition and magnetic transition of bulk at low temperatures is worth investigating. We chose x_c, corresponding to the highest bulk magnetic transition temperature, to study the changes in surface properties by continuous cooling and applied magnetic fields.

To achieve atomic resolution on the $Sr_3(Ru_{1-x}Mn_x)_2O_7$ surface, we use the etched Pt/Ir tip described in Chapter 2 and scan on a clean Au or Cu surface until reasonable resolution is achieved in the STS profile. Since the tunneling current is chemically insensitive, it is impossible to distinguish the corresponding atomic sites on the image. STM is only charge sensitive and not a structural tool to determine the lattice. To facilitate comparison of the surface electronic structures probed by STM, the bulk truncated $(\sqrt{2} \times \sqrt{2})$ R45° superstructure is marked with dashed squares in Figure 5.1a. The corresponding STM image is marked with the same colors as shown in Figure 5.1b. This structure is interpreted as a purely electronic effect at a given bias voltage of +7 mV. The metamagnetic phase transition occurring in $Sr_3Ru_2O_7$ is also demonstrated by the STS spectral weight transfer with the applied magnetic field [87]. The electronic and lattice structures of the $Sr_3Ru_2O_7$ surface in real and reciprocal space are shown in Figure. 5.1c and d. In addition to using spin-polarized STM, it is also possible to detect spin degrees of freedom indirectly by coupling them to charge and lattice, e.g., indirectly detecting spin information by combining non-spin sensitive surface techniques [57].

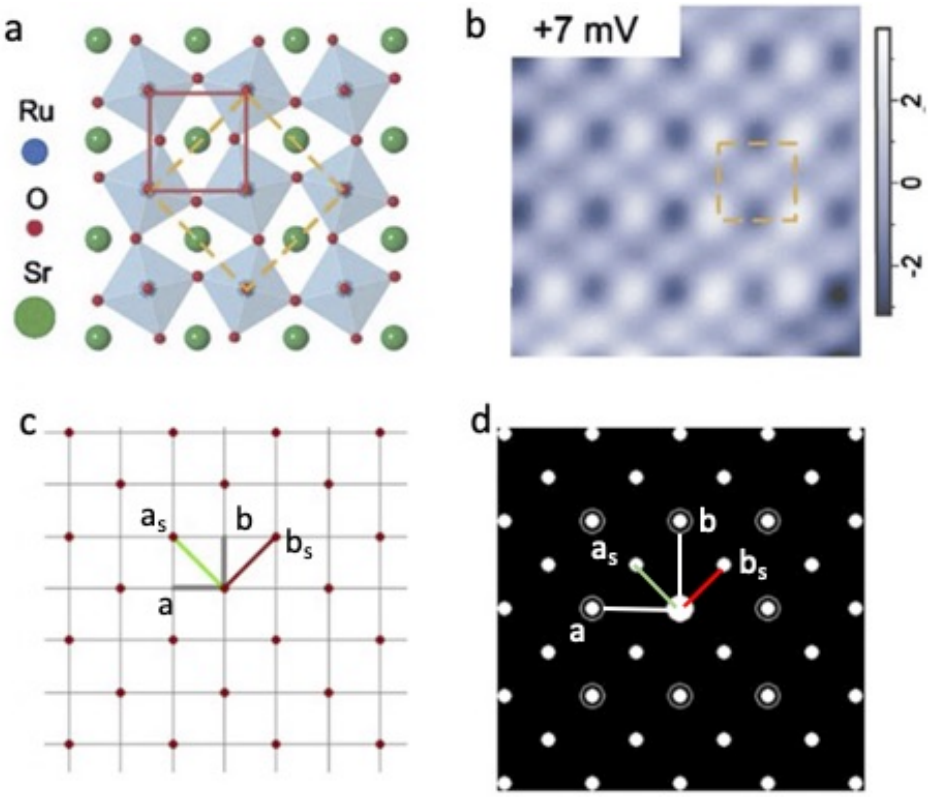

Figure 5.1. STM topography and the lattice structure of the $Sr_3Ru_2O_7$ (001) surface. (a) Surface structure of $Sr_3Ru_2O_7$ in the *ab* plane where Ru, Sr, and O atoms are labeled. The $(\sqrt{2} \times \sqrt{2})\, R45^{\circ}$ superstructure is shown as a dashed square, and the tetragonal unit cell is marked in a solid red square. (b) STM image of the $Sr_3Ru_2O_7$ surface with V_s = + 7mV. The atomic spacing is checked with the consistent values of the lattice constants. Figure adapted from Ref. [87]. (c-d) $(\sqrt{2} \times \sqrt{2})\, R45^{\circ}$ superstructure in the real and reciprocal space. The tetragonal unit cell is described with the vector a, b, and the superstructure are marked with a_s and b_s.

5.1.1 Surface tilt-induced C_{2v} symmetry on $Sr_3(Ru_{1-x}Mn_x)_2O_7$ (x = 0, 0.08, 0.16, 0.23, and 1)

$Sr_3(Ru_{1-x}Mn_x)_2O_7$ has a layered structure, it is cleaved at the weak bonds between octahedral bilayers, thus exposing a pristine Sr-O terminated layer. A large and flat cleaved $Sr_3Ru_2O_7$ surface with terraces (V_s = -1.0 V, I_s = 100 pA) at 77 K is shown in Figure 5.2a, and the step height measured along the line drawn in the image is about one-half of the lattice constant as shown in Figure 5.2b. The step heights are of one-half the bulk tetragonal unit cell, indicating that

the terraces are parallel to the plane intersecting the center of the bilayered octahedra, and the cleaved surface is indeed Sr-O terminated. STM topography for $x = 0$, and 0.08. The corresponding fast Fourier transform (FFT) image are shown in Figure 5.3, where the bright sites correspond to the surface Sr atoms and the dark spots are the (Ru/Mn) sites in the second layer. The two Sr atoms in the figure are identical at the applied bias. The $(\sqrt{2} \times \sqrt{2})$ R45° surface superstructure is obtained by connecting the four sites with one Sr in the center. The value of the adjacent Sr-Sr spacing is 5.7 Å × 5.7 Å, which matches the lattice constant of the surface unit cell.

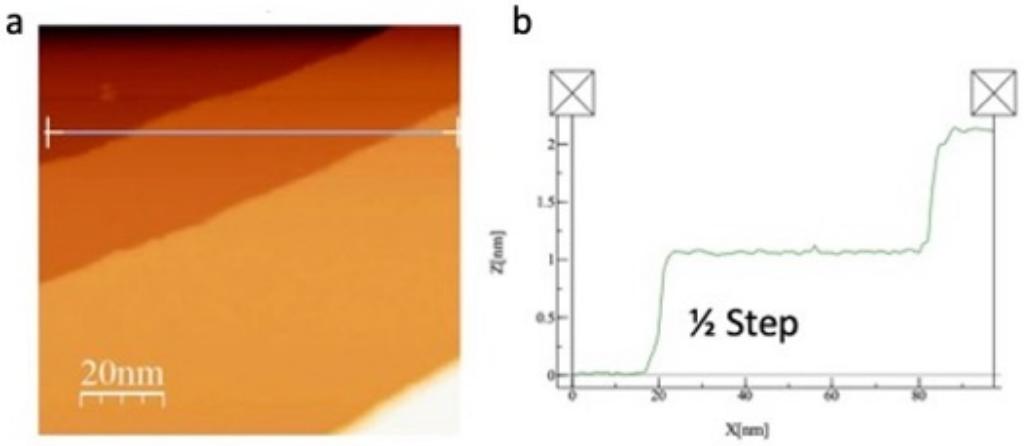

Figure 5.2. (a) Large 100 nm × 100 nm STM image showing a clean large surface with terrace/step morphology on the fresh cleaved $Sr_3Ru_2O_7$ (001) surface (V_s = -1.0 V, I_s = 100 pA) at 77 K (b) Height profile across the terraces of STM image across the line. The terrace is approximately one-half of the *c* value.

We observe similar STM images on the surface of the sample for $x = 0$ (V_s = -1.0 V, I_s = 90 pA) and $x = 0.08$ (V_s = 1.0 V, I_s = 80 pA) for 77K at different sample bias voltages as shown in Figure 5.3. For convenience, the fractional points with different intensities in the inset FFT image are marked in red and green, where two adjacent points have different intensities and two points on the diagonal have similar intensities. Fourier transform of the STM topography is important. The integer points represent the expected pattern of the bulk tet-(1×1) structure and the four integer spots have the identical intensities, while the fractional spots inside the circled points represent the

($\sqrt{2} \times \sqrt{2}$) R45° unit cell in the reciprocal space. If the surface has only octahedral rotation, the intensities of the four fractional spots in the FFT images are the same. The difference in intensity of the fractional spots in Figure 5.3 a and b is due to the tilted octahedron and is marked with a gradient color on the $(Ru/Mn)O_6$ octahedron in Figure 5.3c. This indicates that the electronic symmetry is broken at the surface of these two samples.

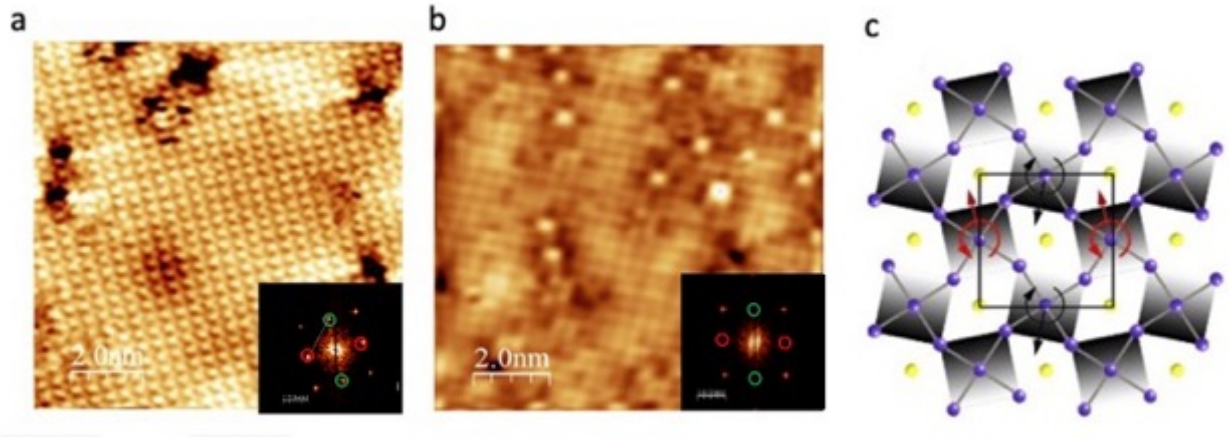

Figure 5.3. STM and the corresponding FFT image for $Sr_3(Ru_{1-x}Mn_x)_2O_7$ (a) x = 0.0 (V_s = -1.0 V, I_s = 90 pA) and (b) x = 0.08 (V_s = 1.0 V, I_s = 80 pA). The fractional spots in the inset FFT images are corresponding to the $(\sqrt{2} \times \sqrt{2})\ R45^{\circ}$ superstructure. Red and green circles mark the fractional spots with different intensities. The two spots in the diagonal line have similar intensities, and the neighboring fractional spots have different intensities. (c) Illustration of the surface $(Mn/Ru)O_6$ octahedral rotation and tilt. The center and corner octahedra have the opposite rotation direction, and the tilt direction is marked with the red arrow. The tilted plane is seen on the gradient color on $(Mn/Ru)O_6$ octahedra.

We can quantify the degree of surface octahedral tilt deformation by analyzing the intensity of the fractional and integer points in the corresponding FFT images. Assuming that the surface electronic symmetry is the same as the lattice, i.e., one of the glide lines is broken by the tilt, this should also be reflected in the FFT image of the STM image in reciprocal space. As illustrated in Figure 5.4a, the reduction of the surface electronic symmetry to C_{2v} is obtained by superimposing

octahedral rotation and tilt. Where four Sr positions are the same from rotation, and octahedral tilt

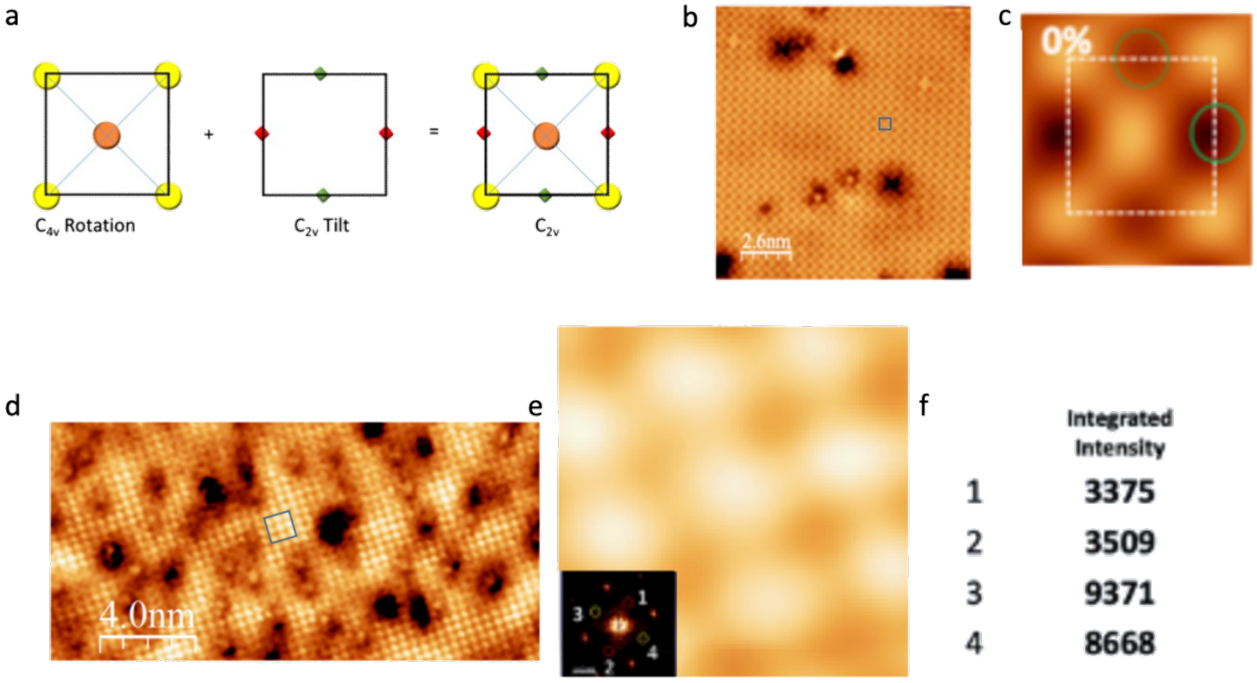

Figure 5.4. Illustration of the C_{2v} symmetry on the STM and the corresponding FFT image at 77 K. (a) The surface C_{2v} symmetry is an addition of four identical Ru/Mn sites and different Ru/Mn sites from octahedral tilt. The different colors represent the intensities of the different sites. (b) STM image of $Sr_3Ru_2O_7$ at 5 K (V_s = - 0.8V, I_s = - 70 pA). (c) Enlarged image of the blue box in the STM image of $Sr_3Ru_2O_7$, where the adjacent sites have distinctly different intensities. (d) STM image for x = 0.08 (V_s = - 0.2V, I_s = - 50 pA). (e) Zoomed-in image of the region marked by the blue box in the image, where the fractional points calculated from the FFT image are marked by different colors. (f) The table lists the intensities of the four fractional points in the FFT image, verifying the asymmetry of the neighboring points.

leads to two different surface Ru environments [43]. Figure 5.4b shows STM image at 5 K for $Sr_3Ru_2O_7$ (V_s = -0.8 V). A magnified image of the region in the blue square is shown in Figure 5.4c, where the marked white dashed squares connect four Sr sites. The nearby Ru/Mn sites are marked with dashed and solid circles, where a clear difference in intensity between them can be seen. For x = 0.08, we analyzed the FFT image of the corresponding STM images (V_s = -0.82V) in Figure 5.4d. A zoomed-in view of the blue region in the STM image is shown in Figure 5.4e,

where the intensity of the fractional sites in FFT images are different and are marked with different colors. The table of fractional point intensities in Figure 5.4f shows that the fractional point intensities of the two adjacent Ru/Mn dots differ by a factor of about 5, representing a clear C_{2v} symmetry on the surface at x = 0.08. These findings echo the results of the lattice structure of LEED in Chapter 4.

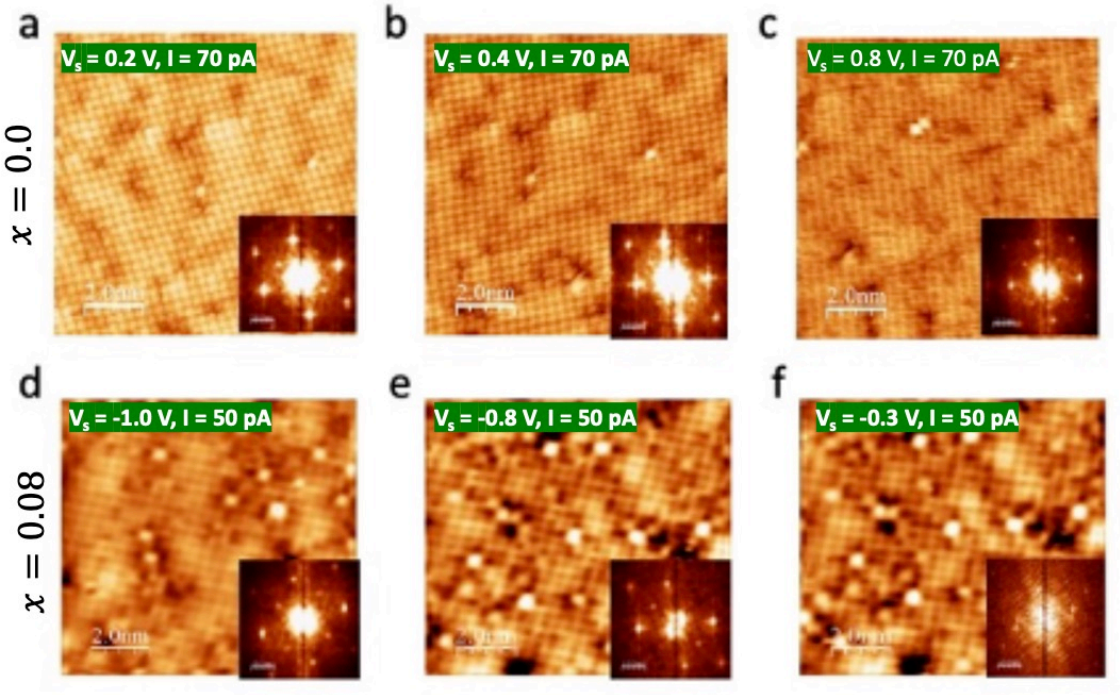

Figure 5.5. Sample bias voltage dependence of STM topography (8 nm × 8 nm) and the corresponding FFT image for $Sr_3(Ru_{1-x}Mn_x)_2O_7$ at 77 K. For x = 0, (a) V_s = 0.2 V, I_s = 70 pA, (b) V_s = 0.4 V, I_s = 70 pA, and (c) V_s = 0.8 V, I_s = 70 pA. For x = 0.08, (d) V_s = -1.0 V, I_s = 50 pA, (e) V_s = -0.8 V, I_s = 50 pA, and (f) V_s = -0.3 V, I_s = 50 pA.

By varying the bias voltage, the tunneling current between the tip and the sample surface changes the Fermi level with respect to the tungsten tip and similarly changes the displacement of the surface atoms [116]. As shown in Figure 5.5, the $(\sqrt{2} \times \sqrt{2})$ R45° superstructure of the surface can be observed in the corresponding FFT images for both x = 0 and 0.08 at different bias voltages of 77 K. Since the two surface RuO_6 octahedra are electronically equivalent, the O, Sr atoms, and Ru atoms at the top of the surface octahedra are indistinguishable. Thus the fraction we observe is

due to the Ru/MnO_2 of the sublayer. Also in the FFT images, the disappearance of the corresponding fractional points in Fig. 5.5a and e is due to the tip effect. The surface octahedral rotation does not vanish because we observe the fractional points under different biases, and the enlarged STM image also does not reveal a change in the electronic symmetry.

5.1.2 Rotation Induced C_{4v} Symmetry on $Sr_3(Ru_{1-x}Mn_x)_2O_7$ (x = 0.16 and 0.23) (001) Surfaces

For $x \geq 0.16$, the surface octahedral tilt vanishes and results in a C_{4v} lattice symmetry. The tilt should lead to electron anisotropy in the plane, i.e., different electron transport properties parallel and perpendicular to the tilted surface. However, for the octahedral rotation only case, the two RuO_6 octahedra rotate in *cw*/*ccw* directions with identical electronic environments. As shown in Figure 5.6, the STM topology and FFT image at 77 K for x_c correspond to the pure octahedral rotation case where the four fractional spots of the same intensity are marked with red circles in the FFT image. The real space magnified STM image also has the same intensity for the adjacent Ru/Mn dark spots. Similar STM images at different bias voltages are shown in Figure 5.6b-d. Positive and negative bias voltages do not cause changes in the STM images in the constant current mode, indicating the C_{4v} symmetry of the x_c surface electronic structure, as expected from its lattice structure.

Figure 5.7 shows the STM images for x = 0.23 surface. One of the larger sized (20 nm × 12 nm) STM images includes dark areas of Mn dopant and defects of the cleaved sample surface at 77 K. The surface cells are marked with black squares, each Sr point is assigned a numerical number, and we first measure the intensities of four integer points (1, 2, 3, 4) on the corresponding black-and-white FFT images on the right side. After determining that their intensities are close (in order to exclude the tip effect), the intensities of four fractional points assigned (a, b, c and d) can be used to represent the electronic symmetry of the surface. As listed in Table 5.1, we note that

the difference between the intensity of the integer *tet*-(1×1) point and the four fractional spots is unsignificant (~3%). All sample surfaces in Figure 5.7b-d show a C_{4v} symmetry at different sample bias voltages. However, the freshly cleaved surface at $x = 1.0$ is insulated and the large area STM image (100 nm × 100 nm) is shown in Figure 5.8, indicating a charging effect on its surface.

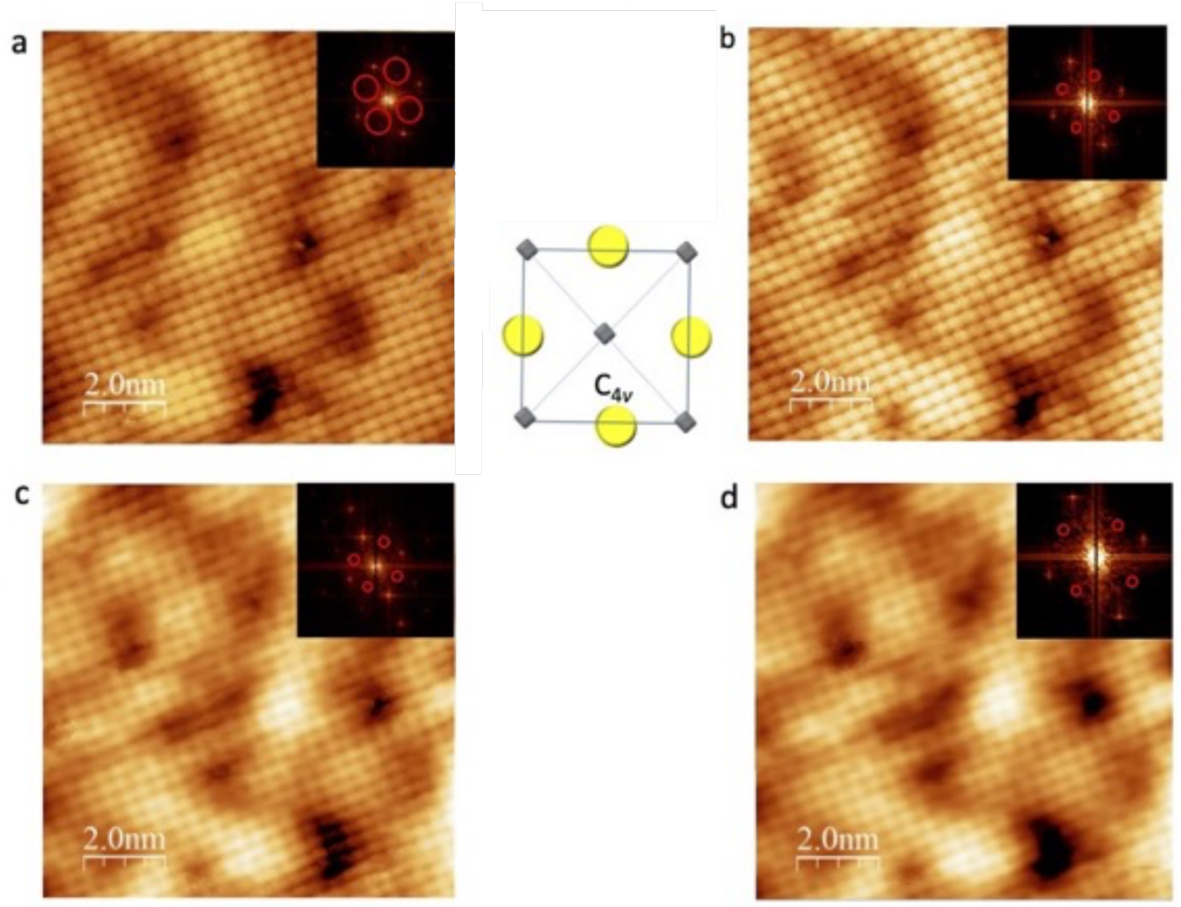

Figure 5.6. STM topography (10 nm × 10 nm) and the corresponding FFT images for x_c under different bias voltages at 77 K: (a) V_s = -10 mV, I_s = 80 pA, (b) V_s = 10 mV, I_s = 80 pA, (c) V_s = -100 mV, I_s = 80 pA, and (d) V_s = 100 mV, I_s = 80 pA. The fractional spots with the same intensities are marked with solid red squares. The STM image illustrates C_{4v} symmetry with the same Sr sites and the Ru/Mn sites.

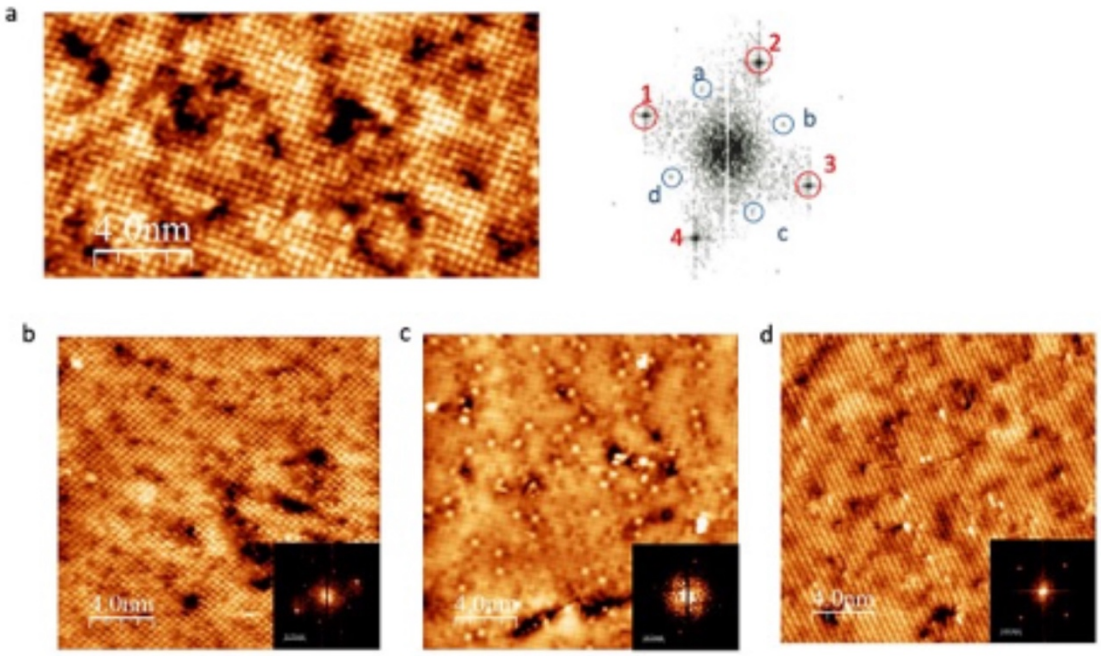

Figure 5.7. Constant-current STM topography at 77 K for x = 0.23: (a) STM image with bias voltage V_s = -0.5V and set current I_s = 90 pA. Shown on the right is the FFT image corresponding to the left STM image, where there are four fractional spots of close intensities, labeled as a, b, c, and d. (b-d) Sample bias voltage dependent STM images and corresponding FFTs (inset) for x = 0.23 with (b) V_s = -0.8V, (c) V_s = -1.0V, and (d) V_s = -0.9V with a tunneling current of I_s = 90 pA.

Table 5.1. Comparison of the integrated spots intensities measured from the Figure 5.7a.: four integer spots and four fractional spots intensities. The sites 1-4 and a-d all obtain close values in the intensity indicating a C_{4v} symmetry on the FFT image.

Integer spots #	Integrated Intensities	Fractional spot#	Integrated Intensities
1	979450	a	273023
2	966513	b	282056
3	964317	c	275006
4	976833	d	274804

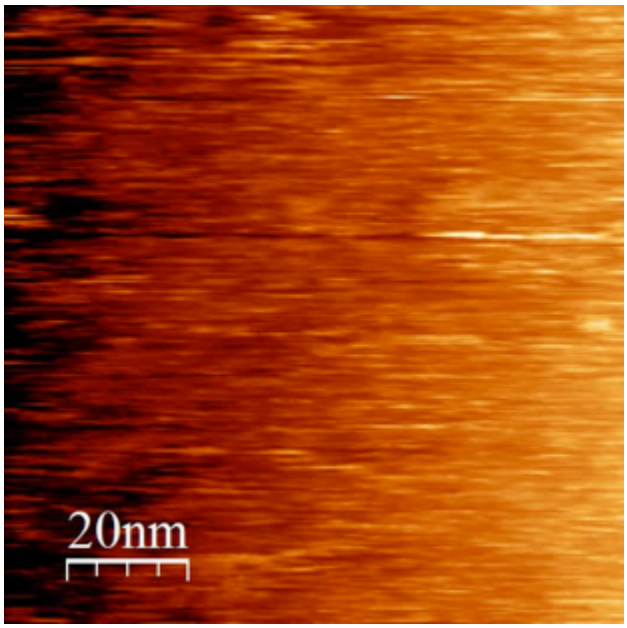

Figure 5.8. Large STM image (100 nm × 100 nm) of the fresh cleaved x =1.0 surface at 77 K (Vs = -0.7V, I_s = 10pA).

For $Sr_3(Ru_{1-x}Mn_x)_2O_7$, the responses of the surface electrons to the bulk insulating AFM phase can be identified from the changes in the STM images when cooled down to 5K. The STM images are shown in Figure 5.9. The STM measurements show that the ($\sqrt{2} \times \sqrt{2}$) R45°superstructure exists at high and low bias voltages and that there is no change when cooled though the bulk AFM ordering temperature (~ 80 K).The distribution Mn on the $Sr_3(Ru_{1-x}Mn_x)_2O_7$ surface also significantly affects its surface properties, and inhomogeneous surface impurities may cause an inhomogeneous electronic environment on the surface. Therefore, we performed a statistical analysis of the STM images as shown in Figure 5.10. The Mn is randomly distributed on the surface without any indication of short-range clustering. Mn sites are visible on the STM large image at 32 nm × 32 nm with bias voltage V_s = 50 mV. For the counting process at x_c surface, and Mn sites are marked with color dots inside the red squares on the magnified image. We can observe that the distribution of Mn on the surface is approximately uniform at the marked 16 nm × 16 nm area. The calculated radial

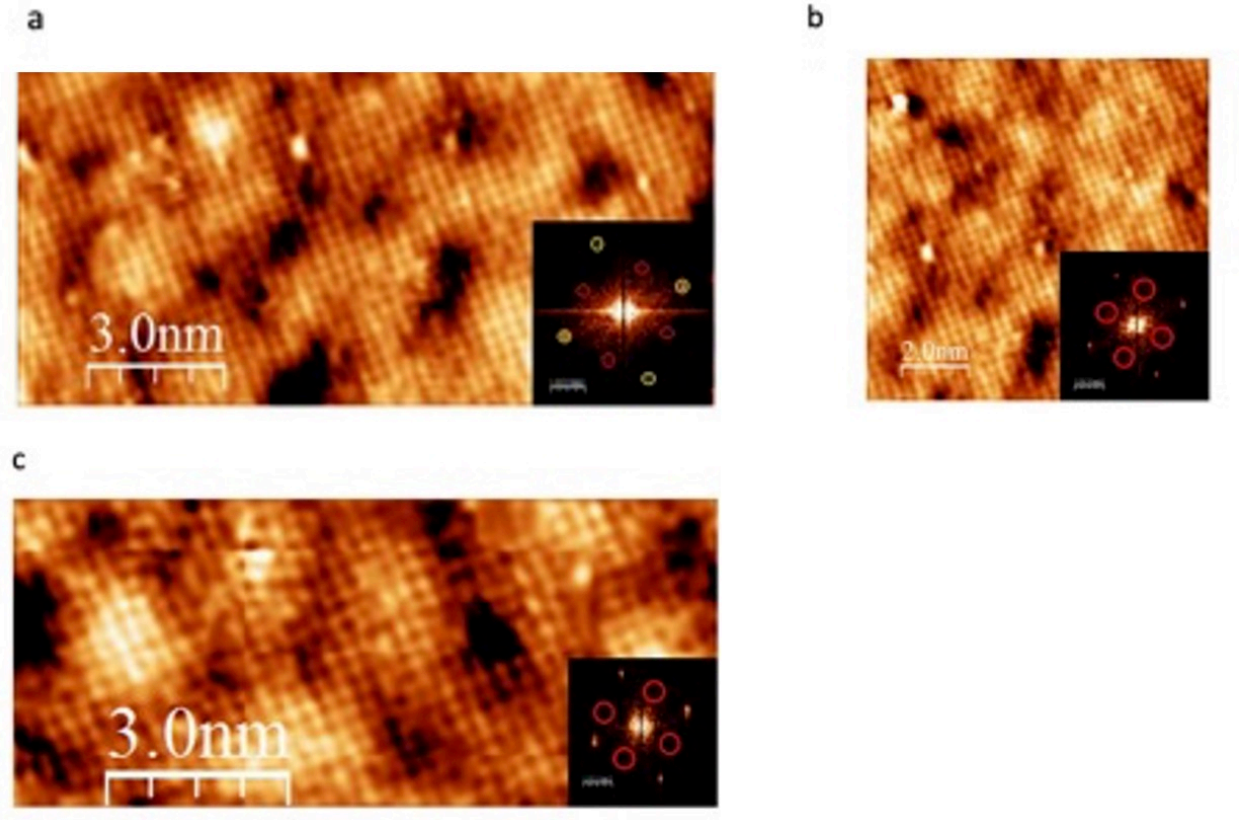

Figure 5.9. Constant-current STM results for $x = 0.16$ on the same cleaved sample surface at 5 K. (a) A large area (12 nm × 9 nm) STM image for a bias voltage V_s = - 0.5V, setpoint current I_s = 90 pA. The inset is the corresponding FFT image where the *tet*-(1 × 1) integer spots are marked in yellow, and the red circles mark the fractional spots with the relative intensities. (b) (8 nm × 8 nm) STM image for a bias voltage V_s = -0.1V. (c) (9 nm × 6 nm) STM image for a bias voltage V_s = -0.15V. The C_{4v} symmetry has been observed on all the surfaces with different sample bias voltages.

distribution ratio (RDR) curve shown in Figure 5.10c represents a function of the Mn-Mn distance within a unit 16 nm × 16 nm area, while the RDR value is the ratio of the observed histogram to the histogram of a random model with the same number of doping values [117]. For the x_c, the Mn-Mn pairs on the surface of counts plotted indicate that Mn is randomly distributed without any sign of short-range clustering. For RDR values close to 0, it indicates the short-range clustering model of Mn on the surface. Similar RDR values close to 1 were found by the statistical counts of the surface Mn dopants for all samples. From this, it can be said that no Mn was found on the surface of the samples without clustering.

The surface dopant distribution indicates that the electronic environment is homogeneous and is not influenced by other sites. The coefficients of the RDR model have a subtle relationship with the actual surface octahedron model, which is defined as:

$$\sum_{i=0}^{n} f\,(M^*, M) / \sum_{i=0}^{n} f(M', M) \quad (5.1),$$

where the direction of the surface octahedral rotation M is defined by a binary value 0 or 1 for counterclockwise or clockwise rotation directions, and the value of M^* is distinguished by the

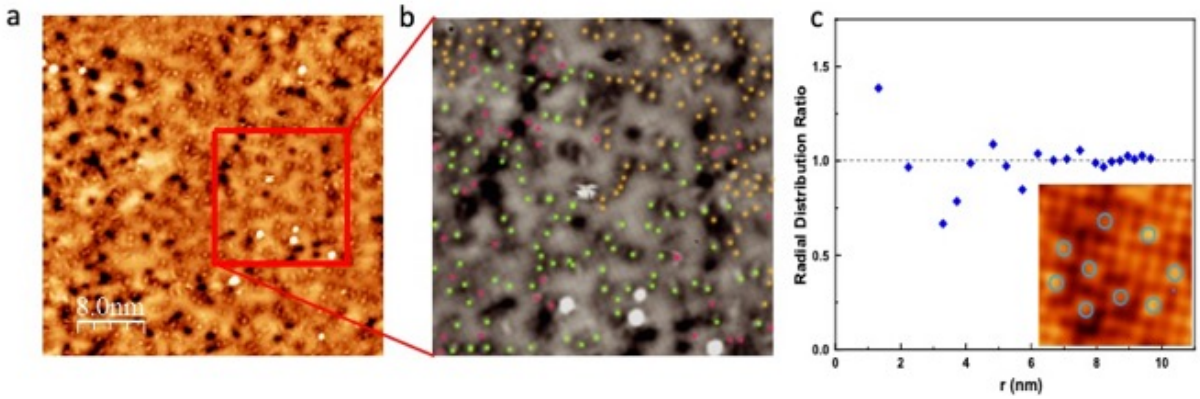

Figure 5.10. (a) STM topography (32 nm × 32 nm) for $Sr_3(Ru_{0.84}Mn_{0.16})_2O_7$ at 77 K with V_s = 50mV, I_s = 80 pA.(b) The Mn dopants inside the red 16nm ×16nm square are marked with different colors. (c)The radial distribution ratio of the Mn dopants is near 1, which indicates an even distribution.

rotation of the nearest neighbor to M varies between 0 and 1. Avalue below 1 indicates a lack of dependence of the rotation direction between the two nearest locations. Thus, we observed no dependence between *ccw* rotations and *cw* rotations of Mn sites on the surfaces of the different samples. Our experimental results effectively show that the cleaved (001) surface has the correct Sr-O termination on the topmost surface layer and no mixed phase.

5.2 STS Measurements on $Sr_3(Ru_{1-x}Mn_x)_2O_7$ (x = 0, 0.08, 0.16, and 0.23)

The main emphasis in this section is on STS measurements of $Sr_3(Ru_{1-x}Mn_x)_2O_7$ surfaces, exploring the evolution of the electronic properties with Mn doping. STS measurements of surface conductivity for x = 0, 0.08, 0.16, and 0.23 provide a good understanding of the surface

conductivity. The x_c sample surface at low temperatures and high magnetic fields (~9 T) in response to the bulk AFM phase was also carefully investigated. STS measurements on the $Sr_3Ru_2O_7$ crystal surface in the presence of an applied magnetic field parallel to the *c*-axis from B = 0 to 11 T [87]. Figure 5.11. shows the 'dip-in-dip' feature around the Fermi energy. The surface conductance dI/dV is presented in Figure 5.11a, with a transformation of the spectral weight of the two small peaks around -3 mV and +4 mV with the application of an external magnetic field up to 11 Tesla. The same dip characteristics around the Fermi energy can be seen for other ruthenate surfaces, such as Sr_2RuO_4 and $Sr_4Ru_3O_{10}$ [118]. The spectral width of these observed peaks becomes wider due to the full-width half-maximum (FWHM) resolution in the measurement and the choice of bias voltage.

5.2.1 Surface Conductance of $Sr_3(Ru_{1-x}Mn_x)_2O_7$ (x = 0, 0.08, and 0.23)

The collected dI/dV curve is proportional to the surface density of states. By assuming that the density of states at the tip is structureless, we use current imaging-tunneling spectroscopy (CITS) to collect a small area differential conductance curve. The obtained dI/dV curves are an average of more than 30 STS curves of the regions on and off the Mn site. The measurements were performed on samples that had been cleaved twice, and we measured the STS curves at different locations on the sample surface explicitly with different tunneling around the Fermi energy, as shown in Figure 5.12. We found that the dI/dV signal at the Fermi energy in the curves recorded on and off Mn sites at I_s =100 pA did not change, and the Mn site has a higher DOS at +0.8V which is the suitable bias voltage to clearly map surface Mn dopant. In contrast, in Figure 5.12b, the dI/dV or density of states at the Mn-doped sites is above the average value and is a flat region at

about 0.8 V, which explains in the STM topography, the Mn sites are not mapped until a higher bias voltage V_s = 0.85 V. The magnified image is shown in Figure. 5.12c, where zero-bias anomaly (ZBA) is seen in all spectra on the surface of the different ruthenates.

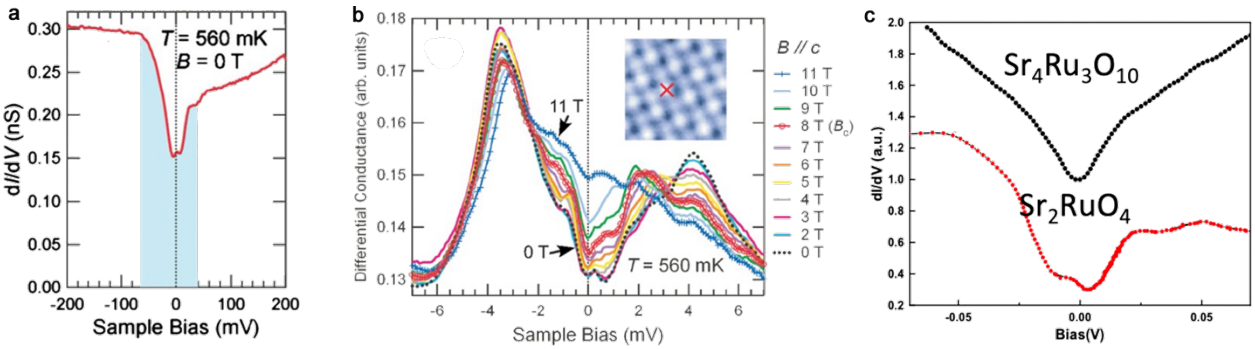

Figure 5.11. STS measurement on $Sr_3Ru_2O_7$ surface at 560 mK (a) at T = 560 mK, B = 0 T with the bias modulation V_{mod} = 500 uV_{rms}, f_{mod} = 717 Hz. (b) Magnetic field dependence of the STS curve on $Sr_3Ru_2O_7$ with V_{mod} = 500 uV_{rms}, f_{mod} = 717 Hz with the tip sitting on the Sr site marked with a red cross in the inset (Figure adapted from Ref. [87]). (c) Similar suppression of the surface conductance around the Fermi level or the ' dip in dip' features in Sr_2RuO_4 and $Sr_4Ru_3O_{10}$ from Ref. [119].

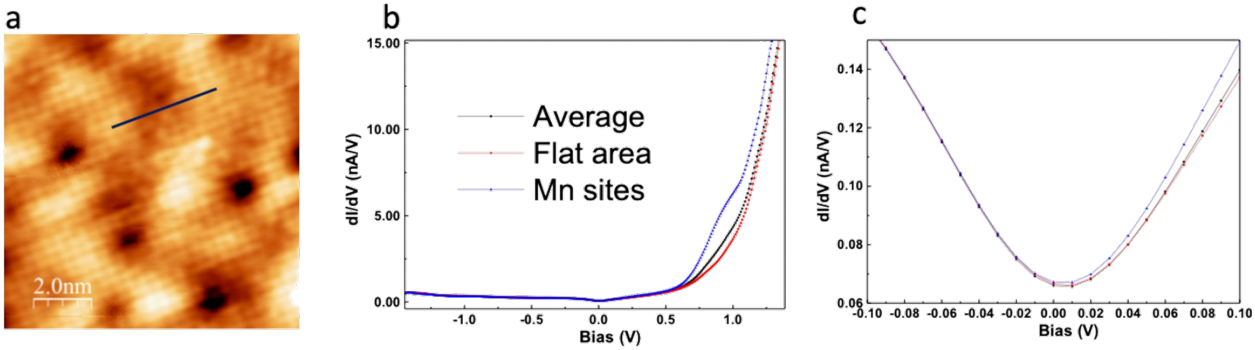

Figure 5.12. STM topography and spatially resolved-STS studies on/off the Mn sites (a) STM image for x = 0.08 with V_s = 0.85 V, I_s = 100 pA at 77 K. (b) Three dI/dV maps in the different surface areas: on/ off the Mn sites or the averaged curve from CITS. (c) Zoomed-in dI/dV spectroscopy around the Fermi energy V_{mod} = 500 uV_{rms}, f_{mod} = 300 Hz.

In Figure 5.13, the electronic properties of the surface vary considerably from compound to compound. It is clear that both x = 0 and x = 0.16 sample surfaces are metallic at a bias voltage

of V_s = 0.50 V at 77K. Along the dotted line of the Fermi energy, we find that the surface of the x_c sample has the best conduction. It is worth noting here that there are pseudo-gaps on the surfaces of all samples and that the density of electronic states at the Fermi energy is finite. Also, surface Mn dopant can lubricate the surface DOS and contribute to the observed intrinsic broadening of the zero-bias anomaly (ZBA), leading to the observation of the pseudo-gaps [120]. The reproducibility of the measurements at different locations on the sample surface is achieved and not dependent on different locations on the sample surface. Therefore, for such temperature dependent experiments, the tip has to be moved slightly out

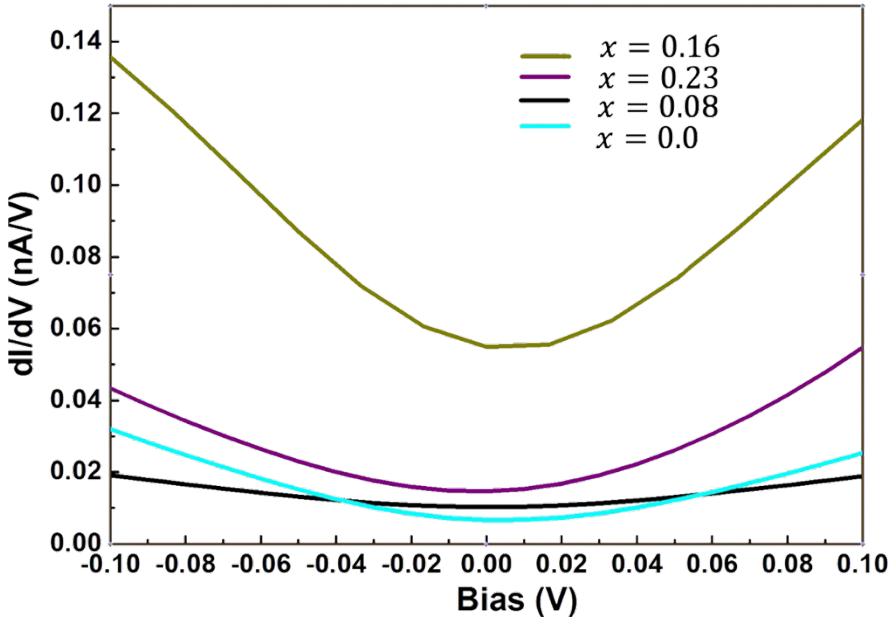

Figure 5.13. STS curves for x = 0.08, 0.16 and 0.23 at 77 K (V_s = - 0.8 V I_s = 100 pA). x_c has the highest DOS at the Fermi energy.

of the way due to thermal drift, resulting in a slight change in location that does not affect the final data collected. Figure 5.14 shows an image of the STM on the sample surface and a comparison plot of the density of states for x = 0 and 0.16. As shown in Figure 5.14b, the surface STM curve shows an increase in the density of states at the Fermi energy for x = 0.16 compared to x = 0.

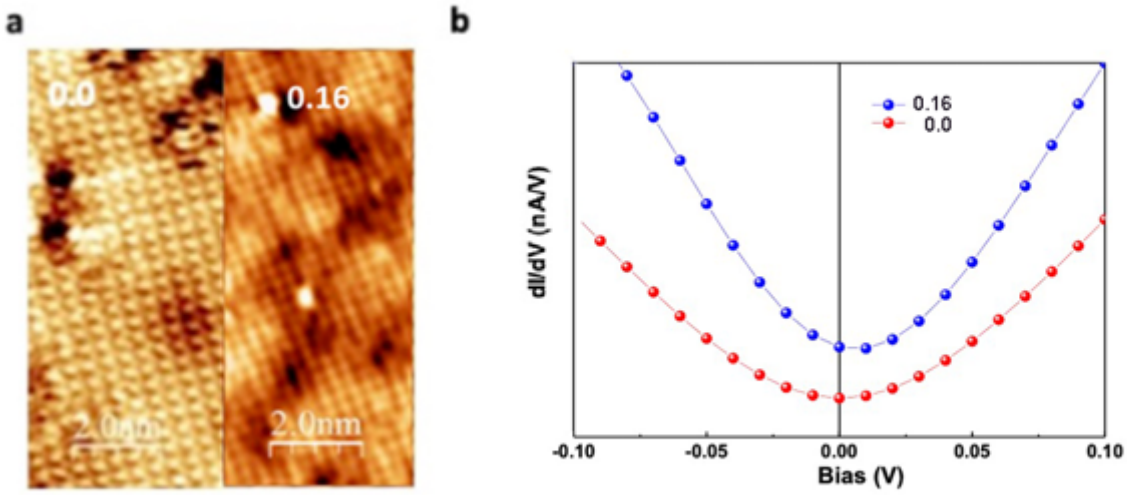

Figure 5.14. STM topography and STS of $x = 0.0$ and $x = 0.16$ surface at 5 K. (a) A 4 nm× 10 nm STM topography of $x = 0$ and $x = 0.16$ surface obtained with $V_s = 0.5$ V and $I_s = 90$ pA. (b) Averaged dI/dV curves with the line marked the Fermi level.

5.2.2 Field/Temperature-Dependent Measurements on $Sr_3(Ru_{0.84}Mn_{0.16})_2O_7$

We previously found that $Sr_3(Ru_{0.84}Mn_{0.16})_2O_7$ surface octahedral structure merely changed with surface atomic rearrangement in the bulk AFM phase. If the surface is the same as the bulk, the surface electronic properties might be affected as a function of temperature and applied magnetic field. Figure 5.15 shows the STM images and the averaged STS curves of $Sr_3(Ru_{0.84}Mn_{0.16})_2O_7$ measured at 5 K and 77 K with a bias voltage $V_s = 0.5$. Figure 5.15a shows the surface morphology of the x_c surface at different temperatures. The conventional thermal broadening can explain the corresponding dI/dV curves in Figure 5.15b due to the thermal effect of the tip and the surface. Comparing the values of differential conductance at the Fermi level, the x_c possesses finite DOS, so at low temperatures, its surface is also metallic, unlike the bulk insulating phase.

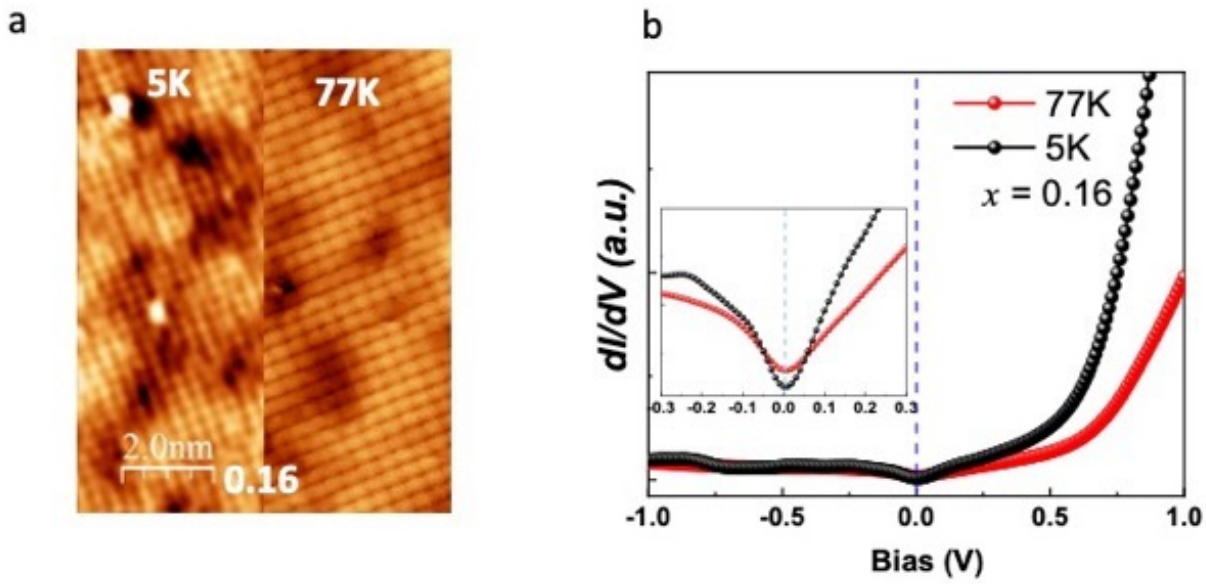

Figure 5.15. Temperature-dependent (a) STM topography and (b) STS curves for $Sr_3(Ru_{0.84}Mn_{0.16})_2O_7$ surface at 77K and 5K (V_s = 0.5 V). The inset represents the dI/dV curve ranging from -0.3V to 0.3V.

To exclude the response of surface magnetism to long-range bulk antiferromagnetic ordering, we applied an external magnetic field of 9T at 5K, as shown in Figure 5.16, we found no evidence of mixing of ordered and disordered surface regions, and the image resolution was nearly identical in the presence and absence of the magnetic field. No significant change in the conductivity spectrum is seen in Figure. 5.16b, which indicates that the surface is nonmagnetic.

In summary, we investigated the bias dependence of STM images and FFT symmetries, and the surface electronic properties of $Sr_3(Ru_{1-x}Mn_x)_2O_7$ vary with the surface structure coupled to the tilt and rotation of the surface octahedra. By measuring different intensities of the fractional points in the corresponding FFT images of each sample, we also qualitatively analyzed the tilt angle gradually decrease from $x = 0$ to $x = 0.08$, which is consistent with the results from our LEED measurements. Our statistical analysis also showed that the Mn on the surface of all samples is randomly distributed and is a homogeneous system at the microscopic level but may be inhomogeneous at the macroscopic level. We performed different tests at various locations and

different cleaved surfaces for the same samples. Through measured dI/dV curves, we found that the doping of Mn on the surface results in better conduction at Fermi energy, with the surface of x_c having the best conductivity (maximum DOS). The conductivity of the surface is coupled to the surface structure, where x_c surface has the largest octahedral rotation angle and no octahedral tilt. Unlike the bulk AFM insulating phase, studies under low temperature and high magnetic field revealed a metallic and nonmagnetic x_c surface. While these findings complemented prior results on the $Sr_3(Ru_{1-x}Mn_x)_2O_7$ surface electronic properties, further theoretical exploration is needed to understand surface magnetism fully.

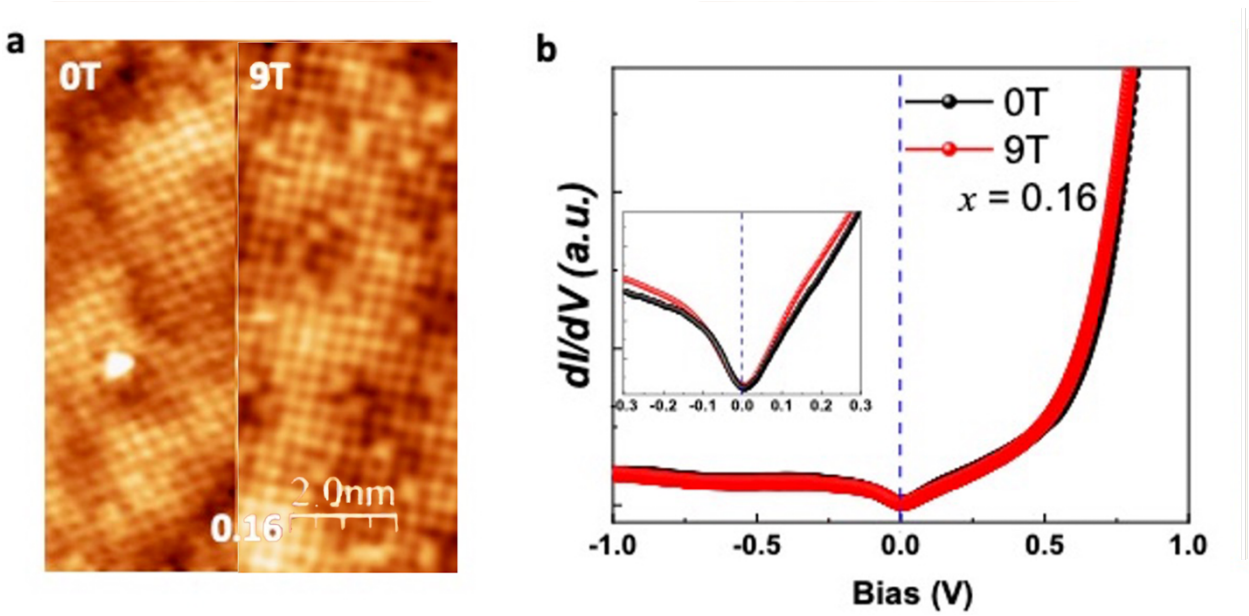

Figure 5.16. (a) STM topography and (b) STS curves for x_c surface with B = 0T and 9T (V_s = 0.5V and I_s = 100pA) at 5 K. The inset represents the dI/dV curves ranging from -0.3V to 0.3V.

Chapter 6. Discussion and Summary

The work in this dissertation deepens the understanding of the complexity of Mn-doped $Sr_3Ru_2O_7$ through the investigation of surface and bulk structure-property relationships of $Sr_3(Ru_{1-x}Mn_x)_2O_7$ (x = 0.0, 0.08, 0.16, 0.23, and 1) from the perspective of the crystal structure. The surface phase diagrams of the surface of $Sr_3(Ru_{1-x}Mn_x)_2O_7$ were constructed, revealing the enrichment phenomena in different regions as shown in Figure 6.1.

From the low-temperature XRD refinement of the $Sr_3(Ru_{1-x}Mn_x)_2O_7$ bulk structure, and we found that $Sr_3(Ru_{1-x}Mn_x)_2O_7$ underwent a series of structural changes, including the Jahn-Teller distortion in the *ab*-plane and the rotation of the RuO_6 octahedron along the *c* axis. These structural changes affect the occupancy of the orbital energy levels [121-123]. The out-of-plane lattice parameter *c* and the octahedral volume decrease monotonically with Mn substitution, and the in-plane lattice parameter *a* increases and then decreases from x = 0 to x = 0.16. The Rietveld refinement shows the variation of bond lengths and bond angles, and we find that the Jahn-Teller distortion of octahedra decreases almost linearly with *x*. Because of the tetragonal symmetry of *I*4/*mmm*, the bond length of Ru/Mn-O3 remains almost constant. It should be noted that the lattice parameters obtained from the neutron scattering experiments differ from the X-ray diffraction measurements. Due to the low penetration of X-ray diffraction, weak peaks are missing in the peak pattern, and the application of lower symmetry in the refinement often causes differences in the structural characterization.

Creating a surface breaks the bulk symmetry and the rotation of the octahedron does not fully relieve the strain, thus the surface octahedron has an additional tilt, which in turn leads to the observation of different physical properties. The surface phase diagram of $Sr_3(Ru_{1-x}Mn_x)_2O_7$ at 77K is shown in Figure 6.1. where we obtained the rotation and tilt angles of the surface octahedra by

using LEED I-V analysis. The double-layered octahedra allow for complex relationships. Therefore, different surface structure models are tested, from which we obtained the optimal solution when the bilayered octahedra rotated in different directions. The rotation of the surface octahedron (purple squares) decreases as x increases, and the tilt of the octahedron (yellow squares) also decreases and vanishes at x_c for $x < x_c$. As the surface RuO_6 octahedral rotation decreases with Mn doping, the suppressed rotational distortion reduces the coupling between orbitals [124,125]. The refined in-plane Ru/Mn-O3 bond length also reaches a maximum at x_c. The surface Fermi energy LDOS of $Sr_3(Ru_{1-x}Mn_x)_2O_7$ (x = 0, 0.08, 0.16, 0.23) (circle) matches the inverse Fano q-parameter curve (triangle) obtained by fitting the $A_{1g}(2)$ phonon. A surface metal-insulator phase transition occurs at the surface in the high doping region between x_c and x = 1.

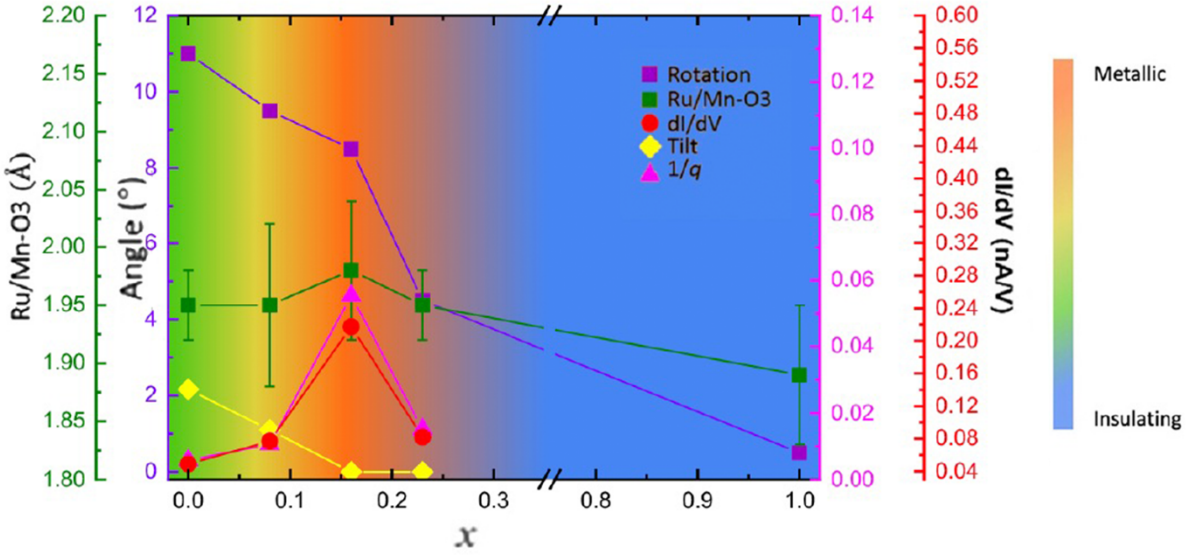

Figure 6.1. :The surface phase diagram of $Sr_3(Ru_{1-x}Mn_x)_2O_7$ at 77K contains the magnitude of the Fano parameter q, the tilt and rotation angle, the in-plane Ru/Mn-O3 bond length and the value of the surface dI/dV at Fermi energy versus x. The color bars on the right side indicate the different degrees of metallicity.

Additional important findings, including STM/STS studies described in Chapter 5 illustrate the consistency of the surface electronic and lattice structures, with no spatial reconstruction of the

local electronic states found at different bias voltages. The amount of Mn dopants on the surface is less compared to the bulk value and the Mn dopants do not change the LDOS of the surface. Across a wide range of Ru substitutions, the STS spectra of $Sr_3(Ru_{1-x}Mn_x)_2O_7$ are characterized by zero-bias anomalies (ZBA), i.e., a V-shaped gap near the Fermi energy [126]. A similar situation occurs on the surfaces of Sr_2RuO_4, $Sr_3Ru_2O_7$, and $Sr_4Ru_3O_{10}$ [87,118,119]. Unlike the electron inhomogeneity induced by doping observed in the Mott system [127,128], it is unlikely that this situation explains the ZBA seen in our data since no induced charge ordering is observed, and STS remains unchanged upon applying an external magnetic field for x_c at 5.2 K. The x_c surface is nonmagnetic and ruled out the possibility of ZBA is due to AFM fluctuations [128]. Probing the surface properties of Mn dopants tailored to $Sr_3(Ru_{1-x}Mn_x)_2O_7$ provides insights into the physics of the bulk-surface relationships in general.

References

[1] Y. Murakami, P. Werner, N. Tsuji, and H. Aoki, Physical Review B **88**, 125126 (2013).

[2] O. Gunnarsson and O. Rösch, Journal of Physics: Condensed Matter **20**, 043201 (2008).

[3] J. Cao, L. Vergara, J. Musfeldt, A. Litvinchuk, Y. Wang, S. Park, and S.-W. Cheong, Physical review letters **100**, 177205 (2008).

[4] S. A. Grigera *et al.*, Science **294**, 329 (2001).

[5] M. Suda, Y. Kawasugi, T. Minari, K. Tsukagoshi, R. Kato, and H. M. Yamamoto, Advanced Materials **26**, 3490 (2014).

[6] S. Maekawa, T. Tohyama, S. E. Barnes, S. Ishihara, W. Koshibae, and G. Khaliullin, *Physics of transition metal oxides* (Springer Science & Business Media, 2013), Vol. 144.

[7] A. Smith and A. Welch, Acta Crystallographica **13**, 653 (1960).

[8] A. Liebsch and H. Ishida, Physical review letters **98**, 216403 (2007).

[9] M. Paraskevopoulos, F. Mayr, J. Hemberger, A. Loidl, R. Heichele, D. Maurer, V. Müller, A. Mukhin, and A. Balbashov, Journal of Physics: Condensed Matter **12**, 3993 (2000).

[10] T. M. Squires and M. Z. Bazant, Journal of Fluid Mechanics **560**, 65 (2006).

[11] C. Chen *et al.*, Physical Review B **94**, 085420 (2016).

[12] B. Stöger *et al.*, Physical Review B **90**, 165438 (2014).

[13] R. G. Moore, J. Zhang, S. Kalinin, A. Baddorf, R. Jin, D. Mandrus, and E. Plummer, physica status solidi (b) **241**, 2363 (2004).

[14] I. Bhushan Sharma and D. Singh, *Solid state chemistry of Ruddlesden-Popper type complex oxides* 1998), Vol. 21.

[15] R. H. Mitchell, *Perovskites: modern and ancient* (Almaz Press Thunder Bay, 2002), Vol. 7.

[16] R. Matzdorf, Z. Fang, J. Zhang, T. Kimura, Y. Tokura, K. Terakura, and E. Plummer, Science **289**, 746 (2000).

[17] D. Kim, B. Zink, F. Hellman, S. McCall, G. Cao, and J. Crow, Physical Review B **67**, 100406 (2003).

[18] M. Covington, M. Aprili, E. Paraoanu, L. Greene, F. Xu, J. Zhu, and C. A. Mirkin, Physical review letters **79**, 277 (1997).

[19] G. Cao, C. S. Alexander, S. McCall, J. E. Crow, and R. P. Guertin, Materials Science and Engineering: B **63**, 76 (1999).

[20] R. G. Moore, V. B. Nascimento, J. Zhang, J. Rundgren, R. Jin, D. Mandrus, and E. W. Plummer, Physical Review Letters **100**, 066102 (2008).

[21] M. Braden, W. Reichardt, S. Nishizaki, Y. Mori, and Y. Maeno, Physical Review B **57**, 1236 (1998).

[22] R. Moore, M. D. Lumsden, M. B. Stone, J. Zhang, Y. Chen, J. Lynn, R. Jin, D. Mandrus, and E. Plummer, Physical Review B **79**, 172301 (2009).

[23] S. Nakatsuji and Y. Maeno, Physical Review Letters **84**, 2666 (2000).

[24] S. Nakatsuji, D. Hall, L. Balicas, Z. Fisk, K. Sugahara, M. Yoshioka, and Y. Maeno, Physical Review Letters **90**, 137202 (2003).

[25] H. Liu, H. Liu, S. H. Lapidus, Y. S. Meng, P. J. Chupas, and K. W. Chapman, Journal of The Electrochemical Society **164**, A1802 (2017).

[26] I. I. Mazin and D. J. Singh, Physical Review Letters **82**, 4324 (1999).

[27] R. G. Pearson, Proceedings of the National Academy of Sciences **72**, 2104 (1975).

[28] R. Englman and R. Englman, *The Jahn-Teller effect in molecules and crystals* (Wiley-Interscience New York, 1972).

[29] O. Friedt, M. Braden, G. André, P. Adelmann, S. Nakatsuji, and Y. Maeno, Physical Review B **63**, 174432 (2001).

[30] D. Mesa, Doctoral thesis, Louisiana State University, 2014.

[31] H. Shaked, J. D. Jorgensen, O. Chmaissem, S. Ikeda, and Y. Maeno, Journal of Solid State Chemistry **154**, 361 (2000).

[32] R. Kiyanagi, K. Tsuda, N. Aso, H. Kimura, Y. Noda, Y. Yoshida, S.-I. Ikeda, and Y. Uwatoko, Journal of the Physical Society of Japan **73**, 639 (2004).

[33] Q. Huang, J. W. Lynn, R. W. Erwin, J. Jarupatrakorn, and R. J. Cava, Physical Review B **58**, 8515 (1998).

[34] S. A. Grigera *et al.*, Science **306**, 1154 (2004).

[35] A. W. Rost, R. S. Perry, J. F. Mercure, A. P. Mackenzie, and S. A. Grigera, Science **325**, 1360 (2009).

[36] A. Tamai *et al.*, Physical Review Letters **101**, 026407 (2008).

[37] S.-I. Ikeda, Y. Maeno, S. Nakatsuji, M. Kosaka, and Y. Uwatoko, Physical Review B **62**, R6089 (2000).

[38] J. Ding *et al.*, Physical Review B **87**, 054428 (2013).

[39] R. S. Perry *et al.*, Physical Review Letters **86**, 2661 (2001).

[40] E. Ohmichi, Y. Yoshida, S. I. Ikeda, N. V. Mushnikov, T. Goto, and T. Osada, Journal of Magnetism and Magnetic Materials **272-276**, 976 (2004).

[41] S. Grigera *et al.*, Science **294**, 329 (2001).

[42] R. Mathieu *et al.*, Physical Review B **72**, 092404 (2005).

[43] P. Rivero, R. Jin, C. Chen, V. Meunier, E. W. Plummer, and W. Shelton, Scientific Reports **7**, 10265 (2017).

[44] Q. Zhang *et al.*, Physical Review B **95**, 220403 (2017).

[45] M. A. Hossain *et al.*, Physical Review B **86**, 041102 (2012).

[46] D. Mesa, F. Ye, S. Chi, J. A. Fernandez-Baca, W. Tian, B. Hu, R. Jin, E. W. Plummer, and J. Zhang, Physical Review B **85**, 180410 (2012).

[47] B. Hu, Louisiana State University and Agricultural and Mechanical College, 2011.

[48] H. Valencia, A. Gil, and G. Frapper, The Journal of Physical Chemistry C **114**, 14141 (2010).

[49] M. P. Allan *et al.*, New Journal of Physics **15**, 063029 (2013).

[50] R. Haydock and M. Kelly, Surface Science **38**, 139 (1973).

[51] I. Batra and S. Ciraci, Physical Review Letters **34**, 1337 (1975).

[52] P. Kelires and J. Tersoff, Physical review letters **63**, 1164 (1989).

[53] P. Carnevali, F. Ercolessi, and E. Tosatti, Physical Review B **36**, 6701 (1987).

[54] K. Christmann, F. Chehab, V. Penka, and G. Ertl, Surface Science **152**, 356 (1985).

[55] K. Horn and M. Scheffler, *Electronic structure* (Elsevier, 2000).

[56] R. G. Moore, J. Zhang, V. B. Nascimento, R. Jin, J. Guo, G. T. Wang, Z. Fang, D. Mandrus, and E. W. Plummer, Science **318**, 615 (2007).

[57] G. Li *et al.*, Scientific Reports **3**, 2882 (2013).

[58] C. Chen, Doctoral thesis, Louisiana State University, 2016.

[59] G. Rosenbaum, K. C. Holmes, and J. Witz, Nature **230**, 434 (1971).

[60] L. J. Farrugia, J. Appl. Crystallography **32**, 837 (1999).

[61] G. Sheldrick, Acta Crystallographica Section C **71**, 3 (2015).

[62] J. Buschmann, E. Müller, and P. Luger, Acta Crystallographica Section C: Crystal Structure Communications **42**, 873 (1986).

[63] H. M. Rietveld, Journal of applied Crystallography **2**, 65 (1969).

[64] T. Milenković and N. Pržulj, Cancer informatics **6**, CIN. S680 (2008).

[65] G. Taylor, Acta Crystallographica Section D **59**, 1881 (2003).

[66] A. L. Spek, Acta Crystallographica Section C: Structural Chemistry **71**, 9 (2015).

[67] L. N. Rozanov, (IOP Publishing, 2002).

[68] C. Davisson and L. H. Germer, Physical review **30**, 705 (1927).

[69] M. Seah, Surface and interface analysis **44**, 1353 (2012).

[70] R. L. Park and J. Houston, Surface Science **18**, 213 (1969).

[71] V. Nascimento, R. G. Moore, J. Rundgren, J. Zhang, L. Cai, R. Jin, D. G. Mandrus, and E. Plummer, *Procedure for LEED I-V structural analysis of metal oxide surfaces: Ca1.5Sr0.5RuO4(001)* 2007).

[72] C. Chen, J. Kim, Y. Yang, G. Cao, R. Jin, and E. W. Plummer, Physical Review B **95**, 094118 (2017).

[73] M. A. VanHove, W. H. Weinberg, and C.-M. Chan, *Low-energy electron diffraction: experiment, theory and surface structure determination* (Springer Science & Business Media, 2012), Vol. 6.

[74] G. Li, Doctoral thesis, Louisiana State University, 2013.

[75] M. A. Van Hove, W. H. Weinberg, and C. M. Chan, *Low-energy electron diffraction : experiment, theory, and surface structure determination* (Berlin ; New York : Springer-Verlag, c1986., 1986), Springer series in surface sciences: 6.

[76] J. Pendry, Journal of Physics C: Solid State Physics **13**, 937 (1980).

[77] J. Rundgren, Physical Review B **68**, 125405 (2003).

[78] M. A. Van Hove and S. Y. Tong, in *Surface Crystallography by LEED* (Springer, 1979), pp. 71.

[79] J. Pendry, Journal of Physics C: Solid State Physics **4**, 3095 (1971).

[80] Y. Gauthier, Y. Joly, R. Baudoing, and J. Rundgren, Physical Review B **31**, 6216 (1985).

[81] K. D. Tsuei, E. W. Plummer, and P. J. Feibelman, Physical Review Letters **63**, 2256 (1989).

[82] Ismail, Physical Review B **67** (2003).

[83] H. Ibach, *Electron energy loss spectrometers : the technology of high performance* (Berlin ; New York : Springer-Verlag, c1991., 1991), Springer series in optical sciences: v. 63.

[84] S. Grafstrom, J. Kowalski, and R. Neumann, Measurement Science and Technology **1**, 139 (1990).

[85] G. Binnig, H. Rohrer, C. Gerber, and E. Weibel, Physical Review Letters **49**, 57 (1982).

[86] Ø. Fischer, M. Kugler, I. Maggio-Aprile, C. Berthod, and C. Renner, Reviews of Modern Physics **79**, 353 (2007).

[87] K. Iwaya *et al.*, Physical Review Letters **99**, 057208 (2007).

[88] J. Leshen, M. Kavai, I. Giannakis, Y. Kaneko, Y. Tokura, S. Mukherjee, W.-C. Lee, and P. Aynajian, Communications Physics **2**, 1 (2019).

[89] B. Hu, G. T. McCandless, M. Menard, V. B. Nascimento, J. Y. Chan, E. W. Plummer, and R. Jin, Physical Review B **81**, 184104 (2010).

[90] B. Hu, G. T. McCandless, V. O. Garlea, S. Stadler, Y. Xiong, J. Y. Chan, E. W. Plummer, and R. Jin, Physical Review B **84**, 174411 (2011).

[91] B. Hu, Louisiana State University.

[92] Z. Zhu *et al.*, Physical review letters **122**, 017202 (2019).

[93] L. Xing, X. Gui, W. Xie, H. Cao, J. Yan, B. C. Sales, and R. Jin, Scientific reports **8**, 1 (2018).

[94] Q. Xu, H. Liu, L. Zhang, J. Xie, H. Hao, M. Cao, Z. Yao, and M. T. Lanagan, Rsc Advances **6**, 59280 (2016).

[95] F. S. Varley, Neutron news **3**, 29 (1992).

[96] C. Suryanarayana and M. G. Norton, in *X-Ray Diffraction* (Springer, 1998), pp. 3.

[97] E. O. Wollan and C. Shull, Physical Review **73**, 830 (1948).

[98] R. Jin, H. Sha, P. Khalifah, R. E. Sykora, B. C. Sales, D. Mandrus, and J. Zhang, Physical Review B **73**, 174404 (2006).

[99] Q. Zhang *et al.*, Physical Review B **99**, 094416 (2019).

[100] M. Woińska, S. Grabowsky, P. M. Dominiak, K. Woźniak, and D. Jayatilaka, Science advances **2**, e1600192 (2016).

[101] W. F. Sanjuan-Szklarz, M. Woińska, S. Domagała, P. M. Dominiak, S. Grabowsky, D. Jayatilaka, M. Gutmann, and K. Woźniak, IUCrJ **7** (2020).

[102] V. B. Nascimento, R. Moore, J. Rundgren, J. Zhang, L. Cai, R. Jin, D. Mandrus, and E. W. Plummer, Physical Review B **75**, 035408 (2007).

[103] R. Döll and M. Van Hove, Surface Science **355**, L393 (1996).

[104] R. Matzdorf, Z. Fang, Ismail, J. Zhang, T. Kimura, Y. Tokura, K. Terakura, and E. W. Plummer, Science **289**, 746 (2000).

[105] H. H. Kung, *Transition metal oxides: surface chemistry and catalysis* (Elsevier, 1989).

[106] Ismail, J. Zhang, R. Matzdorf, T. Kimura, Y. Tokura, and E. W. Plummer, Physical Review B **67**, 035407 (2003).

[107] S. Dey, M. Banik, E. Hulkko, K. Rodriguez, V. Apkarian, M. Galperin, and A. Nitzan, Physical Review B **93**, 035411 (2016).

[108] P. Wölfle, Y. Dubi, and A. Balatsky, Physical review letters **105**, 246401 (2010).

[109] C. Ott, A. Kaldun, P. Raith, K. Meyer, M. Laux, J. Evers, C. H. Keitel, C. H. Greene, and T. Pfeifer, Science **340**, 716 (2013).

[110] S. Weimann, Y. Xu, R. Keil, A. E. Miroshnichenko, A. Tünnermann, S. Nolte, A. A. Sukhorukov, A. Szameit, and Y. S. Kivshar, Physical review letters **111**, 240403 (2013).

[111] T. Oguchi, Physical Review B **51**, 1385 (1995).

[112] R. Moore, V. Nascimento, J. Zhang, J. Rundgren, R. Jin, D. Mandrus, and E. Plummer, Physical review letters **100**, 066102 (2008).

[113] J. Lee, M. Allan, M. Wang, J. Farrell, S. Grigera, F. Baumberger, J. Davis, and A. Mackenzie, Nature Physics **5**, 800 (2009).

[114] Z. Fang and K. Terakura, Physical Review B **64**, 020509 (2001).

[115] S. N. Ruddlesden and P. Popper, Acta Crystallographica **11**, 54 (1958).

[116] P. Xu, S. D. Barber, M. L. Ackerman, J. Kevin Schoelz, and P. M. Thibado, Journal of Vacuum Science & Technology B, Nanotechnology and Microelectronics: Materials, Processing, Measurement, and Phenomena **31**, 04D103 (2013).

[117] I. Zeljkovic, D. Huang, C.-L. Song, B. Lv, C.-W. Chu, and J. E. Hoffman, Physical Review B **87**, 201108 (2013).

[118] T. Novgorodov, Doctoral thesis, Universität Kassel, 2007.

[119] M. Klinke, Doctoral thesis, kassel university 2013.

[120] H. Ibach and J. Rajeswari, Journal of Electron Spectroscopy and Related Phenomena **185**, 61 (2012).

[121] H.-T. Jeng, S.-H. Lin, and C.-S. Hsue, Physical Review Letters **97**, 067002 (2006).

[122] H. Shaked, J. D. Jorgensen, S. Short, O. Chmaissem, S. I. Ikeda, and Y. Maeno, Physical Review B **62**, 8725 (2000).

[123] M. Kubota, H. Fujioka, K. Hirota, K. Ohoyama, Y. Moritomo, H. Yoshizawa, and Y. Endoh, journal of the physical society of japan **69**, 1606 (2000).

[124] S. Mukherjee and W.-C. Lee, Physical Review B **94**, 064407 (2016).

[125] Y. Heo, D. Kan, M. Anada, Y. Wakabayashi, H. Tajiri, and Y. Shimakawa, Physical Review B **99**, 174420 (2019).

[126] H. Zeller and I. Giaever, Physical Review **181**, 789 (1969).

[127] A. Richardella, P. Roushan, S. Mack, B. Zhou, D. A. Huse, D. D. Awschalom, and A. Yazdani, science **327**, 665 (2010).

[128] Z. Wang *et al.*, Proceedings of the National Academy of Sciences **115**, 11198 (2018).

Vita

Yifan Yang was born on Jun 29, 1990, in Zhoukou, Henan Province, China. He graduated from Mississippi College, Clinton, Mississippi, with a Bachelor of Science degree in Engineering physics in December 2012 and started his graduate study in The Department of Experimental Statistics in Louisiana State University, Baton Rouge, Louisiana, in January 2013. In September 2013, he transferred to The Department of Physics & Astronomy at Louisiana State University, Baton Rouge, Louisiana, to start the doctoral program. He expects to receive his Doctor of Philosophy degree in physics in August 2021.